Reduced beam-squint series fed horn array manufactured using using additive manufacturing

by

Alexander Simonovic

Submitted in partial fulfillment of the requirements for the degree
Master of Engineering (Electronic Engineering)

in the

Department of Electrical, Electronic and Computer Engineering
Faculty of Engineering, Built Environment and Information Technology

UNIVERSITY OF PRETORIA

March 2023

SUMMARY

REDUCED BEAM-SQUINT SERIES FED HORN ARRAY MANUFACTURED USING ADDITIVE MANUFACTURING

by

Alexander Simonovic

Supervisor:	Prof T. Stander
Department:	Electrical, Electronic and Computer Engineering
University:	University of Pretoria
Degree:	Master of Engineering (Electronic Engineering)
Keywords:	array, beam-squint, slow wave, true time delay, phase shift, additive manufacturing, plating

In this work, a series-fed antenna is designed with beam-squint compensation. The horn array operates between 21.5 GHz and 23.5 GHz. Beam-squint compensation is designed into the array using time delay equalisation, thus keeping the phase of the signal arriving at the radiating horns equal. This is achieved by using power dividers and sinusoidal time delays. The waveguide form factor was WR-42 waveguide. The array reduced beam squint when compared to a reference array with the time delay compensation. The performance of the array was limited by the bandwidth of the time delays and power dividers.

The array is additively manufactured using stereolithographic apparatus printing technology and electroless silver plating to create the conductive surfaces needed for the waveguide. This work extends previous work by providing a detailed analysis of the plating performance. The silver plating was also used as a seed layer for copper plating. The manufactured parts were compared to titanium-printed versions. The silver plated parts performed better than the titanium-printed parts in terms of manufacturing cost and waveguide losses. Furthermore, the titanium printed waveguides needed post-processing to achieve the best performance. There was little benefit in performance when copper plating onto the silver with a basic copper plating approach.

LIST OF ABBREVIATIONS

ABS	Acrylonitrile Butadiene Styrene
CAD	Computer-Aided Design
CRPM	Center for Rapid Prototyping and Manufacturing
DM	Direct Metal
DMLS	Direct Metal Laser Sintering
EM	Electromagnetic
FDM	Fused Deposition Modelling
LWA	Leaky Wave Antenna
PCB	Printed Circuit Board
PEC	Perfect Electrical Conductor
RADAR	Radio Detection and Ranging
RF	Radio Frequency
SIW	Substrate Integrated Waveguide
SLA	Stereolithography
SLM	Selective Laser Melting
SSSLT	Short-short-short-load-through

TABLE OF CONTENTS

LIST OF FIGURES

LIST OF TABLES

CHAPTER 1 INTRODUCTION

1.1 PROBLEM STATEMENT

1.1.1 Context of the problem

Compact and high directivity antennas are ideal for applications such as SATCOM applications where space is limited and the radiating beam only needs to be directed in a single direction. Antenna arrays allow for an increase in antenna gain (directivity). However, antenna arrays, most notably series-fed arrays, suffer from beam squint which is a variation in the direction of the array beam as the operating frequency is varied. In series-fed arrays the paths from the input to the radiators have different lengths, leading to unequal phases at the radiators. A solution to correct the phases at the output is to use slow-wave transmission lines to equalise the time travelled to the radiating elements. This can be complex since the time delays are all different and depend on the array dimensions. It was found that slow-wave lines significantly improve the bandwidth in a microstrip array feed network. By using slow-wave lines and rectangular waveguides there is potential for more compact antenna arrays with greater design flexibility and suitable bandwidth.

1.1.2 Research gap

Existing beam squint mitigation is usually applied to series-fed antennas and rarely achieves fractional bandwidths greater than 20 %. There is little research that aims to reduce beam squint in series-fed arrays. When designing an antenna array, corporate feed networks are used because of low-cost and the parallel signal paths ensure that the phase relationship of the signal arriving at the antenna elements remains constant with frequency. The size of these arrays can grow considerably with an increasing number of antenna elements. With the advent of additive manufacturing, complex waveguide parts can be manufactured inexpensively.

1.2 RESEARCH OBJECTIVES AND QUESTIONS

Beam squint reduces the usable bandwidth of an antenna array. Current solutions require a corporate feeding strategy which adds to the complexity and increases the size of the array. Travelling wave antennas have a single input making their integration and use simpler but suffer from beam squint.

- How can series-fed arrays be designed to reduce squint over large bandwidths?
- How can additive manufacturing be used to realise low-cost, rapidly prototyped antenna arrays with low beam squint?
- What limitations are imposed by additive manufacturing on waveguide components?
- Can waveguide components be manufactured using low-cost techniques?

1.3 APPROACH

1.3.1 Design and modelling

The first phase involves the design of the array network. In this stage, the network is synthesised using the relevant literature. Literature also serves as a reference to gauge the performance of the array as well as a data source to perform a detailed design of the components required to realise the array. Simulation tools such as numerical calculation (in Python) and EM simulation (CST Microwave Studio) were used to ensure the different components performed as expected. With all the components designed simulation analyses were carried out where the parts were integrated to view the performance in simulation, which is used to verify if the array meets the design specifications.

1.3.2 Construction

The anti-beam-squint network was constructed using additive manufacturing. A Form 3 Stereolithographic (SLA) printer was used as parts with low surface roughness and high accuracy are possible, more so than those realised by fused deposition modelling. The printed components were silver plated so that the desired electrical properties are achieved. Additive manufacturing is used because it allows for fast prototyping of the network. It also increases the ease of construction but removes the need for machining. Additive manufacturing also makes it possible to quickly develop revisions of the network if needed.

1.3.3 Measurement

First, the performance of each individual component was measured using a VNA. Parts that did not achieve the desired performance were remade should the issue be related to flaws in the silver plating.

The antenna pattern measurements were completed by measuring the array in a tapered anechoic range. The two-step process in measurement allows for a more detailed measurement of the array and its constituent components to aid in interpreting array results. The far-field measurement directly verifies the radiation pattern of the array fed using the anti-beam-squint network, which indicates the in situ performance on the anti-beam-squint network.

1.4 RESEARCH GOALS

To determine how much of an improvement can be made to the beam squint in a series array manufactured using waveguide components. The network will be considered a success if the main lobe of the far-field pattern shows a significantly less amount of squint than a reference array without any anti-beam-squint. A secondary goal is to establish a reliable procedure that can be applied to manufacture waveguide components with consistent performance using additive means.

1.5 RESEARCH CONTRIBUTION

This work contributes to the design of a series-fed antenna array manufactured using waveguide components. The antenna uses sinusoidal time delay waveguides to equalise the phase at the output ports and asymmetrical T-junction power dividers to equalise the power at the output ports. This work also contributes a detailed procedure describing how to use additive manufacturing to realise the waveguide parts used here. Desktop printing equipment is used which has the advantage of being low-cost. The plating procedure extends on previous work to improve the success and reliability of the procedure.

1.6 RESEARCH OUTPUTS

- A. Simonovic, E. Rohwer and T. Stander, "Preliminary investigation into the use of silver seed layers in copper electroplating of waveguide parts," in *2022 International Conference on Electromagnetics in Advanced Applications (ICEAA)*, Cape Town, South Africa, Sep. 2022, pp. 361-364
- A. Simonovic, E. Rohwer and T. Stander, "SLA Printed K-Band Waveguide Components using Tollens Reaction Silver Plating," *IEEE Transactions on Components, Packaging and Manufacturing Technology*, vol. 13, no. 2, pp. 230 - 239, Feb. 2023
- A. Simonovic, T. Stander, A Series Fed Waveguide Horn Array with Beam Squint Reduction, *Interantional Journal of RF and Microwave Computer-Aided Engineering*, vol. 2023, May 2023

1.7 OVERVIEW OF STUDY

Chapter 2 describes the review of the literature. Chapter 3 discusses the methods used during simulation, high-level modelling and manufacturing. Chapter 3 also includes the high-level design of the antenna array. Chapter 4 describes the additive manufacturing process in detail and all the experiments that lead to the design of the final method. The performance of the additive manufacturing process is also presented there. In Chapter 5, the measurements of the manufactured components used in the antenna array and the antenna array are presented. In Chapter 6 concluding remarks are given.

CHAPTER 2 LITERATURE STUDY

2.1 INTRODUCTION

This section provides the context of antenna arrays, beam squint, and 3D printing technologies. Beam squint and possible solutions are discussed in Section 2.3. Section 2.6 discusses slow-wave waveguides that are used to solve the issue of beam squint in passive solutions. Plating technologies used to create conductive surfaces on printed plastic parts are mentioned in 2.7.

2.2 ANTENNA ARRAYS

Antenna arrays are popular because they are a simple way to shape a radiated beam for various applications [1]. Arrays are typically composed of multiple antenna elements with controlled spacing from each other and achieve pattern shaping by adjusting the amplitude and phase at the antenna elements. Antenna arrays are fed with either a series-fed network or a corporate (parallel feed) network; with corporate feeds being more common due to their simpler feeding scheme. The corporate network ensures that the paths between the input to all radiating elements are the same, keeping the phase relationship between radiating elements the same. In series-fed arrays, the path to each radiating element differs, usually only by length, leading to varying phase relationships between elements as frequency varies [2].

2.3 THE ISSUE OF BEAM SQUINT

The direction of the radiated beam in an antenna array is controlled by adjusting the phase progression of the signal between consecutive antenna elements, which changes based on the frequency of the signal [2]. For a series-fed array like those shown in Figure 2.1, the array input is connected to what is known as the feed line. The feed line distributes the input wave to the output and the antennas, while also controlling the power that arrives at each port. The lines between the feed line and the antennas are known as branch lines and are responsible for connecting the antenna elements to the feed line. The spacing between antenna elements, d_E, is typically constant, which makes the design of these arrays

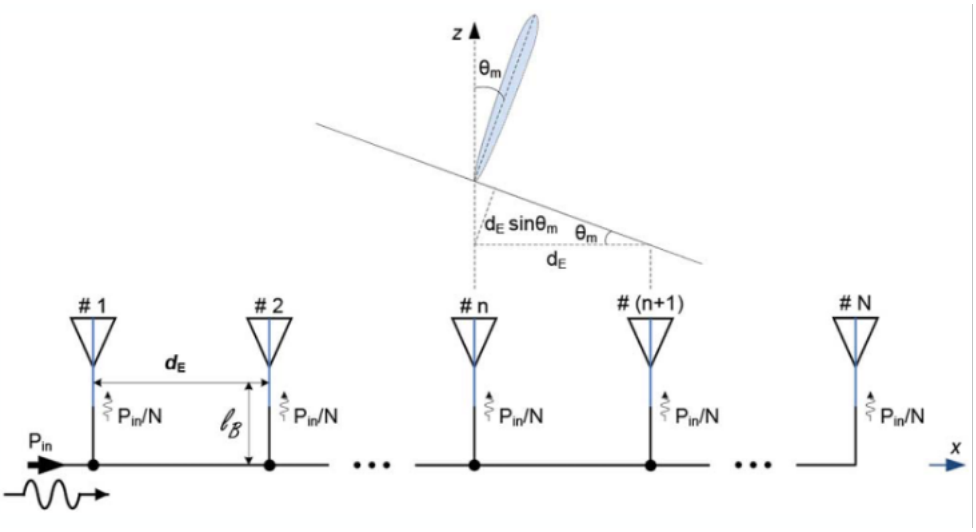

Figure 2.1. An N element series fed array. Taken from [2] , ©2023, IEEE.

much simpler. The phase relationship between antenna elements is written as a phase progression, which is the same along the line if the spacing between elements is the same. The phase progression is found in [2, 3, 4] as

$$\Delta\phi = \beta_0 d_E \sin(\theta_m), \tag{2.1}$$

where β_0 is the propagation constant of free space and is sometimes written as k_0. The direction of the beam is θ_m, and $\Delta\phi$ is the phase progression. The phase progression determines the angle of the beam and is dependent on the instantaneous frequency of the transmitted signal. Note the dependency of beam-steering angle on frequency; this is referred to as beam squint. The cause of beam squint is visible in (2.1), for a constant θ_m and a varying frequency, β changes, leading to the required phase progression to vary with frequency, which leads to the beam being squinted. One solution that reduces beam squint is to create a feedline capable of superluminal propagation [2, 3, 5]. The equation for the required phase velocity in the series feed network is given in [2] as

$$v_p = \frac{c}{\sin(\theta_m)}. \tag{2.2}$$

It is evident in (2.2) that the phase velocity required in the feed line will always be greater than the speed of light, known as superluminal propagation. An alternate solution is to apply squint in the opposite direction, correcting the squint [6]. Another solution to equalise the phase at the radiating elements is to delay the wave going to each element so that the input wave arrives at the radiating elements at the same time. The required delay would be different for each element. All of the solutions mentioned above will be discussed in detail in the following sections.

2.3.1 Beam squint in leaky wave antennas

Leaky wave antennas also exhibit beam squint. Power is radiated from these antennas by leaking energy as it travels along the guide. These antennas can be integrated using microstrip lines and closed waveguides [7, 8]. For closed waveguides, the direction of the radiated beam is dependent on the propagation constant in the waveguide and free space. In the case when speeds faster than light are possible, providing a positive k_p, the angle of the beam would not vary with frequency. The second case is when the wave is slower than light leading to an imaginary k_p. The propagation constant needs to be real for the radiated energy to propagate. The propagation constant can be found based on the free space wavenumber, and the propagation constant in the guide

$$k_p = \sqrt{k_0^2 - \beta^2}. \tag{2.3}$$

There are then two cases to consider. The first is to improve the phase-matching condition at the boundary of the waveguide. One such technique is the use of periodic scatterers. Practically these are implemented as radiating slots in the waveguide where the slots allow energy to propagate through. In this case, the beam angle is found using

$$\theta = \sin^{-1}\left(\frac{\beta}{k_0} - n\frac{k_p}{k_0}\right), \tag{2.4}$$

where k_p is the wavenumber of the signal inside the waveguide and P is the period of the scatterers

$$k_p = \frac{2\pi}{P}. \tag{2.5}$$

Thus when observing (2.4) and (2.5), the only constant with frequency is k_p, which is the cause of beam squint when using travelling wave antennas. In the case of a fast wave, there are no periodic scatterers; thus the beam angle is dependent solely on the ratio of the propagation constant in the waveguide and free space [9] and [8]. For the ratio of the propagation constant in the waveguide and free space to stay constant, a dispersionless line is required; otherwise, β would vary, leading to a change in the beam angle. Thus, two broad solutions exist for solving beam squint in travelling wave antennas. These are to fabricate a guide that allows dispersionless superluminal propagation or add some squint correction that counteracts the beam squint. Non-Foster loading of non-planar waveguides such as travelling wave antennas is impractical due to the difficulties in integrating the non-Foster components [9]. Ideally, one would want to fill the waveguide with a material that has a permittivity of less than 1. An alternative is a waveguide transition like that in [10], where SIW to coplanar transition is discussed. These transitions introduce non-idealities that are difficult to model.

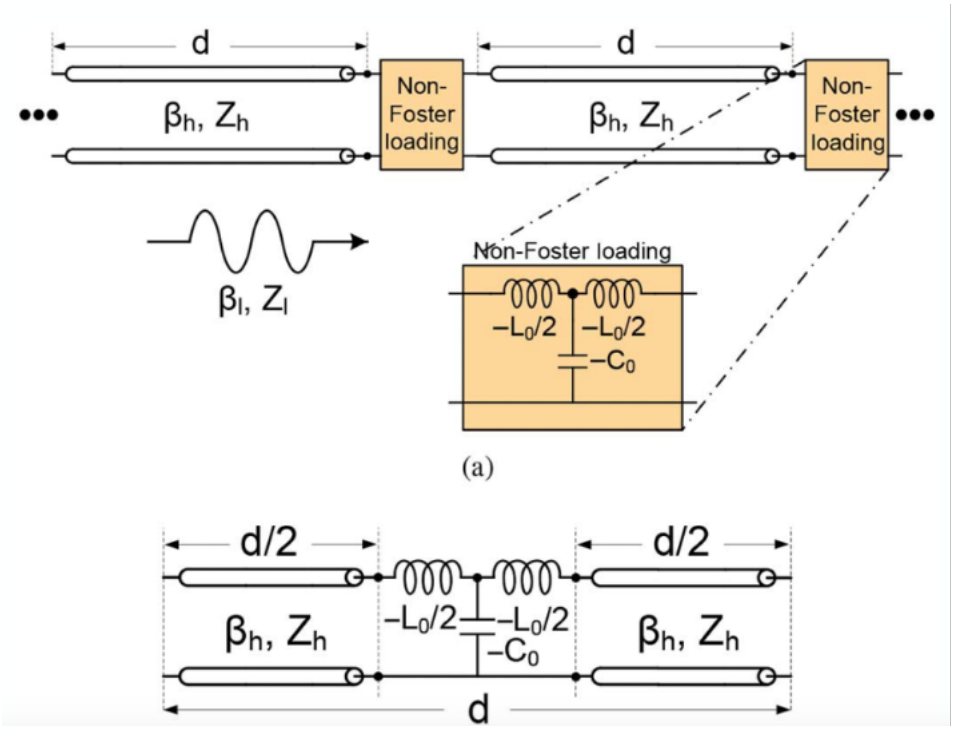

Figure 2.2. A transmission line is broken into unit cells of length d. The non-Foster elements are inserted into each cell. β_h and Z_h are the original line's propagation constant and characteristic impedance. L_0 and C_0 are the non-Foster capacitances and inductances. Taken from [2] , ©2023, IEEE.

2.4 NEGATIVE GROUP DELAY

Negative group delay is a method that can be used to achieve superluminal propagation [11]. The balance between bandwidth and stability is the significant difficulty with circuits that allow for superluminal propagation. Achieving negative group delay requires loading the array feed line with negative inductances and negative capacitances, known as non-Foster circuits. This method is described in [2, 9, 12, 13]. From the expression for β, taken from [14], relates propagation velocity and frequency as

$$\beta = \frac{2\pi f}{v_p}. \tag{2.6}$$

It is evident that superluminal propagation can be achieved by decreasing β. Loading the transmission line with negative inductances and negative capacitances causes the wave to propagate as if the effective dielectric constant ranges between zero and one. Figure 2.2 from [2] best illustrates the loading of the transmission line. The propagation constant of the line made up of the non-Foster elements is found using

$$\beta_l = \omega\sqrt{\left(L - \frac{L_0}{d}\right)\left(C - \frac{C_o}{d}\right)}. \tag{2.7}$$

The propagation constant of the line can be reduced by reducing the reactance of the line. This is achieved by adjusting L_0 and C_0 so that they cancel out the inductance and capacitance of the line. A significant issue for non-Foster circuits is stability. As mentioned in [15], a non-Foster loaded waveguide is potentially unstable. A stability analysis for non-Foster circuits was performed in [16], where it was found that increasing the number of unit cells in a line creates more stringent requirements for stability. This instability results from a negative impedance in the non-Foster circuit that causes the propagating wave to grow. Furthermore, the stability of the circuit is ensured at the expense of the bandwidth of the circuit, leading to less squint-free bandwidth. Another concern when using non-Foster elements is that since they are loaded periodically, the line parameters can vary slightly between periods. The issue can be mitigated by keeping the period of the unit cells smaller than the wavelength. The issue is reported in [9], which mentions that the issue cannot be entirely removed. Thus, limits are placed on the distance and, consequently, the size of the antenna array. Removing all variation in line parameters would require the distance between unit cells to be zero or an effective dielectric constant between 0 and 1. Some of the best achievements in the squint-free network were demonstrated in [9], [17]. These networks showed bandwidths of 40%.

2.5 PASSIVE SOLUTIONS

There is limited literature making use of passive circuits to implement superluminal lines. While there are passive circuits that achieve superluminal propagation, they work by operating at or near their resonant point, leading to a significant amount of dispersion [11]. While it is possible to design dispersion compensation networks [18], [19], the bandwidth of passive superluminal transmission lines and metamaterials is narrow [20], leading to the main reason for the use of active circuits. Two forms of passive squint correction are discussed here. The first is the compensation lens, which reduces squint by squinting the beam in the opposite direction to the array squint; the second is the use of delay equalisation in array branches.

2.5.1 Compensation lenses

Metasurfaces are used as the corrective lens. These metasurfaces possess a frequency-dependent law of refraction. In [21], a metasurface is designed to remove beam squint in a planar antenna. Where Φ is the phase discontinuity on the interface, an incident wave with an angle θ_i is refracted to θ_t as described by

$$\sin(\theta_t) = \frac{c}{2\pi f}\frac{d\Phi}{dx} - \sin(\theta_i). \tag{2.8}$$

The reduction in beam squint is achieved by designing the antenna so that the two terms in (2.8) are opposite. Equation (2.8) is specific to the problem in [21] for it depends on the metasurface's

construction. Thus, a complete metamaterial analysis cannot be easily presented. However, the approaches are based on (2.8).

Another popular solution for reducing beam squint is the use of compensation lenses. This is done by placing some lens-like apparatus at the antenna's output. This lens counteracts the beam squint by causing a squint in the opposite direction. The lens dielectric properties and geometry control the squint. A dispersive lens and the waveguide were designed, that, when combined, the characteristics of each cancel out, reducing the amount of squint. In [6], a compensation lens was placed at the output of a substrate-integrated waveguide (SIW) leaky wave antenna. In this work, the dispersion of the leaky wave antenna is compared to the dispersion of a periodic structure composed of vias.

The beam squint reduction in [6] reduced the amount squint to less than 1° for a frequency range of 33 GHz to 38 GHz. While this method yielded good results, it requires that the dispersive characteristics of the antenna can be counteracted by a suitable dispersive lens, which may not be the case for all array types. In [22], the works of [21] and [6] are combined. The aim was to reduce the change in dispersion with frequency and to achieve the desired propagation constant so that a specific angle of radiation could be realised. In [23] a prism dielectric lens is placed over the radiating side of a leaky wave antenna. The opposite squint is achieved by controlling the refractive index of the lens. In [24], the lens is implemented as a bed of nails. In [22], a similar leaky wave antenna is designed but uses glide-symmetric holes, while an alternate design uses Substrate Integrated Holes (SIH). The SIH antenna achieved a 20% bandwidth with a 2° variation in beam angle. The work in [21] achieved 12° of beam squint over a 10% bandwidth at a frequency of 10 GHz. This corresponds to a 50% reduction with the original antenna possessing a squint of 23.5 $^\circ$. In [22], two cases of meta-material lenses are presented. The first had achieved 1.5° at 10 GHz over 20% bandwidth while radiating at an angle of 40°. The second radiated towards the broadside with a bandwidth of 18%. Radiation towards the broadside ($\theta_m = 0^\circ$) in the non-Foster approach is a significant challenge because, in the ideal sense, it requires an infinite guided velocity. This is an advantage when using the method of compensating the beam direction.

A second but more significant advantage is the absence of non-Foster circuits operating at K-band, for which very little literature exists.

2.5.2 Delay equalisation

In [25], an alternate analysis of the beam squint issue is carried out. Most analyses of the problem fix the characteristics of the feed branches such that they are all the same, thus only allowing for the solution by adjusting the feed line. It was found that passive solutions to beam squint could be found by allowing the branches' characteristics to change. Two solutions were presented in [25]. The first solution varies the length of the branches while keeping the propagation constant of the branches the same. The angle of the beam is then controlled by adjusting the difference in length (Δl) between two antenna elements

$$\Delta l = l_n - l_{n+1} = d_E \left(1 - \frac{\sin\theta_m}{\sqrt{\varepsilon_{eff}}}\right), \tag{2.9}$$

where l_n is the length of the n^{th} branch and $l_n + 1$ is the consecutive branch. The only rule that needs to be adhered to is that the ratio of the propagation constant in the line and the free space wavenumber should be consistent with frequency. This method could eliminate the size advantage the series-fed arrays have due to the increase in the length of the branches, especially for an array with multiple elements. The second approach in [25] varies the propagation constant while keeping the line length constant. Thus, keeping the physical size of the network constant at the expense of complexity. The progression of the propagation constant between consecutive branches can be described using

$$\Delta\beta = \beta_n - \beta_{n+1} = \frac{d_E}{l}\left(\beta - \beta_0 \times \sin\theta_m\right), \tag{2.10}$$

where β is the propagation constant in the branch furthest away from the input and β_0 is the free space phase constant. This solution requires that the propagation constants in the branches change linearly with frequency and this behaviour is synthesised with time delays. Both methods mentioned here were physically realised in [25]. The implementation of varying branch lengths achieved a beam angle variation of 2° with a fractional bandwidth of 160% operating at a maximum frequency of 5GHz. This implementation shows a much larger bandwidth than any of the other approaches mentioned thus far. What is particularly advantageous about this approach is its ease of implementation at high frequencies. The second approach of variable propagation constants showed an offset in the desired beam angle but was still constant over the same bandwidth of 160%.

2.6 SLOW-WAVE WAVEGUIDE

In [26], a waveguide known as Fakir's Bed of Nails is presented. This waveguide uses nail-like protrusions from the top and bottom walls of the waveguide to achieve a slow-wave effect. In this waveguide, the time delay is controlled using the spacing between the nails. A challenge with a waveguide based on Fakir's Bed of Nails is that the tolerance requirement becomes more stringent at higher frequencies, making manufacturing more difficult. A rectangular waveguide with a helical

groove is presented in [27]. This waveguide has a fin that creates a helical groove. An advantage of the helical groove waveguide is that it has reduced dispersion leading to a group delay that is flatter for wider bandwidth. Another advantage of this slow wave structure is that there are fewer losses. When manufacturing the waveguide using an additive process, care must be taken to orientate the waveguide in a way that negates the need for internal supports that can roughen the inner surface and degrade performance. The Sin Waveguide is presented in [28]. This structure uses sinusoidal ridges on the top and bottom walls to create a time delay. The sinusoidal waveguide also has very low loss and reflection. This waveguide benefits from being simple to manufacture using additive processes because of the lack of complex geometry inside the waveguide. Another advantage of the sinusoidal waveguide is that its frequency response looks similar to the bandpass response, which can aid in isolating only desired signals.

2.7 ADDITIVELY MANUFACTURED WAVEGUIDE PLATING

Additively manufactured waveguides are becoming popular due to their reduced weight, fast manufacturing time and reduced cost. Most low-cost additive manufacturing uses plastic to realise the printed parts. Plastic is a poor conductor, so post-processing steps are required to create a conductive finish. For RF, the plating thickness does not need to be more than three skin depths due to most of the currents travelling along the surface of a conductor at high frequencies.

2.7.1 Printing technologies

By far, the most popular method of manufacturing waveguide parts was with a subtractive process such as machining. Machining can be applied to multiple materials, such as copper, brass and titanium. For parts with internal geometries, the subtractive process requires that the machine tool has access to internal sections of the waveguide. Otherwise, the waveguide is manufactured in halves and assembled. Machining can be expensive because of the complex equipment and the cost of the stock material, of which much is cut away in the machining process.

FDM printing is a popular low cost 3D printing method that additively manufactures parts using extruded plastics [29]. FDM printing can use multiple plastic types, including ABS, which benefits from existing knowledge where it has been commonly used in plated plastic applications [30]. DM printing is less precise than other printing technologies [29]. In [31, 32], FDM was used to manufacture waveguide filters and waveguide sections at X-band and W-band. Despite some successful applications of FDM printing of waveguide parts, FDM is one of the least accurate printing processes available

Stereolithographic printing (SLA) selectively cures a resin using UV light to create printed parts. SLA printing can produce a smoother part with a smaller feature size, which is advantageous at high frequencies where component dimensions are small. In [29], a W-band waveguide filter with an iris thickness of 200 μ is presented, demonstrating an unloaded quality factor of 152. A sensitivity analysis of an SLA printed split-block WR-75 seventh-order low pass filter is conducted in [33]. The AM process achieved a good yield of 96% for the low pass filter, which had a reflection coefficient of -20 dB and a stopband of 60 dB. Printing inaccuracies in a waveguide hybrid coupler are presented in [34]. This work shows the difficulties with manufacturing small dimensions, in particular, the size of curved cylindrical posts. When the post diameter was too small (0.2 mm), there was a significant distortion of the posts, which was improved by making the diameter of the posts 0.42 mm. This work also shows that parts printed with a 10° had more distortion than those printed at 30°, supporting that parts printed at inclinations have less distortion. In [35], an SLA-printed Rotman lens that operates at 6-10 GHz is presented. This lens produces multiple beams. The beam scanning is controlled by adjusting the input power at the port that corresponds to the beam. The lens is large and comprises a top and bottom which are assembled. This work shows that lenses can be large and complex necessitating multiple sub-components. The weight advantage of AM reduced the weight of the lenses by 33% when compared to the same lens made from aluminium. When comparing FDM printing to SLA printing, SLA is more costly due to the higher complexity of the equipment. SLA printing also requires extra post-processing steps, such as rinsing to remove uncured resin and curing to ensure the resin has fully hardened. SLA printed waveguides typically have limited power capability because of the plastic base material [36].

While FDM and SLA printers are relatively low cost, waveguide components require a conductive surface finish, necessitating post-processing steps that metallise the parts. Direct Metal Laser Sintering DMLS (also referred to as Selective Laser Melting (SLM)) is a process that uses metal powder and a high-power laser to manufacture parts out of metal, requiring no post-processing steps [37]. The process melts patterns into layers of metal powder that make up the object. This process has the advantage that parts do not need any metallisation layers added after printing which is a significant advantage when a component has inaccessible internal features. The process does suffer from some poorer surface roughness leading to an increase in losses [38, 29]. Another disadvantage of metal printing is that it is still expensive compared to other additive manufacturing technologies. In [29] rectangular metal waveguide was printed and then copper plated to improve the surface roughness.

The performance of the printed waveguide was almost identical, except that the printed waveguide had slightly more loss. A similar result was found in the same work when testing the process on a W-Band Iris filter. When comparing the measured results to the simulation, there was a greater insertion loss while the filter profile remained the same. In [38], a copper waveguide for E and D bands was printed. When compared to machined waveguides, there was an increase in losses, but they were comparable to non-metallic waveguides. In [39], a cavity bandpass filter was manufactured using metal printing. The filter's behaviour resembled the simulated results, but accuracy and surface finish limited the ability to match the simulated results closely. In [40] and [41], waveguide horns are manufactured using DMLS printing. In both cases, surface roughness was greater than SLA printing. In [42], V and W-band splitters were manufactured. Splitters made of an $AlSi_{10}Mg$ alloy did not work due to poor tolerances in printed parts. The issue is believed to be caused by the small dimension of the septum, which is comparable to the particle size of the metal powder used in manufacturing. The design of the splitter is complex and would not be able to be manufactured using traditional milling, showing the advantage of using additive manufacturing.

Binder jetting is an approach that also uses a powder material to make up the part, except that the printer selectively deposits a binder to solidify powder. The advantage is that parts can be made from multiple materials, such as plastic or metal. Metal binder jetting uses a stainless steel powder as the base material. After printing and curing, the part is placed in a crucible with an infiltrated metal powder with a lower melting point than the base stainless steel. The binder is burned off and the metal infiltrate melts; this is then absorbed into the pores of the base material to create a part that is completely solid [43]. In [43], a WR-28 waveguide is manufactured, achieving a loss of 4.3 dB/m. A WR-28 Filter and a WR-28 horn with a parabolic reflector are made. The filter achieved an in-band loss of 0.71 dB but the response was shifted down by 350 MHz as the waveguide had slightly larger cavities caused by printing accuracy. The reflector antenna achieved a peak gain of 24.77 dBi, which was 0.48 dB less than the simulation, with more significant discrepancies at the lower band edge. In [36], meshed waveguides are manufactured with metal binder jetting. The waveguide achieved a transmission loss of 2.9 dB/m while a solid waveguide achieved a loss of 1.34 dB/m. All waveguides achieved return losses below 30 dB. The parts had an average roughness (R_a) of 6.37 μm, which was a major contributor to the observed losses.

2.7.2 Plating technologies

Metal plating approaches typically fall into two categories: electroplating and electroless plating [44]. Electroplating uses an electric current to facilitate the reduction of a metal solution to form a metal on a part. Electroless plating relies only on an electrolytic reduction-oxidation reaction between chemicals to form metal [45]. A disadvantage of electroplating is that it requires that the part being plated is already conductive to facilitate electric current flow. For this reason, electroplating is typically used when increasing the metallisation layer, not to create one [45] and is often used after electroless plating to increase the metal thickness [44, 46, 47, 48].

At mm-Wave frequencies, the currents induced by the propagating wave remain near the surface of the conductor [14]. This means that as long as there is a sufficiently thick layer of good conducting material, there is an insignificant amount of loss. The skin depth (δ) defines the thickness where the amplitudes of the currents travelling along a conductor decrease by 36.8%. For the case of five skin depths, 99.3% of the conducting wave is contained in the conducting material. Conductors that are too thin result in a lossy waveguide. The skin depth is found using

$$\delta = \sqrt{\frac{2}{\omega\mu\sigma}}, \tag{2.11}$$

where f is the frequency of the wave, μ is the magnetic permeability of material, σ is the conductivity of the conducting material and ρ is the resistivity of the material [14].

2.7.2.1 Electroplating

Electroplating is the most common method in industry to plate a metal layer onto an object. Electroplating uses an electric current and a metal in solution to deposit a metal layer on the item being plated. Simple copper plating solutions result in dull copper due to surface roughness. Surface roughness can be improved using brighteners such as chloride ions. These chemicals assist by levelling the plated copper surface, leaving a smoother surface with a shiny finish. The geometry can make electroplating less effective because the electric field strength inside shapes and around corners is lower than outside surfaces, resulting in reduced plating. To solve this issue, slots are created in the waveguide walls to facilitate current flow to the inside of the waveguide [48, 49]. Another solution is to use supplemental anodes placed inside the waveguide to increase electric field strength inside the waveguide [45, 46, 48]. In [47], waveguide sections and an antenna horn are printed as halves and assembled similarly to split-block assemblies. However, the work in [32] shows that losses are incurred when splitting the waveguide, with E-plane cuts being a better choice than H-plane cuts.

Both components performed nearly identically to their off-the-shelf counterparts. In [46], a slot array is printed as a single piece composed of nine slotted waveguide sections. The difference in gain between the simulation and the measured array was 2.3%. A disadvantage of electroplating is that it requires that the base material being plated is conductive. As a result of this, electroplating thickens the metal layer after electroless plating has created a seed layer.

2.7.2.2 Electroless plating

The electroless reactions use palladium or nickel to create a catalytic surface on the plated part. The palladium then allows the metal from an electroless plating solution to form on the surface of the printed part [30]. Electroless plating has the advantage that the inside of tubes is also plated [50, 49, 30, 46]. The process may begin with some surface roughening to increase the success of plating and is usually done chemically using a strong oxidiser. This renders the surface hydrophilic, allowing a palladium colloid, used as a catalyst in the electroless reaction, to be absorbed onto the part's surface. Once the surface has absorbed the palladium catalyst, it is placed in the electroless plating solution. In this step, the metal layer forms on the part's surface due to a reaction between the electroless plating solution and the catalytic palladium. The disadvantage of this process is achieving the desired thickness. Once there is a layer of metal around the part, there is no longer palladium exposed to the plating solution, ending the plating process. Thickening the metal layer must be done using other methods, such as electroplating. In [50], the thickness of the metal layer varied between 4 µm to 5 µm. In [51], an electroless nickel layer of 5 µm was achieved. The etching process used in some electroless plating is a major contributor to the overall characteristics of the plating process. Typically chromic acid (Cr_6^+) is used, which is highly toxic [30, 52]. Due to the toxicity, there have been many inquiries into alternate chemicals for etching. In [52] KM_nO_4 is reported. Hydrochloric acid has been successfully used in [50]. Sandblasting is also used [53]. Where external access to surfaces that require plating is difficult or impossible, chemical etching is preferred to sandblasting.

A novel solution developed by Jet Metal™ sprays a metal solution and a catalyst simultaneously on plastic parts to create a metal surface finish [54]. This process was used in [55] to produce a rotary vane attenuator. The performance of the additively manufactured attenuator compared well to the simulated results with an S_{21} error of 0.3 dB. A disadvantage of this process is that the spray application makes it less suitable for coating inside surfaces [37]. A 384-slot conformal array was created using the spray process and was shown to have a good agreement with simulations [56].

Sputtering is a technique that deposits a metal by bombarding the surface with metal atoms [57]. This process has the advantage that it can be applied to a variety of material types. In [58], a waveguide based dipole antenna is manufactured. Copper sputtering is used to deposit a seed layer into 3D printed parts. As sputtering generates heat, the part is only sputtered for 2 minutes; otherwise, deformation due to heat can occur. The copper layer is then used for electroplating to thicken the metal layer. The dipole antenna in [58] closely matches the simulated results, which had a 4.6 % smaller bandwidth and a difference in gain of 0.1 dB. A similar approach is used in [59], which uses titanium and copper sputtering to create a 0.1 µm titanium layer followed by a 0.5 µm layer of copper, which improves adhesion to the plastic part. Copper electroplating is added to thicken the plated surface by another 6 µm. In this work, a Vivaldi antenna with a SIW transition was manufactured. The 1 dB difference between simulated and measured gain was attributed to calibration tolerance. In [60], a travelling wave tube operating at W and D-band is presented. Gold sputtering deposits a seed layer, later used for electroplating copper to thicken the metal layer. The results showed that the measured results were comparable to smooth wall simulations. The waveguide was manufactured in two halves to allow for sputtering inside and electroplating. In all cases, electroplating is followed to thicken the metal later because the time for copper sputtering is limited by the temperature the printed parts can withstand. Copper sputtering also requires complex machinery, rendering it not easily accessible.

In [32, 31], a conductive spray paint creates a conductive layer on two halves of waveguide filters. The spray paint is a poor conductor and is only used to create a seed layer for electroplating. In both cases, the filters achieved insertion losses lower than -20 dB and passband losses lower than 1 dB. Mismatch in the filter shape was attributed to the printing accuracy and cut required to manufacture the filter in two halves. In [61], a commercial nickel spray is used to create a seed layer for electroplating. Loss exceeded 10 dB/cm at Ka-band without electroplating, showing that electroplating the parts after the spray coating is necessary. Waveguide straight sections were manufactured with a loss of 1.05 dB/m at Ka-band and 4.3 dB/m at W-band.

In [62], an electroless plating process that does not require etching is developed. This process is based on the Tollens reaction, where a silver layer is produced inside glass beakers. This process requires silver nitrate, ammonium hydroxide, dextrose and water. The process was tested at 75-110 GHz with WR-10 waveguide [62]. Results showed a maximum loss of 20 dB/m. The exact process was tested in [49] and has subsequently been applied to a waveguide to microstrip transition operating at 70 GHz [63] and a slotted waveguide in [64]. A loss of 10 dB per metre was

reported. This process is advantageous because it does not use toxic chemicals like chromic acid. This process has been applied to microwave components operating at V-band and E-band. However, no work provides an in-depth review of this process and there is no mention of the plating thickness and limitations, such as its potential to be applied to waveguide tubes which can be difficult to plate and at lower frequencies.

2.8 SUMMARY AND FOUNDATION FOR THIS WORK

The issue of beam squint is well-known and has multiple solutions. Non-Foster circuits are limited by their stability which decreases proportionally with an increase in the number of non-Foster elements. Furthermore, the criteria for stability make the design of non-Foster circuits very difficult. Passive approaches typically use special lenses to correct the beam squint, which is complex, bulky and difficult to manufacture or repair. No work uses classical waveguides that are simple to manufacture to mitigate against beam squint. Multiple processes can be used for the additive manufacture of waveguides. The most popular approach is copper plating with an electroless metal deposition to create a seed layer for electroplating. This gives a good finish with a controllable copper thickness, but the application is complex. The deposition of a seed layer is highly dependent on the base material and can be costly depending on the metals used. Alternatives such as metal spray solutions are convenient since the application method is more straightforward. However, spray applications cannot cover parts with internal geometries without splitting the geometry. Spray applications are also commercialised, making them costly and decreasing turnaround time. Electroless silver plating with Tollens reaction proves to be a viable manufacturing method for 70 GHz waveguide application. The process is inexpensive and is not hazardous, making its application simple.

CHAPTER 3 METHODS

3.1 OVERVIEW

The study commenced with a literature review that necessitated identification of a suitable approach to mitigate beam squint in series-fed arrays and how to apply additive manufacturing to create waveguide parts. A passive approach to mitigating beam squint was chosen for it is more suited for passive waveguides, which are more simply realised using additive manufacturing. The design of the anti-beam-squint array began with a high-level design, where theoretical calculations were used to gain insight into the array's feasibility and to aid in selecting component topologies that could realise the required performance. Each component was designed and simulated, ensuring they reached the desired performance metrics. A system-level simulation was performed to verify the array performance, followed by full 3D EM modelling. Components were selected based on their feasibility of manufacturing. The manufacturing approach was chosen from the literature study. When a suitable approach was found, modifications to the parts and manufacturing approach were applied to take advantage of the approach. This was followed by formal manufacturing, where the components required to create the array were manufactured for measurement. After measurement results were available, the performance was compared to the simulated performance and conclusions were drawn.

3.2 THEORETICAL DESIGN

3.2.1 High-level system design

The theory of system design is based on the work done in [25]. A system diagram is shown in Figure 3.1. The network has a single input, four outputs and three power dividers (PD). For this work, the number of outputs has been chosen as four. The desired array pattern is a broadside array firing perpendicular to the array. The network works by equalising the time delay between the input port and each output port. This produces the same phase and power at the ports of the feed network. Time delay (t_{d1-3}) can be achieved by increasing the length of transmission lines, but this is only sometimes

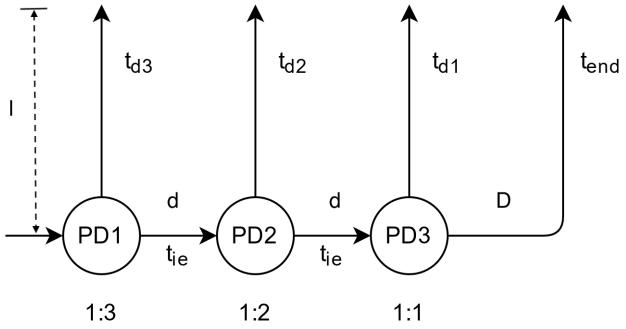

Figure 3.1. High-level system diagram.

feasible when the physical geometry is important, such as in the case of antenna arrays. The time delays can be calculated by relating the travel time between the input and the end antenna to the input and the other antennas. The time for the wave to travel to the end port is given by

$$t_{end} + 2t_{ie}. \tag{3.1}$$

The time taken to the third port is given by

$$t_{d1} + 2t_{ie}. \tag{3.2}$$

Relating (3.1) and (3.2) gives

$$t_{d1} = t_{end}. \tag{3.3}$$

The symbol t_{end} is the travel time between power divider three (PD3) and output four. The travel time between power dividers is t_{ie}. The values for t_2 and t_3 are found similarly as

$$t_{d2} = t_{end} + t_{ie} \tag{3.4}$$

and

$$t_{d3} = t_{end} + 2t_{ie}. \tag{3.5}$$

As the lengths of the branches cannot be easily varied without changing the antenna geometry, the propagation velocity needs to be adjusted. Instead of using time delay, the required propagation velocity of the time delay element can be calculated for the case where the time delay elements are the same length. The propagation velocity of the wave in a standard waveguide is v_p, and v_n is the propagation velocity in the time delay elements. Equation (3.5) can then be written as

$$\frac{v_{p3}}{v_p} = l\left(\frac{1}{D} + 2\frac{1}{d}\right) \tag{3.6}$$

to provide the velocity fraction for the first time delay, where l is the length of the time delay elements, D is the length from PD3 to the fourth antenna, and d is the length between power dividers. The velocity fraction of the time delay 1 (t_{d1}) can then be found as (3.8). In this case, the time delays are

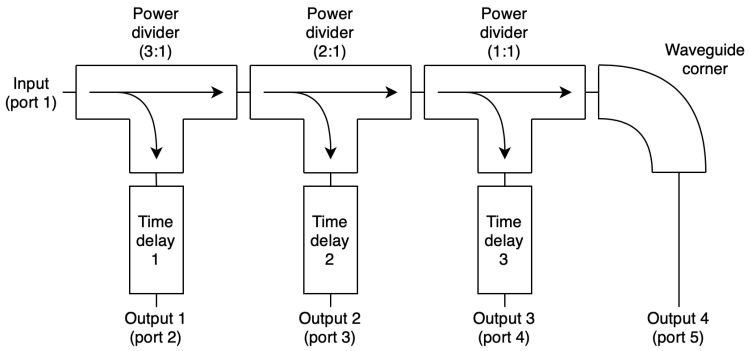

Figure 3.2. Concept circuit diagram using ideal components.

assumed to be perpendicular to the feed line, with all ports spaced at an equal distance from the feed line. The velocity fraction for the second time delay is given by

$$\frac{v_{p2}}{v_p} = l\left(\frac{1}{D} + 1\frac{1}{d}\right). \tag{3.7}$$

The velocity fraction for the third time delay is given by

$$\frac{v_{p1}}{v_p} = \frac{l}{D}. \tag{3.8}$$

3.3 PERFORMANCE MODELLING

3.3.1 High-level modelling

Cadence VSS was used to perform the proof of concept modelling. The first design used ideal components for time delays and power dividers provided by the VSS environment. The ideal circuit model is shown in Figure 3.2, created as a circuit schematic. The ideal design was used to verify theoretical calculations emphasising the time delays and the phases at the outputs. The S-parameter information was then used in post-processing to calculate the array factor. With design variables confirmed in AWR, the next step is to design the parts in an EM simulator.

3.3.2 EM modelling

3.3.2.1 Solver setup

All EM modelling was performed in CST Microwave Studio. The frequency span of the waveguide components was set to 18 - 27 GHz. A time domain Transient solver was used because it is well suited for wideband tasks. CST documentation recommends that this solver be used for applications involving connectors, transmission lines, antennas and non-resonant filters. The solver can analyse scattering parameters, E and H-field and far-field. The time domain solver is not recommended for problems that consist of resonant structures due to long settling times. The time domain solver was chosen over the

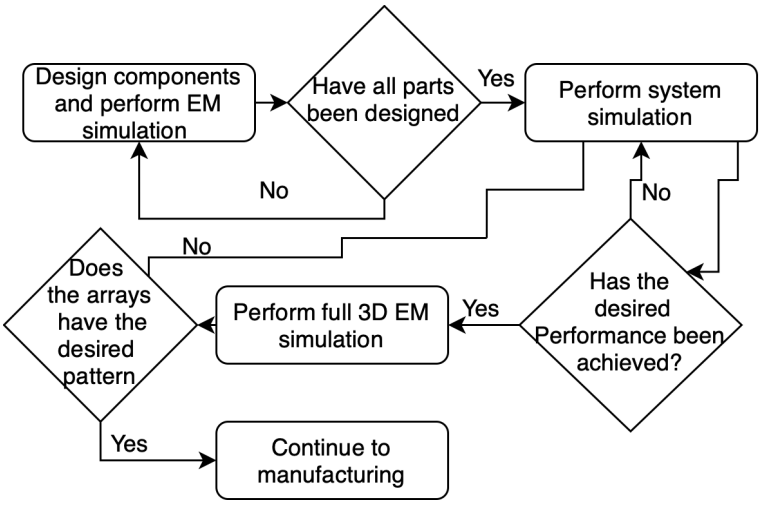

Figure 3.3. Flow diagram of the EM modelling.

frequency domain solver, which is better for solving resonant structures. In contrast, using a Gaussian pulse excitation, a time domain solver can measure broadband behaviour with a single run.

3.3.2.2 Part construction

Initial designs used a background medium of PEC with only the open-air volumes being captured. Modelling this way is similar to a negative mould and improves simulation time. However, considering all geometry needed to be exported for printing, this was changed for the final part designs. The final designs used a vacuum background and the part structures were modelled. This allowed for parts to be exported directly from the EM simulator to printer slicing software. This does increase simulation time because there is more geometry to simulate. However, the advantage is that the integrity of the parts is ensured since they do not need any post-processing and can be exported directly to the printing slicer.

3.3.2.3 EM modelling flow

EM modelling was broken into three steps. The first step involved constructing the parts and tuning them until the desired performance was achieved. For the power divider, the key results were S-parameter data to verify the power split. The time delays were evaluated using S-parameters and group delay. The horn antenna was evaluated using far-field measurements to visualise the antenna pattern and measure the gain. Once the behaviour of the parts has been modelled, a system simulation is performed. This simulation uses the cascaded responses of individually simulated parts to simulate the S-parameters at the output of the feed network. Each part is imported as a component for this simulation and connected like circuit components. The advantage of this is that changes can be quickly

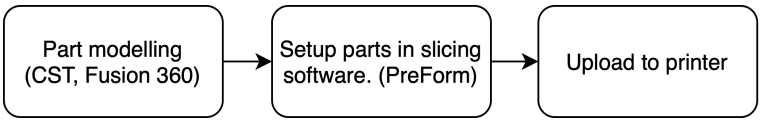

Figure 3.4. Process flow of part modelling up to printing.

applied to a single part without the need to re-simulate other parts. The disadvantage is that EM interactions are not fully modelled. This was done to verify the phases at the outputs of the antenna array. Tuning the time delays was more manageable since only the time delays that were changed needed to be re-simulated. After the time delays were tuned, a full 3D EM simulation was performed to measure the far-field pattern of the array. This was achieved by assembling the array in CST using the designed individual parts. All parts were imported as SAB file formats since it is less computationally intensive than working with STL files.

3.4 MANUFACTURING OVERVIEW

3.4.1 Printing equipment and process

All printing was completed on an SLA printer due to the improved accuracy and finish. A Formlabs Form 3 printer was used; and white Formlabs resin was used, having been suggested by the manufacturer to be used as a base for parts that undergo post-processing. A clear resin was also attempted because of its improved layer resolution of 25 µm, which could produce more accurate parts but did not plate well, as discussed in Chapter 4. All parts were rinsed in isopropanol and cured in a Formlabs UV chamber. The manufacturer recommends these steps after any print is complete.

3.4.2 CAD design flow

The process of modelling a part in CAD and preparing it for printing was kept intentionally short. This meant that design files had to pass through as few software packages as possible before it was uploaded to the printer. The modelling and EM simulation, performed in CST Microwave Studio, produced geometry which should remain unaltered through the prototyping process. If any changes happened to the geometry after modelling, these changes would not be accounted for in the simulation. As a result of this, no modelling changes were made outside the CST environment. Parts were exported from CST as STL files which describe parts using a triangular mesh. By default, the accuracy that CST exports a mesh is low, which will cause variation in parts that have curved surfaces. For all parts of this work, the resolution of STL files was set to the highest value possible. This was especially important for the time delay waveguide sections with sinusoidal geometry. These settings are available at export. It is worth noting that increasing the resolution can significantly increase file sizes; in these cases,

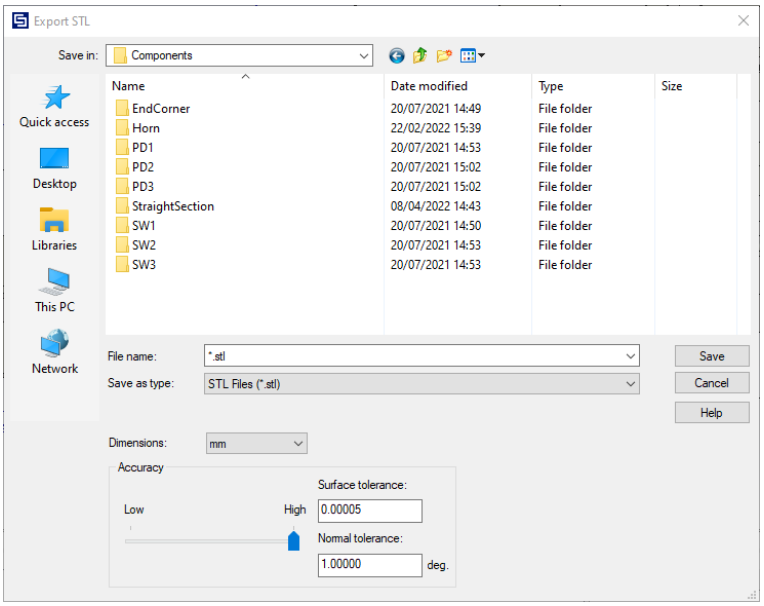

Figure 3.5. CST export dialogue where the resolution can be set for the exported file.

files were as large as 100 megabytes. When exporting from CST, it is possible to export a component as a single 3D model, which is prone to cause mesh errors. The resolution setting is adjusted when exporting the model, shown in Figure 3.5. Mesh errors can occur when multiple bodies are exported as a single STL, meaning it is best to export the different bodies of the components separately or to union the parts to create a single body. Non-RF parts were designed using Fusion 360 with a student license. Fusion 360 was chosen because it is easily accessible as well as ample resources on modelling exist online. Brackets were designed to hold the horn antenna and array to the measurement platform, plating containers, brackets and clips were used to position wire anodes inside the waveguide.

To prepare the files for printing, they need to pass through slicing software which creates a set of layers of the part at different heights of the print. The printer then realises these layers in the resin, making up the whole part. The software used for this is PreForm which Formlabs provides for the Form3 printer. Part placement, orientation and supports can be controlled in the slicer. The slicer can also scale parts and place multiple parts on the build platform. The slicer software evaluates the feasibility of the print, checking that the printer can print the parts. The slicer shows areas that may need more support. The slicer also detects cupping when a vacuum is created during prints leading to deformation. If there are errors in the STL file, a warning will appear with the option to repair the file. A visual inspection of the part is necessary if this is used, particularly in areas with small geometry. The repair can cause a webbing effect in some areas.

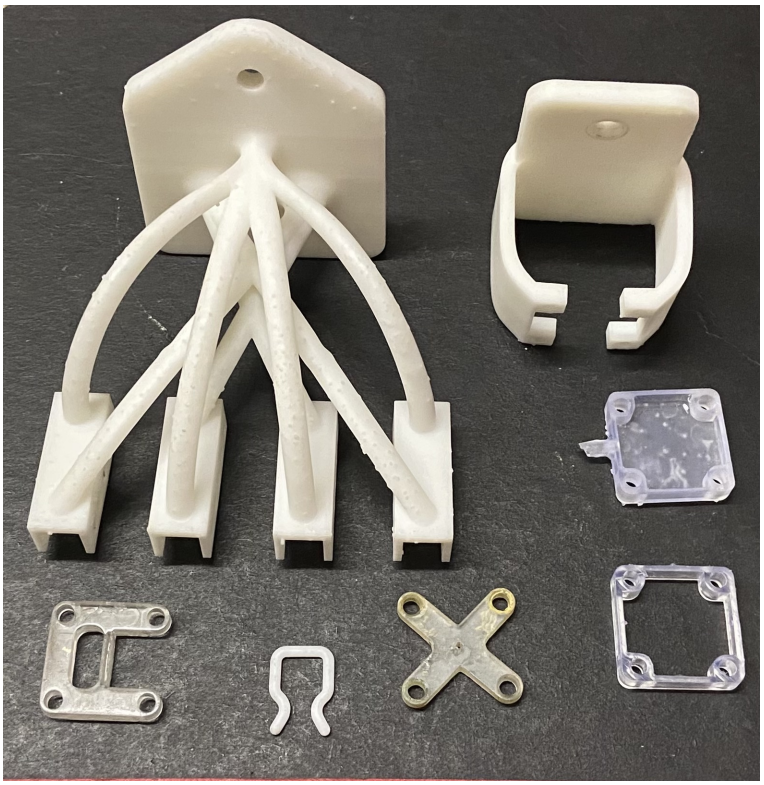

Figure 3.6. Brackets and clips that were used for measurements and manufacturing.

3.4.3 Printing orientation

A difficulty with printing waveguides is minimising the need for support inside the parts. If supports are needed inside the part, the surface finish will be rough because the breaking points of the supports leave slight protrusions on the plastic. Minimising the need for supports can be achieved by carefully orientating the part so that large surfaces of the part are not parallel to the printing platform, which allows surfaces to be made incrementally instead of the whole surface being made at once. The parts were printed 45° to the printing platform as seen in Figure 3.7.

3.4.4 Part curing and cleaning

After printing, parts need to be cured of any excess liquid resin on the parts as it comes out of the printer. The parts are placed in a washing machine which rinses the parts in isopropanol. The parts are washed for 10 minutes, after which the support structures are removed. Extra care was taken to ensure that plastic offcuts from the supports were cleared from inside the waveguide. This was done by washing the inside of the waveguide with clean isopropanol. If this is not done and there are plastic pieces, those pieces will fuse with the waveguide during curing. After the parts are rinsed in isopropanol, they are cured in a UV curing chamber. The manufacturer recommends that the parts are cured for 60

Figure 3.7. Parts printed at a 45° angle using clear resin.

minutes at 60°; however, a longer curing time was needed. The inside of the waveguides was still tacky. This is due to less UV light inside the waveguide. This was fixed by curing the parts overnight for 10 hours. Before the parts are silver plated, they need to be cleaned again to remove residue and oils from the parts. This is achieved by washing the parts in acetone, methanol and isopropanol while inside an ultrasonic cleaner. Parts were placed in plastic bags filled with acetone which were then placed inside the water bath inside the ultrasonic cleaner for 15 minutes. This was then repeated for methanol and isopropanol. Doing this was quicker and inexpensive since the cleaner did not need to be filled and emptied with the cleaning solution. During this step, gloves were worn so that oils were kept off the parts. It is crucial to minimise touching electrically significant areas. For the waveguide, these areas were the flange faces and inside the waveguide.

3.4.5 Silver plating

The chemicals used for silver plating are listed below.

- 0.5 g Silver Nitrate ($AgNO_3$)
- 0.35 g Sodium Hydroxide (NaOH)
- +/- 2 ml Ammonium Hydroxide (NH_4OH)
- 0.4 g Dextrose ($C_6\ H_{12}\ O_6$)
- 60 ml Distilled water

The silver nitrate and dextrose were purchased as a powder. The sodium hydroxide came in the form of pellets. The silver plating process was widely used and is covered in Chapter 4.

3.5 METROLOGY

The array and horn performance were measured in an anechoic chamber. The measurement frequency spanned 18 to 27 GHz, with 500 MHz increments. The DUT was measured in the far-field while rotating it along the azimuth direction until there was a full 360° measurement while the elevation was set to zero. The DUT and measurement antenna are then rotated by 90°, and the process is repeated to perform an elevation measurement. The antenna pattern was measured with 2° increments. Power dividers and time delays were measured using an Anristu MS4647A VNA. This VNA operates from 70 kHz to 70 GHz. The analyser has two ports. A short-short-short-load-through (SSLT) method and a VT220VNAWKK calibration kit for rectangular K-band waveguides were used for calibration. A sliding load was used instead of the broadband load supplied with the kit for more accurate calibration. The power dividers were measured with multiple measurements because a two-port VNA was available. The first measurement was performed between ports one and two, then between one and three, while the unused port was terminated with a matched load. They were measured in the same frequency range of 18-27 GHz, with a frequency resolution of 18 MHz.

3.6 CHAPTER SUMMARY

This chapter summarised the methods used in this study. The theoretical analysis of the array was presented, which established the relationships for the required time delays. These relationships can then be used as design goals in the synthesis of the time delay and power dividers. The design goals show that each feed branch of the array required a unique design, which is in contrast to corporate arrays which use components with equal responses. Each part is designed in CST Microwave Studio and tuned until the design goals are reached. This process used hand tuning as well optimisers that reduced the goal function set for each part.

Finding the correct recipe for silver plating was also shown to be an iterative process that was optimised for best performance. The preparation of the parts for printing and plating were critical factors that impacted the success of part manufacturing. Part orientation needed to be carefully chosen to minimise supports on critical areas, and parts needed to be thoroughly cleaned so that the silver plating could adhere to the printed parts. The array and horns were measured in an anechoic chamber and time delays and power dividers were measured with a VNA to verify their performance.

CHAPTER 4 ADDITIVE MANUFACTURING

4.1 HOW SLA PRINTING WORKS

Stereolithographic printing uses UV light to cure resin used to make up printed parts. The printer used in this work uses a UV laser to selectively cure resin layer by layer, leading to the additive nature of the manufacturing process. With SLA printing, parts are manufactured upside down, suspended on the build platform, and above the resin tank. This is done so that resin does not run off the build platform. The bottom of the tank is made of a transparent film which allows UV light to pass through to cure the resin. The process works by lowering the build platform into the resin tank until it almost touches the transparent film, usually 50 microns of separation. UV light is transmitted through a pattern that forms a layer of the part. This is then repeated but with the previous layer that was cured being placed so that it almost touches the film of the tank, where the UV light adds cured resin to the previous layer. This is repeated until the whole part is made. For the printing to work, the part must remain fixed to the build platform, which is usually achieved by using supports added by printing software. The supports are removed manually when the part is removed from the printer. The supports must hold the parts firmly in place; otherwise, distortion can occur if the parts shift, leading to the cured layers adding incorrectly to the part.

4.2 PRINTING

4.2.1 Individual part orientations used for printing

They are carefully orientated relative to the build plate to successfully print the parts. Printing at 45° prevents resin from pooling inside the part, where it might cure slightly on long prints, leading to distorted parts. The 45° also prevents the need for supports inside the parts since the surfaces are then self-supporting [65]. An example of the rounding of the corners can be seen in Figure 4.1, where the waveguide was rotated by 45° on the axis parallel to the waveguide so that it was standing on the flange corner. The bottom left corner is rounded compared to the others as resin pools in the corner

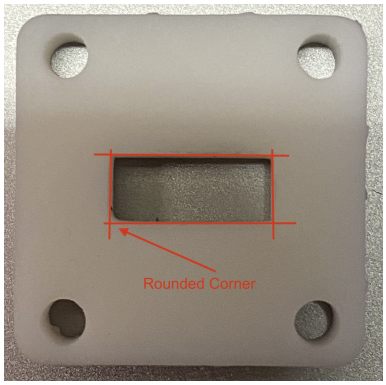

Figure 4.1. Waveguide with rounded corner due to resin pooling.

Figure 4.2. Waveguide with distorted flange due to insufficient support.

during the print. The time delays and power dividers were only rotated by 45° relative to the build platform. A difficulty with printing a standard waveguide and its flanges is that when printing at a 45°, the flange edge begins as an independent body that eventually becomes part of the waveguide as the printer progresses through each layer. If the part is not well supported, the part of the flange that is separate from the waveguide can shift, leading to distorted features. To mitigate this issue, extra support was placed along the edges of the flange to improve the connection to the waveguide body, which improved the repeatability of prints. The extra support is an alternate solution to adding webbing between the waveguide body and the flange [65]. Care was taken so that none of the supports touched the face of the flange and inside the waveguide. Supports were placed to touch the edges of the flange or the outside of the waveguide. An example of these supports is shown in Figure 4.3 cells E8, F9 and G8 as well as I9 and J9. Orientation does depend on the parts themselves and it is not

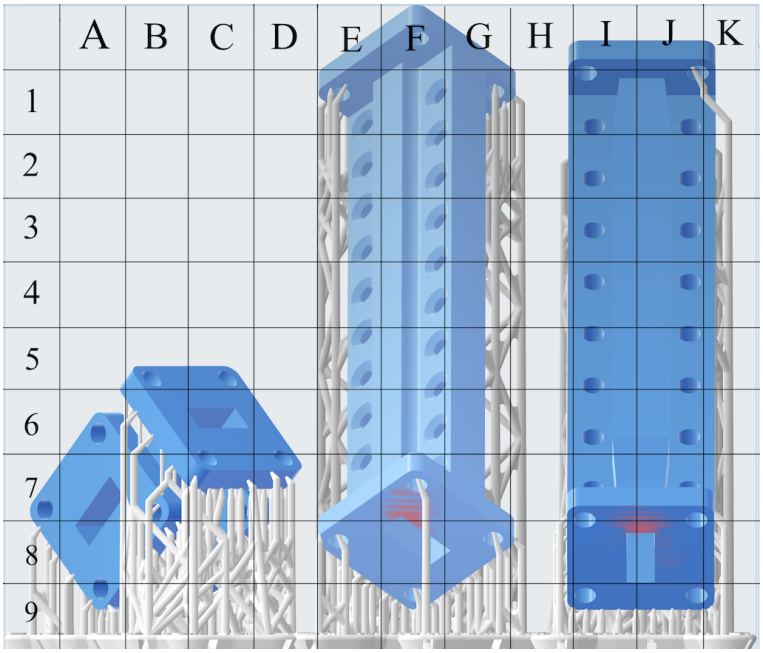

Figure 4.3. A power-divider, time delay and straight section orientated for printing in PreForm. Red shading indicates areas that are prone to fail.

always possible to prevent pooling or supports that touch the flange faces. The primary goal in all cases was to minimise internal support. Secondary to that was negating or reducing supports touching flange faces, and lastly, pooling is prevented. The power dividers were orientated at 45° but with the flange facing away from the build plate. This orientation prevented pooling around the septum of the divider but did cause rounding in some corners. In practice, this was not an issue with the power divider because the perpendicular port (Figure 4.3 cell C6) allows the resin to drain away during printing. The orientation of the parts before printing is shown in Figure 4.3.

The straight sections were the easiest parts to orientate. The long length required that the parts were rotated by 45° first in the direction the wave travels then again so that the angle between the waveguide and the build platform is 45° (Figure 4.3 centre part). This orientation provides the best chance of printing success since no face is parallel to the printing platform, potentially creating a hanging edge/surface. The time delays were the most tricky and most prone to printing errors.

The time delays could only be rotated by 45° relative to the printing platform (Figure 4.3 right). Otherwise, they are prone to resin pooling in the ridges of the waveguide, which is made worse if the sinusoid ridges are parallel to the printing platform. As a compromise, the side wall of

the waveguide was placed on the side of the build platform, but with the part rotated by 45°. A short hanging edge created a warning in the slicing software, however, the printer could still print the part successfully while allowing the resin to drain out of the part during printing.

4.2.2 Printing distortion compensation

The waveguide parts were not compensated through pre-distortion as is done in [66]. Careful orientation of the print geometry and ample support prevented serious deformation. One aspect that was corrected experimentally was the size of the screw holes used to connect the waveguide parts. Initially it was found that the screws did not fit into the holes that were printed. When the dimensions of these screw holes were measured, they were found to be on average 0.2 mm smaller than on CAD designs. The holes were made 0.2 mm bigger, allowing for the thread of the screws to self-tap into the plastic and create their own threads but without cracking the plastic.

4.3 COMMERCIAL PLATING SOLUTIONS

4.3.1 Conventional plating using C_r^{6+}

After the waveguide parts have been cured, they needed to be given a conductive finish. This is done using a metal plating process. Initially, a process used in local automotive manufacturing was attempted through a company called Plastiplate, discussed in Chapter 2.7. The parts are then dipped in a catalytic metal for nickel plating, after which it is copper plated. This process is heavily dependent on the presence of butadiene in the plastic. The SLA resin does not contain butadiene, meaning it could not be used. Furthermore, the SLA resin appeared to absorb the chromic acid (shown in Figure 4.4), which meant that an attempt to plate the part could not be continued due to the risk of contaminating the chemicals following in the process, which would be costly to replace.

4.3.2 Conductive resin solution

Another commercial solution that was attempted is a conductive resin and silver. The resin comes as two parts, namely a base SLA resin and silver ink. The manufacturer suggested that once the parts have been printed, they should be placed in an oven for sintering at 130 °C. After sintering, the parts are dipped in a mixture of silver paste and a conductive thinner. The initial ratio suggested by the manufacturer was 50:50 by weight. Parts are left in the silver paste for a minute. After this step, parts are then sintered in an oven at 120 °C for 5 minutes. A Creality LD002h 3D printer was used for the conductive resin for the resin was incompatible with the Formlabs printer. A simple dog bone shape was used in initial tests. The results for a ratio of 50:50 did not create parts that were conductive. These are shown in Figure 4.5. The base SLA material could easily be seen, meaning that the silver

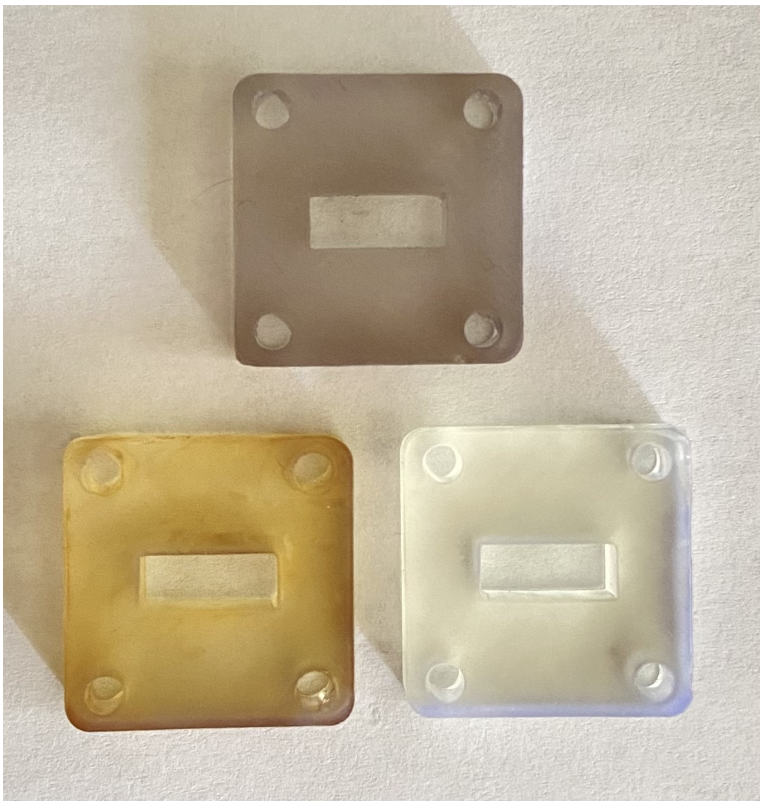

Figure 4.4. Clear resin after being dipped in chromic acid. Top: Anycubic resin part after submersion. Left: Fromlabs resin after submersion. Right: Formlabs before submersion.

concentration was too low, and not distributed evenly. The conductive paste was not very viscous, causing most of the paste to run off the part during sintering. A multimeter was used to check for conductivity on the surface part, indicating that it was not conductive. The process was repeated with a ratio that was 75 % silver by mass, which increased the viscosity. The increase in viscosity increased the amount of silver that was deposited on the part. The results are shown in Figure 4.6.

Figure 4.5. Conductive resin print with 50 % silver.

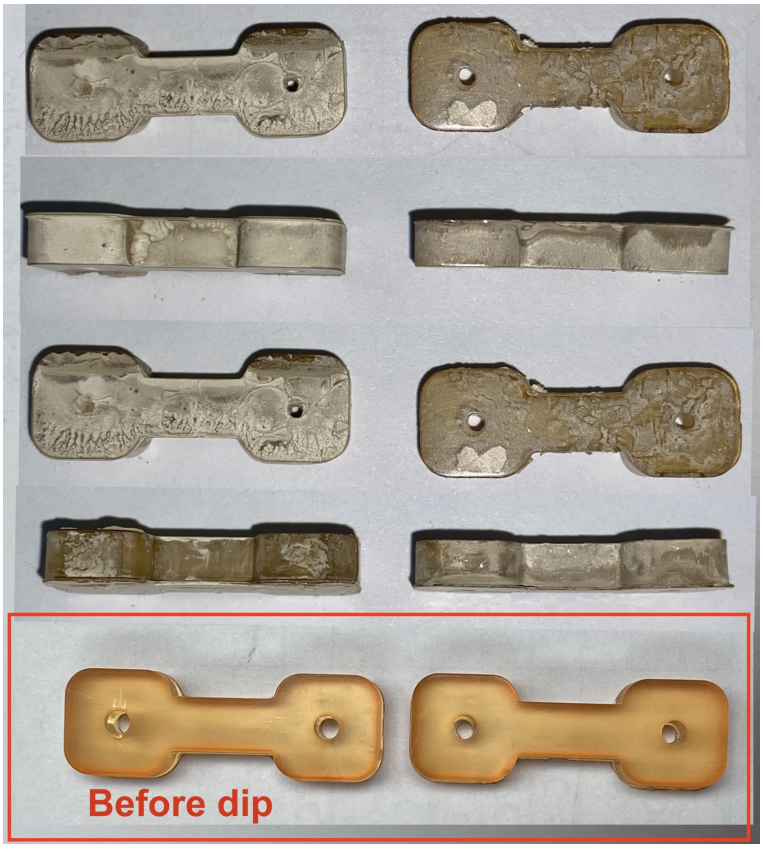

Figure 4.6. Conductive resin with 75 % silver.

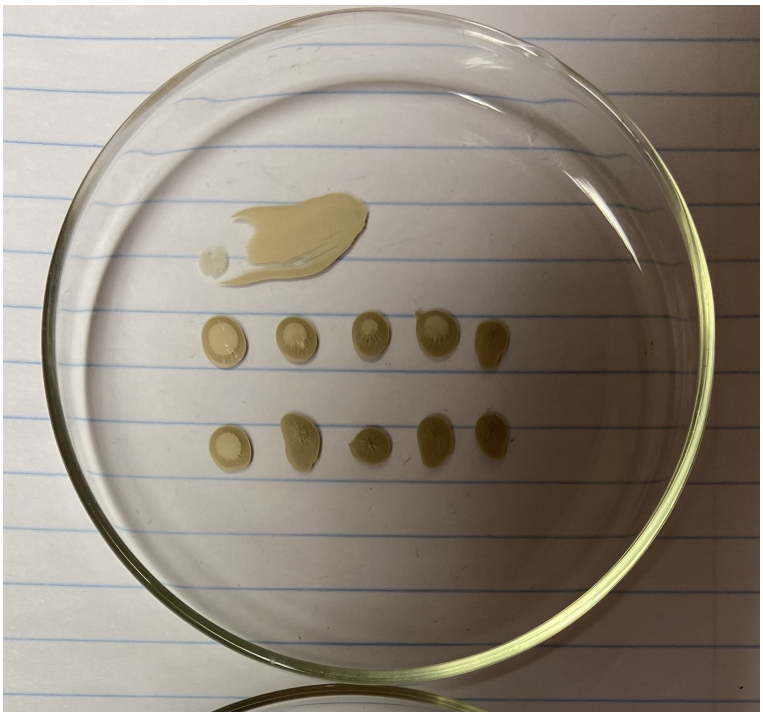

Figure 4.7. Drops mixed with resin and silver before curing.

In Figure 4.6 some of the holes are closed due to the viscosity of the silver. This would block small geometries and cause rounding of the corners of the parts, which is not ideal. A final attempt was made to see if the silver could be added directly to the resin. According to the manufacturer, it is possible but it depends on the curing power of the printer. To test this, small drops of resin with different amounts of silver were cured in the printer. The thickness and conductivity of the cured layer were then assessed for its feasibility. Silver percentages of 15, 30, 50 and 75% were tested. Silver concentrations of 15 and 30% were not conducive. The samples with 50% silver were not consistently conductive, but the lowest resistance measured was 1.2 kΩ. For a mixture containing 75% silver the printer could not cure the resin because the silver blocks the UV light from penetrating the resin. It is, therefore, unlikely that a conductive mixture would be cured by the printer and the experiment was abandoned.

4.4 TOLLENS SILVER PLATING

The waveguide parts were plated using a variation of Tollens reaction. This is a popular reaction that leaves a layer of silver on part surfaces that are in the reaction solution. The process is based on the work in [62]. The process is low cost and required 2 hours per part that was manufactured. The process requires silver nitrate, sodium hydroxide, dextrose and ammonium hydroxide. The silver nitrate, sodium hydroxide and dextrose are made into solutions using distilled water. When performing

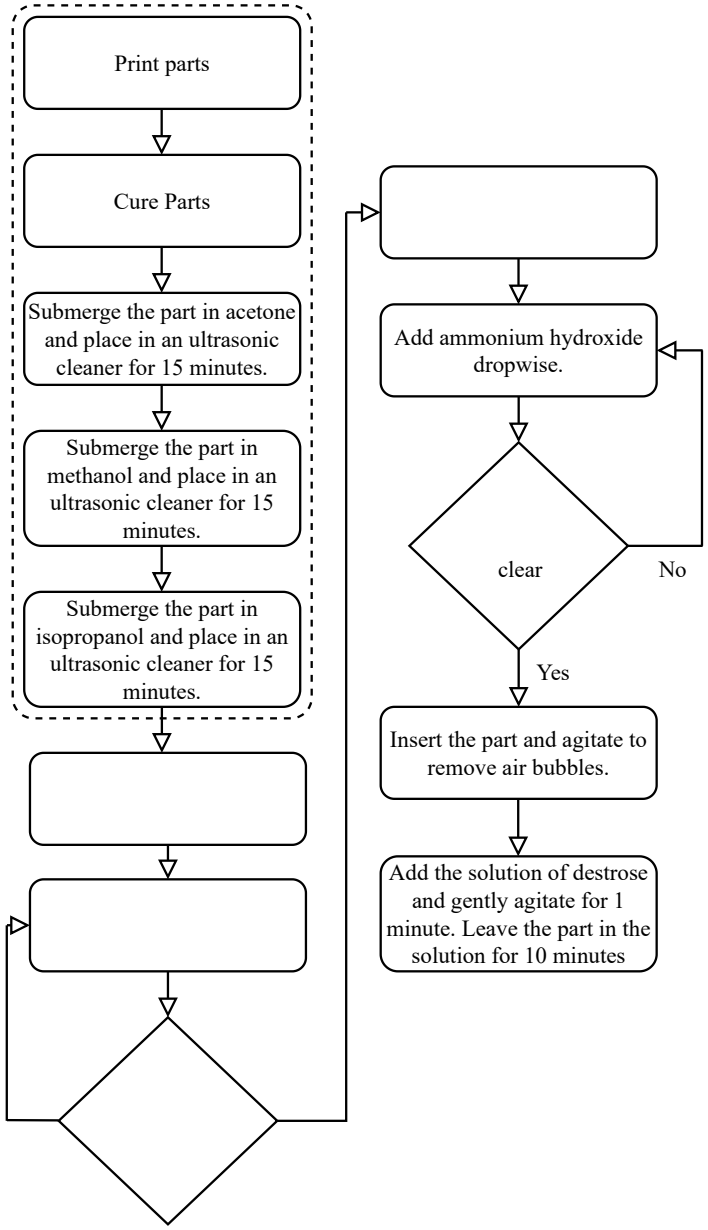

Figure 4.8. Plating process flow diagram.

a plating round, 0.5 g of silver nitrate is mixed with 25 ml of water, 0.35 g of sodium hydroxide is mixed with 25 ml of water, and 0.4 g of dextrose is mixed with 10 ml of water. The plating process is shown in Figure 4.8. Before the plating can begin, the parts must be thoroughly cleaned in multiple steps using acetone, methanol and isopropanol in an ultrasonic cleaner. Parts are dried after each step using an oven set to 50°C. It is important to wear gloves once cleaning has begun so that oils do not settle on the parts from handling. Once the part has been cleaned, the plating process can begin. The silver nitrate solution was added to a large container to hold the part. First, the silver nitrate solution

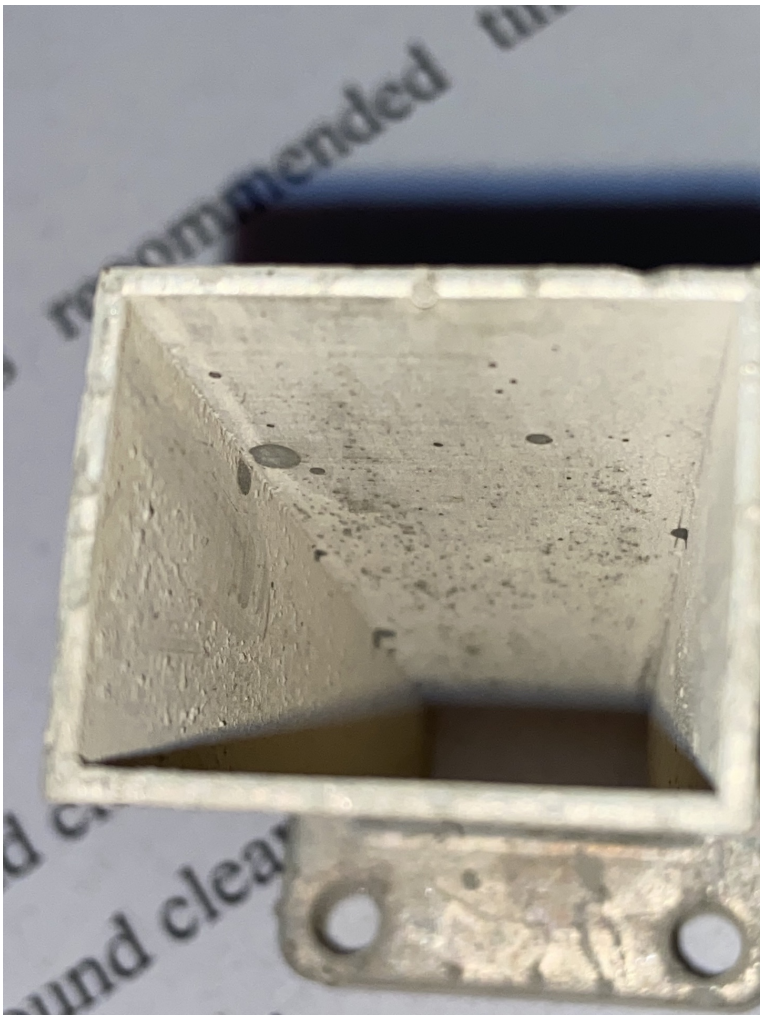

Figure 4.9. Close-up view after silver plating a horn antenna. Spots can be seen where bubbles were not fully removed.

was added to the container. Ammonium hydroxide was added dropwise, causing the solution to change to brown. Ammonium hydroxide was added until the solution became clear while being mixed gently. After the solution turned clear, the solution of sodium hydroxide was added. The colour of the mixture immediately became brown. Ammonium hydroxide was added until the solution became clear again. The part is submerged in the solution and agitated to remove bubbles. An example of not adequately removing the bubbles is shown in Figure 4.9, where spots without silver are on the part. When plating the initial horn, it was placed horizontally, making it harder for bubbles to escape. Final designs were placed vertically in a custom container with the output facing upwards. Waveguides were also placed vertically so that bubbles could easily escape and float away from the parts. Once the bubbles were removed, the dextrose solution was added while mixing for a minute afterwards. The solution became

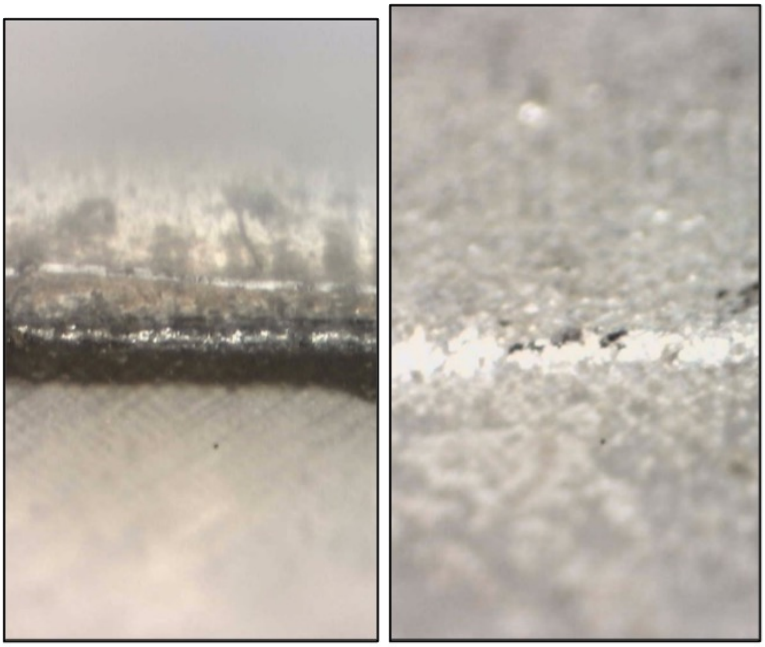

(a) Corner of waveguide printed with clear resin.

(b) Corner waveguide made with white resin.

Figure 4.10. Comparison of silver oxide build up on clear resin vs white resin.

grey and was left to stand with the part submerged for 10 minutes. After plating, the parts were rinsed in water. Parts that needed another round of silver plating were left in the water during preparation for the following round to minimise the possibility of silver oxide formation. During plating, the entire part needed to be submerged in the plating solution, which is difficult using the volumes given in [62] without increasing the amount of reagent. To solve this, a custom container was used, which minimised free space around the part, reducing the amount of reagent wasted during plating.

4.4.1 White vs clear resin

A comparison was made between FormLabs white and clear resins, with the intention of testing if there is more silver adhesion to either of the two materials. The experiment's motivation came from observing a consistent layer of silver on the glass beakers after some plating experiments. The two resins were evaluated by plating split block straight sections and measuring S-parameters between plating rounds. The performance of waveguides made with white and clear resin is summarised in Figure 4.11. When considering the S_{21}, the white resin waveguide performs much better than the clear waveguide, a consistent result. In contrast, the clear waveguide performed consistently worse, with only one instance matching the performance of the white resin. This is a reasonable result considering

the silver oxide buildup shown in Figure 4.10. Surface currents need to travel across the corners of the waveguide, which has more loss in the case of the clear parts where the corners do not have good silver plating. Unfortunately, with the silver oxide buildup limiting the performance achieved with clear parts, the benefits of the improved tolerance of the clear resin could not be tested. With four rounds of plating on white resin, the white resin waveguide performs significantly better than the clear resin waveguide. The S_{21} and the S_{11} measurements can be seen in Figures 4.11 and 4.12. The S_{11} result can be attributed to conduction losses where the flanges touch, leading to the increased reflected wave.

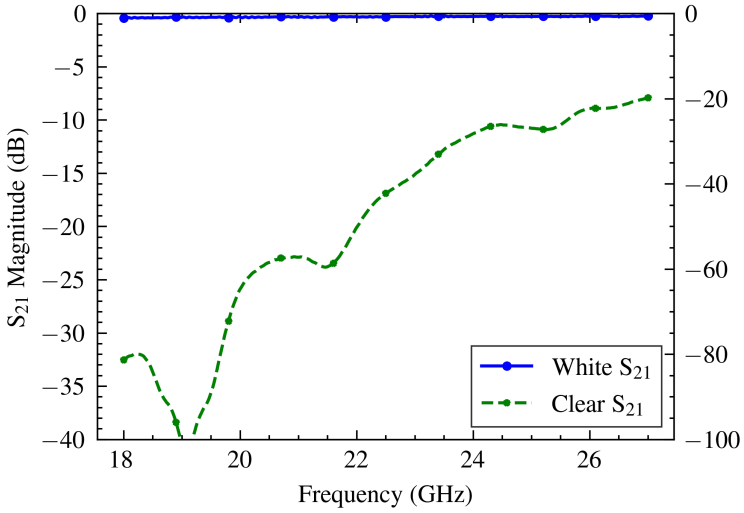

Figure 4.11. S_{21} of white and clear resin waveguide.

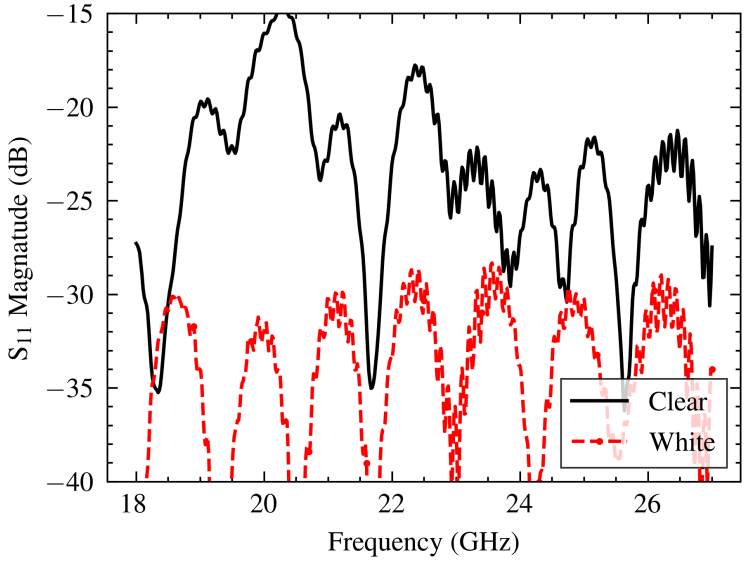

Figure 4.12. S_{21} of white and clear resin waveguide.

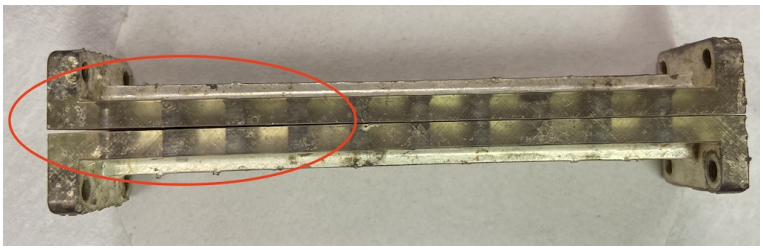

Figure 4.13. Image of a warped waveguide flange. The right-hand side of the two halves are flush while the left is not.

4.4.2 Split block vs monoblock

Initial designs were manufactured as split blocks which were bolted together. These waveguides were easier to plate since there was no tube. The halves were placed on their back with the waveguide grooves facing upwards, so bubbles were less likely to be trapped. Split block designs were most susceptible to warpage. In all cases, waveguides had curled, which meant they were not perfectly parallel. When the two halves were bolted together, they were bent toward their original shape. The curling can be seen in Figure 4.13. There was also warping at the flange, which caused the flange not to be perpendicular to the waveguide. This was difficult to repair. When connecting the flange to the VNA, the waveguide-to-SMA adapter does cause them to flatten, but not completely. This worsened S_{11} performance. The flanges on each half also did not warp equally, making the surface not coplanar. Monoblock prints did not have as many issues with warping, especially on the flanges, which printed flat. The assumption is that there is more structural integrity from the larger bending radius and symmetry. Similarly, monoblock waveguides also had good performance after four rounds of silver plating, showing little advantage with split-block designs.

4.4.3 Improving silver finish

Preventing silver oxide buildup was a minor optimisation that yielded significant improvements to the silver finish. Initially, between plating rounds, the parts were dried in an oven. During this process step, dark streaks were present on the parts, which were presumed silver oxide. To prevent the build up of silver oxide, the parts were rinsed and placed in distilled water to prevent oxygen exposure and keep the parts cool, as both air exposure and heat contributed to the formation of silver oxide. The reagents were kept cool during the reaction to improve the finish further. Parts made this way presented with a much better surface finish as shown in Figure 4.14. Cooling the reaction improved the finish by slowing the reaction, improving the surface finish. Slowing the reaction chemically [67] is within the scope of future work. The waveguides that achieved the least loss were manufactured

Figure 4.14. Dried waveguide (bottom) vs immersed and cooled waveguide (top).

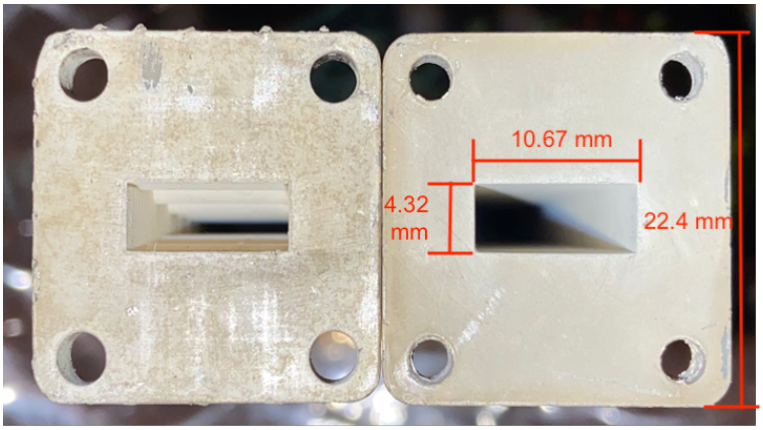

Figure 4.15. Flanges of the dried waveguide (left) vs waveguide that remained immersed (right).

using this method, improving the loss that rivalled the copper-plated waveguide. As shown in Figure 4.15, flanges had a significant visual improvement that directly affected the reflection coefficient. The plating solution's temperature was lowered by placing the reagents in a fridge set at 2° C and removed when needed. Parts manufactured this way had a more consistent finish and performance was more repeatable, as seen in Figure 4.16. The repeatability is compared to those shown in Figure 4.17, where there was more variability in performance. The best waveguide achieved a minimum attenuation of 0.39 dB, while the worst-performing one featured more than 10 dB of attenuation in places. With cooling, attenuation of 0.4 dB was easily achieved when cooling the parts. Furthermore, outlier cases like case C in Figure 4.17 did not occur.

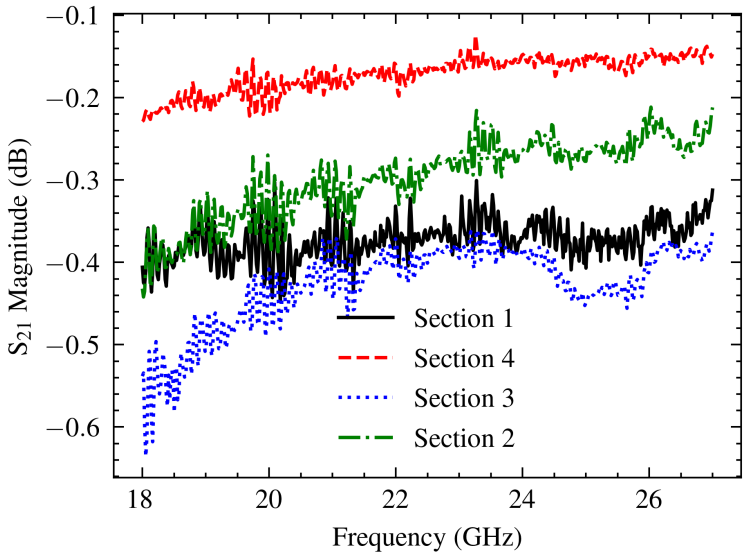

Figure 4.16. S_{21} of 100 mm long waveguide that was kept cool during manufacturing.

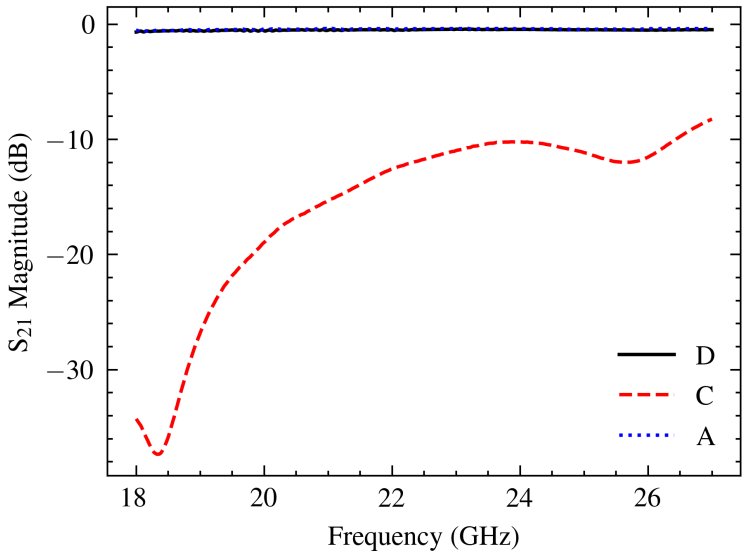

Figure 4.17. S_{21} of waveguide that was not kept cool during manufacturing.

The cooled waveguide also had a visually better surface finish, attributed to a reduced silver oxide buildup on the parts. The time it took for the reaction to complete increased since the cooler temperatures reduced the reaction rate, but the overall time was not affected since parts were not dried.

4.4.4 Silver thickness

The thickness of the silver was evaluated by plating glass microscope slides and measuring the change in height from glass to silver using a profilometer. Glass was used instead of plastic because the roughness of the plastic masked the step change. In Table 4.1, the thickness of the silver is shown for up to five silver plating rounds. The layer needs to be thick enough to support the surface currents with minimal loss. According to [14], multiple skin depths are needed for low loss. The skin depth is given by (2.11).

Table 4.1. Average and minimum thickness of silver when plating glass slides.

Number of rounds	Average thickness (µm)	Minimum thickness (µm)
5	7.535	2
4	6.755	2
3	6.925	1.215
2	3	1
1	0.6	NA

The skin depth for silver is 0.4 µm at 22.5 GHz. This means that the layer of silver should be at least 1.27 µm. Based on Table 4.1, this means that at least four or more rounds of silver plating are required. One round of silver plating did not provide a uniform layer, as can be seen in Figure 4.18.

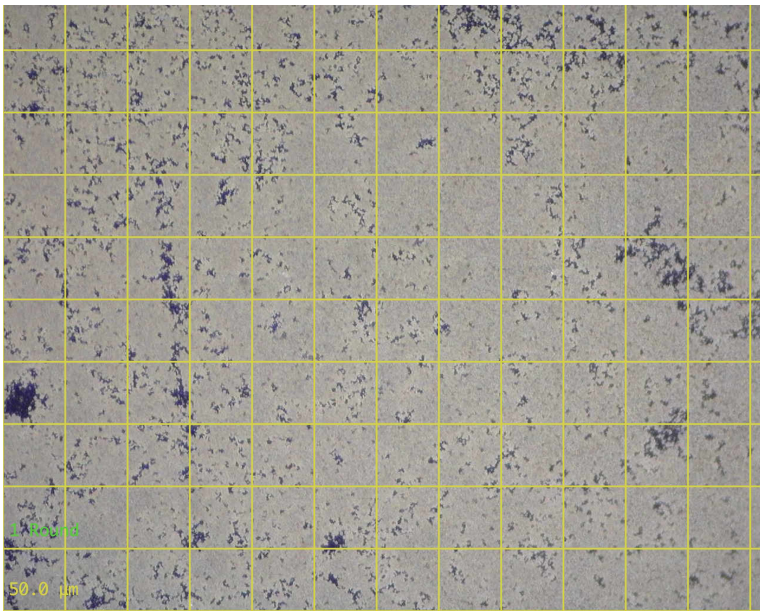

Figure 4.18. Image of the silver surface taken with a microscope after one round of plating.

This study found that multiple rounds were needed to produce a silver layer that was thick enough so that parts had low losses. With four rounds of silver, there were no holes in the surface, but it can be seen that the surface is still not perfectly smooth, as seen in Figure 4.19.

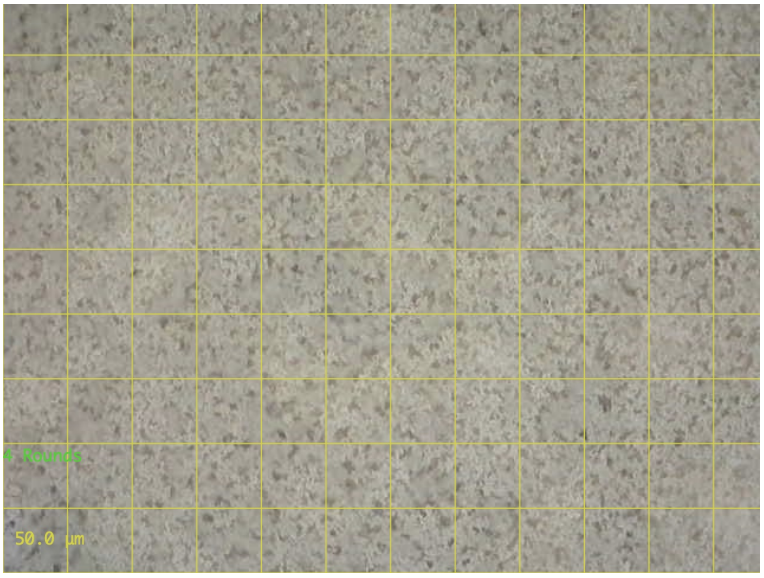

Figure 4.19. Image of the silver surface taken with a microscope after four rounds of plating.

These results were confirmed when measuring the S-parameters of a plated waveguide section with varying amounts of plating rounds. In Figures, 4.20 and 4.21, S_{21} and S_{11} results are shown.

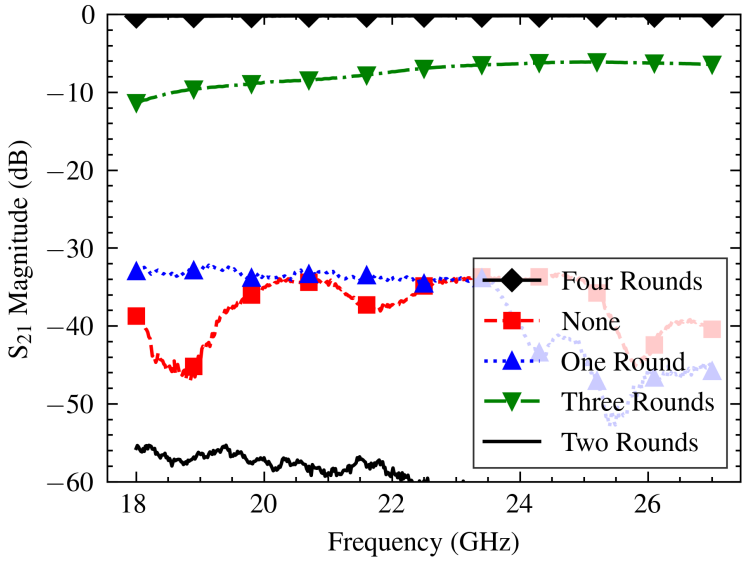

Figure 4.20. S_{21} of waveguide with extra rounds of silver plating.

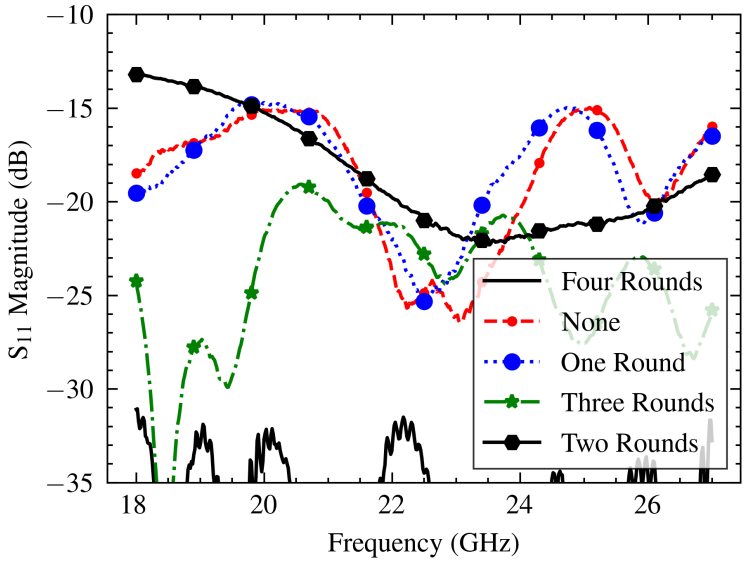

Figure 4.21. S_{11} of waveguide with extra rounds of silver plating.

An interesting observation is that there is little to no improvement with only one or two rounds of silver. In some cases, there is even a reduction in S_{21}. This is assumed to be caused by the silver layers that are too thin to conduct the surface current without introducing significant losses. Two rounds

introduced much more loss than no rounds, where the two waveguide adapters radiate towards each other. The difference between two and three rounds is quite substantial as the silver layer is more consistent and becomes thick enough to support the surface current without significant losses. This view is supported by Figures 4.18 and 4.19; this assumption holds up. With four rounds, there is further improvement of the S_{21} achieving a transmission loss of 0.5 dB across the band. Figure 4.22 shows the performance with another two rounds of silver plating. After four rounds of plating, further rounds yield little benefit. Five rounds only provided an improvement of 0.05 dB, while six provided an improvement of 0.02 dB. This is explained by the fact that four plating rounds already constitute three skin depths. After seeing these results, four rounds were selected as the standard number of layers to manufacture waveguides.

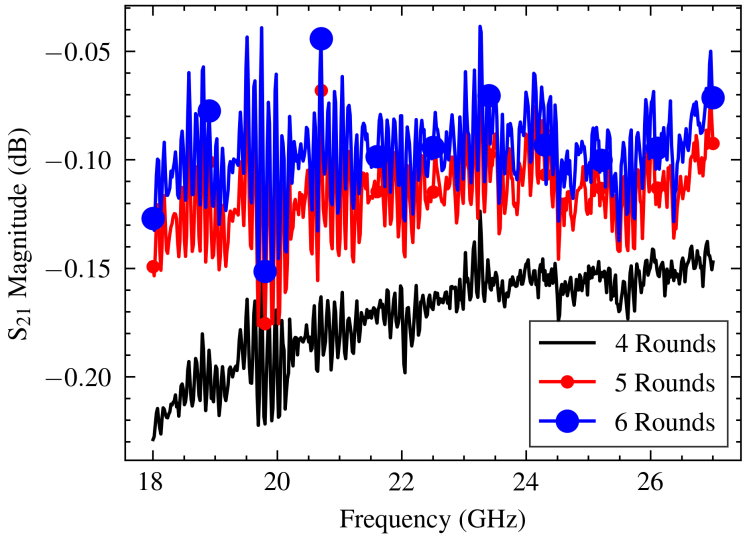

Figure 4.22. S_{21} of waveguide with another two rounds of silver plating.

The time delays had more complex geometry inside the waveguide, leading to a reduced flow of plating solution. The time delay with the greatest delay (branch one) needed eight rounds of silver plating. This is because the more complex geometry reduced the flow of the plating solution to the inside of the waveguide, resulting in branch one having eight rounds of silver plating instead of four. There was an attempt to use a pump to ensure a continuous flow of the plating solution; ensuring there is a continuous movement of the plating solution during the entire solution preparation process and when the dextrose is added.

Figure 4.23. Waveguide being plated using a pump to move the plating solution.

This process was difficult to control but gave a good finish inside the waveguide. After considering that monoblock parts could be plated easily without a pump, the method was abandoned. This method, however, does have the potential for small complex geometries.

4.4.4.1 Custom silver plating containers

To increase the success of the silver plating, custom containers were designed in Fusion 360 and printed. When plating the split-block waveguide, a horizontal container was used. The container dimensions allowed for a 3 mm clearance around the waveguide to ensure that the whole part was submerged in plating solution by minimising wasted volume in the container. When the waveguide is placed inside the container, the groove faces upwards so that air bubbles can escape instead of being stuck in the waveguide groove. A protrusion is added to take up more volume that would otherwise be free space under the waveguide. A vertical container was used for monoblock prints. The corners at the bottom of the container were rounded so that the face on the bottom flange did not contact the bottom of the container, reducing the flow of the plating solution to the flange. A hole was made in the sidewall of the container to prevent cupping during printing, which occurs when the part traps air while printing (which subjects the semi-cured parts to stresses, which can lead to deformation). The hole was filled with resin and cured with a UV light by hand after printing. The container was tall enough not to overflow when the part was placed inside with the plating solution. Fusion 360 allows for the

measurement of the volume of the container. The container volume is then added to the amount of plating solution used during plating. The height is then found using the area of the container opening. The height was rounded up to reduce spilling, and the corners were rounded to prevent flange faces from touching the container. The opening of the container allowed for a 3 mm clearance around the waveguide. This had the added benefit of weakly forcing plating solution through the waveguide when the waveguide is dropped in; forcing air bubbles out of the waveguide.

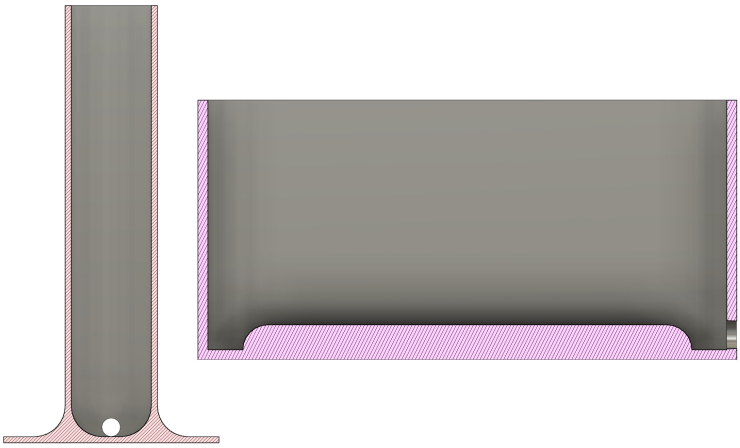

Figure 4.24. Section view of the horizontal (right) and vertical (left) containers used.

4.4.5 Copper plating

The parts were copper plated using the silver seed layer. A copper sulphate solution from Merck was mixed with water at a ratio of 50g:500ml. Waveguides that were plated were made as split block assemblies. The parts were placed in a copper sulphate bath with copper anodes surrounding the part. Care was taken to ensure anodes surrounded the parts so that there was a sufficient electric field inside the parts. The anodes are connected to the positive terminal of the power supply, and the part is connected to the negative terminal via a small copper wire, so the whole part is submerged in the plating solution. The halves were plated with 10 mA for 10 hours, creating a slow deposition of copper to help ensure a smooth finish. The plating solution was prepared with a ratio of 50g of copper sulfate with 500 ml of water.

4.4.5.1 Conductive FDM filament

Initially, a conductive FDM filament was tested. The same dog bone shape used in the conductive resin prints was used. A Creality CR10S FDM printer was used with a PLA filament infused with carbon. The intention was to copper plate parts without requiring a conductive silver layer. The FDM filament was poorly conductive, limiting the current that could be used when plating despite the applied

voltage being greater than 40 V. The poor conductivity limited the plating current leading to a slow formation of copper for a small dog bone shape. Larger shapes would not plate evenly because the poor conductivity would yield a very uneven finish. The part after copper plating is shown in Figure 4.25.

(a) Front view of the conductive FDM printing.

(b) Side view of the conductive print where more copper formed.

Figure 4.25. Copper plating of the conductive FDM printer plastic.

There was more copper formation on the side of the part because the anode was parallel to the side of the part. The part was distorted during printing but could still be used to evaluate its potential for copper plating. The parts were plated for 8 hours with the maximum plating current that could be achieved. The plastic was deemed not conductive enough for successful plating and further work with it was halted.

4.4.5.2 Horn antenna

Initially a horn antenna was plated, as seen in Figure 4.28. A copper wire anode was placed in the centre of the horn to ensure an electric field for the copper plating. A bracket was used to hold the copper wire in the centre of the horns.

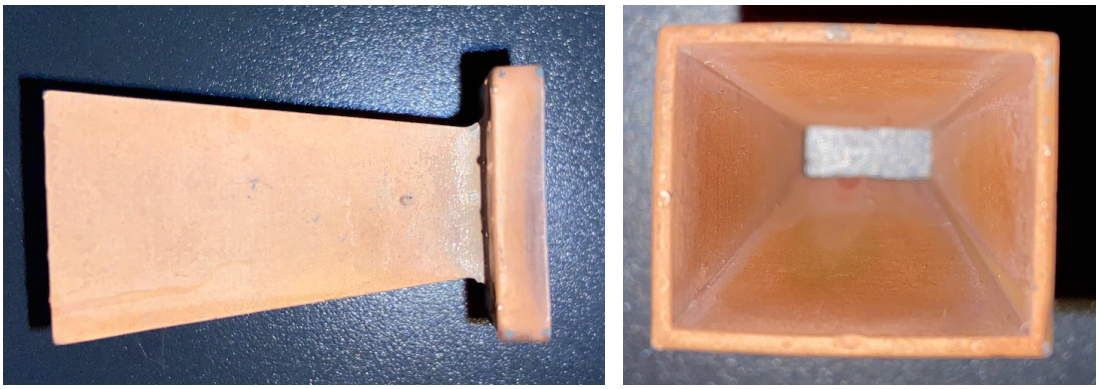

(a) Copper plated horn antenna **(b)** Inside of the copper plated horn antenna.

Figure 4.26. Horn antennas that were copper plated using the silver layer as a seed layer for copper plating.

There was good coverage of copper on all sides of the horns. The conductive seed layer used for copper plating was created using four rounds of Tollens silver plating. The copper sulphate solution had the same ratio as that used for the conductive FDM prints; a current of 50 mA was used while the applied voltage was 2.4 V. While there was good coverage, the finish was matt and the surface was visibly rough.

4.4.5.3 Copper-plated waveguide

A 100 mm copper-plated waveguide is shown in Figure 4.27. The waveguide was copper plated using four rounds of Tollens silver layer as the seed layer.

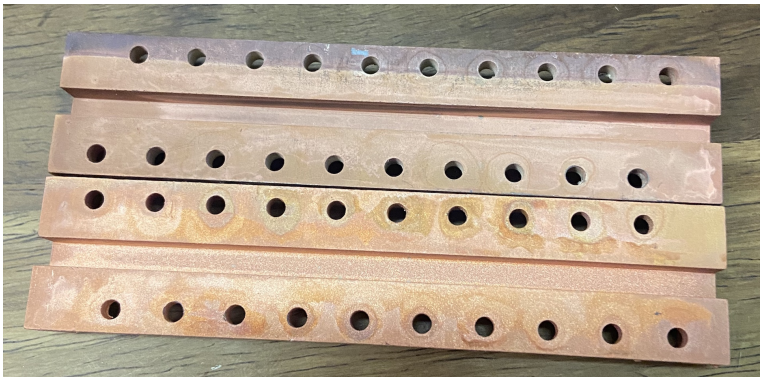

Figure 4.27. Waveguide after copper plating.

The waveguides were plated using a current of 100 mA over 10 hours. The slow rate was used to reduce the surface roughness. The waveguide was completely covered in copper, including the groove where the surface currents are located. In Figure 4.28, the waveguide at different plating stages can be seen. The silver finish was smoother than after copper plating was applied, which is noticeable in how shiny the surfaces are.

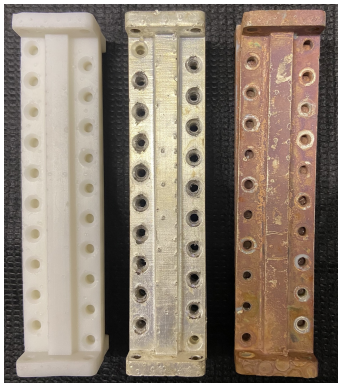

(a) Waveguide during different stages of manufacturing.

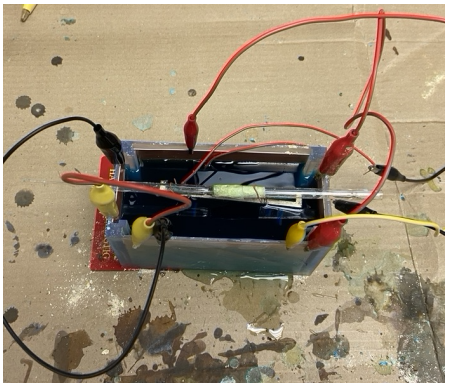

(b) Waveguide during plating.

Figure 4.28. (a) A comparison of the waveguide in all manufacturing stages. The part on the left is after printing. The centre waveguide has been silver plated, and the right waveguide has been copper plated. (b) During copper plating the parts were suspended in the plating solution.

Anodes were added on all sides of the container to ensure good electric field coverage. The anodes were copper sheets that slid into the custom copper plating container grooves. The anodes were then connected to the positive terminal of the power supply. The performance of the waveguide shown in Figure 4.27 was measured on a VNA to characterise the loss and is compared to an off-the-shelf waveguide manufactured using brass in Figure 4.29. The off-the-shelf waveguide featured an insertion loss below 0.1 dB across the full waveguide band, while the copper-plated waveguide achieved a -0.55 dB insertion loss. The off-the-shelf waveguide had a lower reflection coefficient of -38 dB versus -23 dB for the copper-plated waveguide (Figure 4.30). Considering the performance achieved, the waveguide lost less than -5.5 dB per meter. Despite the successful copper plating of the waveguide, the results were not repeatable. Following attempts resulted in corroded waveguides (Figure 4.31) inside the plating solution. The corroded waveguide did not perform as well as the first copper plating attempt or as well as parts with only silver plating. Compared to waveguides with only four rounds of silver, the silver-only waveguide showed a similar performance to the copper-plated waveguide and

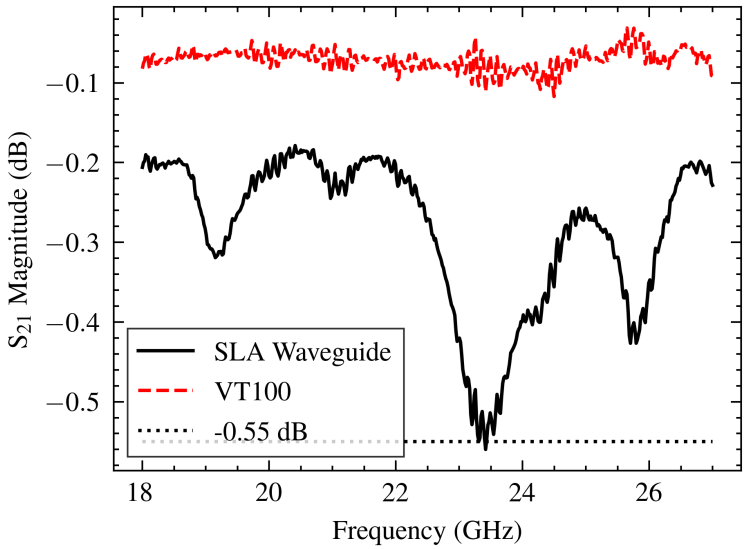

Figure 4.29. S_{21} measurement of the copper plated waveguide.

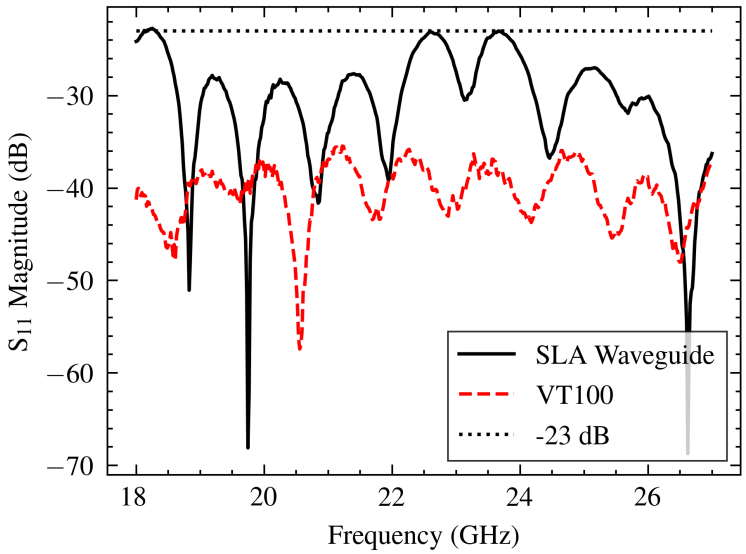

Figure 4.30. Reflection coefficient of the copper plated waveguide.

Figure 4.31. Corroded copper waveguide.

exceeded it in some cases. It was decided that copper plating would not improve part performance because of the good performance offered by parts with only silver plating.

4.4.6 Metal printed parts

A metal waveguide was printed to compare to the SLA waveguides. The waveguide was printed with titanium Ti64 powder on an EOS metal printer by the Center for Rapid Prototyping and Manufacturing (CRPM). The metal waveguide is shown in Figure 4.32.

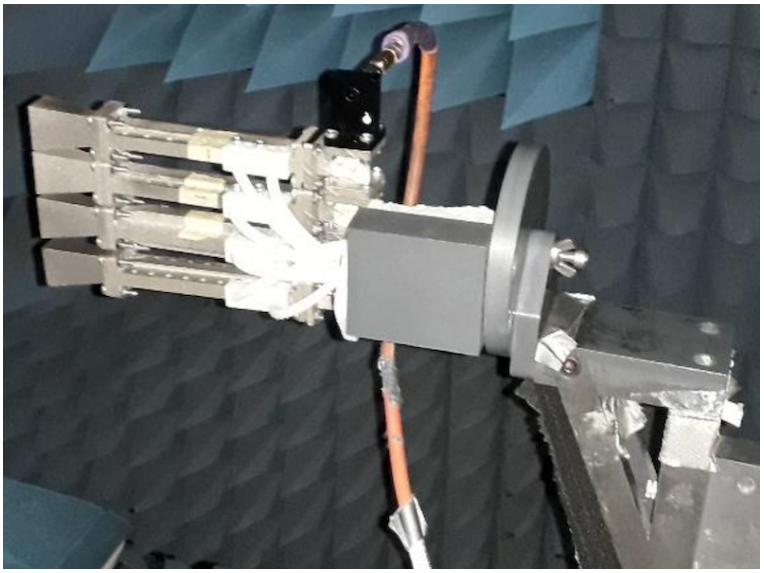

Figure 4.32. Metal antenna array during measurement.

The metal printed parts were very distorted. The end horn antenna was skewed off the broadside. The metal parts also had more loss when compared to sliver-plated SLA parts. The flanges were rough from support material, and the laser used to melt the metal particles necessitated skimming after printing. The surface of the metal printed waveguides are shown in Figure 4.33

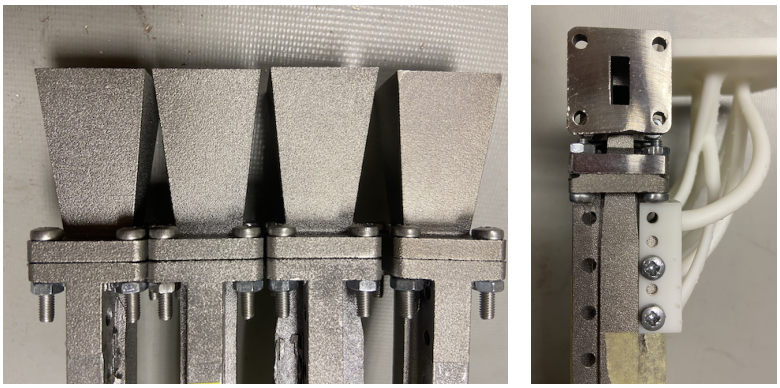

(a) **(b)**

Figure 4.33. Distorted parts of the metal printed waveguide array. (a) Horns of the antenna array. (b) Input flange of the metal array.

In Figure 4.34, the SLM parts are shown as they came out of the printer. The roughness can be seen all over the part. This roughness degrades the performance in two ways. The first is that a rough surface introduces increased losses, since the wave travels on the surface and has an imperfect path. The second is that the roughness can reduce the electrical conductivity between waveguide flanges leading to loss. The SLM printed waveguide had to be post-processed on a lathe to improve the flange surface finish. Internal post-processing was impossible since the cutting tool could not access the inside of the waveguide. There is a significant difference in flange surface roughness when comparing 4.33 and 4.34. The performance of the SLM waveguide is compared to the off-the-shelf waveguide and the white resin printed waveguide in Figures 4.35 and 4.36. In Figure 4.35, the off-the-shelf waveguide and the white resin printed waveguide exceed the metal-printed waveguide in terms of insertion loss.

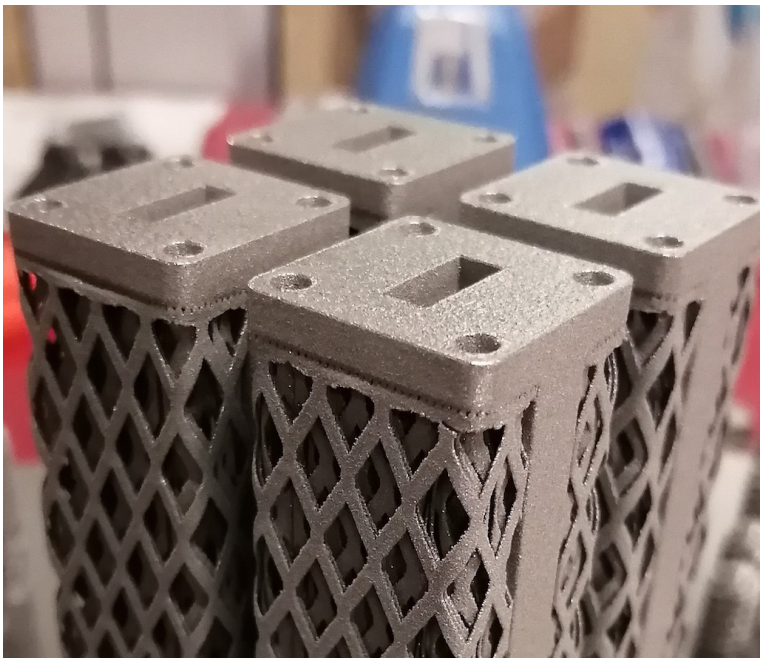

Figure 4.34. Metal printed parts when removed from the printer.

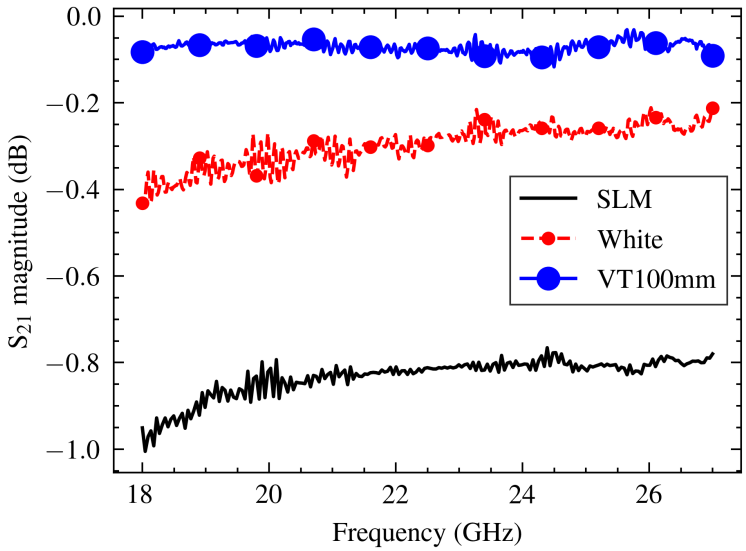

Figure 4.35. S_{21} of a metal printed waveguide, a waveguide made from white resin and four rounds of silver plating, and an off-the-shelf waveguide (VT100mm).

Considering that the SLM parts have the worst transmission loss, it is interesting to note that they have an S_{11} comparable to the off-the-shelf waveguide. This confirms that the loss is due to surface roughness inside the waveguide. This also hints at the possibility that the flanges of the resin-printed

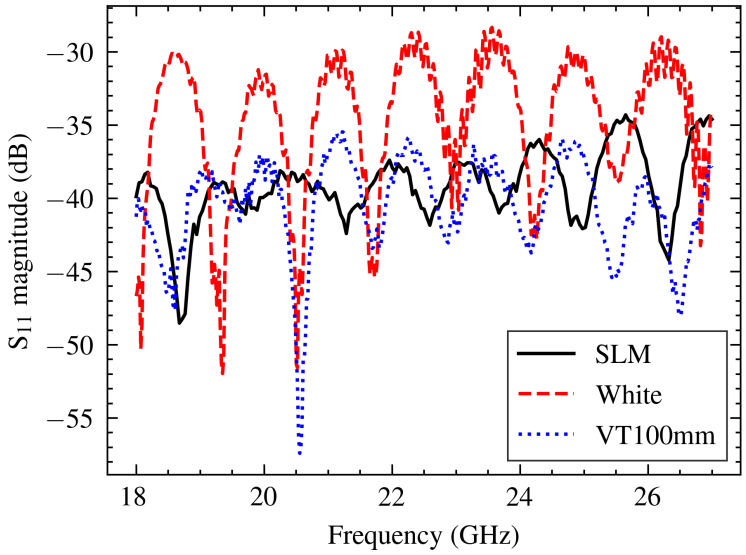

Figure 4.36. S_{11} of a metal printed waveguide, a waveguide made from white resin and four rounds of silver plating, and an off-the-shelf waveguide (VT100mm).

waveguides are either slightly deformed or don't provide a good electrical connection. It should be noted that calibration allowed for S_{11} measurements down to -50 dB.

4.5 CHAPTER CONCLUSION

Considering the measured results, it is evident that a WR42 waveguide was successfully manufactured by printing the part with white resin, cooling the Tollens reaction to 2 °C, and using a minimum of four plating rounds. This simplified manufacturing significantly, given the complexity associated with copper plating the waveguide. It also has the added advantage that parts can be used immediately without requiring assembly. Electroplating components operating at lower frequencies should pose fewer difficulties because the larger dimensions allow for more flexibility when adding anodes inside the waveguide. An observation made during silver plating is that a few rounds are needed to create a good layer of silver on the glass. A further observation is that glass beakers used in some experiments had an opaque layer of silver after the first rounds of plating, while the printed parts needed three rounds before the base resin could not be seen. This leaves room for more work to be done experimenting with different resin types, hoping that a resin with a high affinity for silver can be found, reducing the number of plating rounds and the cost of raw materials. The issues in repeatability of copper plating the waveguide meant that silver-plated waveguides were the only option, with the white resin performing better than the clear resin. Finally, as the single successful copper-plated waveguide performed similarly to copper-plated waveguides, there was no reason to use copper plating. There is potential

that waveguides manufactured as monoblock parts and then copper plated by careful placement of anodes inside the waveguide will perform better than the white resin silver plated waveguide. This expectation is based on the work done in [32], which investigates the effects of cutting planes.

CHAPTER 5 ARRAY REALISATION

5.1 CHAPTER OVERVIEW

This chapter describes the realisation of the array and refers back to the theoretical design in Section 3.2. The design of the sinusoidal delay lines, asymmetric power dividers and the horn antenna is covered in this chapter. At the end of the chapter, the performance of the waveguide components and the array are presented.

5.2 HIGH LEVEL DESIGN

Typically the spacing between antenna elements in a broadside configuration is set to just less than one wavelength to ensure maximum directivity. At 22.5 GHz, a spacing of one wavelength would imply the outputs are spaced less than 13.3 mm away from each other. A K-band rectangular waveguide has a width of 10.688 mm, meaning that the waveguide wall would need to be less than 0.6 mm. There would also be no space for horn antennas placed on the output to flare outwards. To solve this issue, the spacing between antenna elements was chosen to be 22.5 mm or 1.7 λ_0. The maximum directivity based on element spacing is shown in Figure 5.1, taken from [1]. A spacing of 22.5 mm is equal to 1.7 λ_0. This spacing is near the second peak in directivity that occurs at 1.9 λ_0. The disadvantage of increasing the element spacing is that the time delay needed is increased, as shown in (3.4) and (3.5). Increasing the spacing also has the disadvantage of introducing two grating lobes in the array pattern. These lobes have a directivity that is equal to the main lobe. Using the free space propagation velocity, the relations for time delays in (3.3), (3.4), (3.5) and assuming a right angle corner waveguide is used approximated as $d + l$, the time delays are calculated and shown in Table 5.1. If the time delays are perpendicular to the feed line, t_{end} is equal to t_{ie} plus the time taken to travel along the straight section connected to the last output port. A physical delay length of 100 mm was chosen as it provides enough physical space for the time delays to be synthesised without much difficulty. Before committing to physical dimensions for the array, the system concept was first simulated using high-level simulation

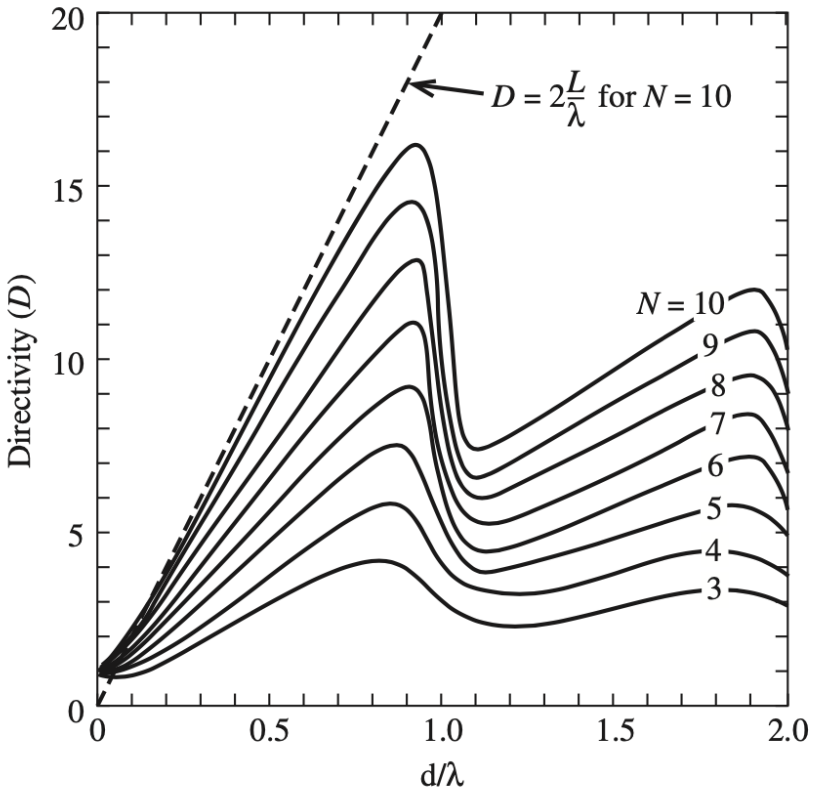

Figure 5.1. Antenna directivity as a function of element spacing. Taken from [1]. ©2012 John Wiley & Sons.

Table 5.1. Theoretical delays needed for a broadside beam.

Branch	Delay (μs)
t_{d1}	0.559
t_{d2}	0.484
t_{d3}	0.408

with ideal elements shown in Figure 5.2. This was verified by checking for equal phases at all outputs of the antenna array. Standard waveguide is modelled using ideal transmission line elements. The time delay line was modelled using ideal time delays. Tuning the time delays in sequence is a simple process. The delay is adjusted until the phase at the antenna is equal to the phase at the end antenna. If the gradient of the phase is steeper than the last antenna, the time delay is too large and vice versa. The phase at the output port is only affected by the time delay connected to that port and the feedline. Thus, each time delay can be found without concern for the delay at other delays. This makes the process simple and can be easily found manually with tuning or using computer optimisation.

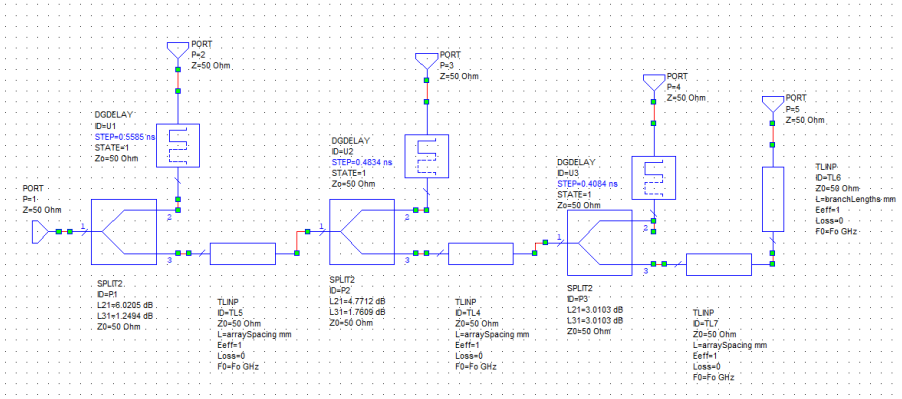

Figure 5.2. AWR schematic of the high-level simulation.

The array designed here was a uniformly excited array. A non-uniform array with unequal element spacing can also be designed with this approach by using the time delays to control the phase and the power dividers to control the amount of power to each horn. This could potentially improve the side lobe level of the array. Since the array was designed to demonstrate the additively manufactured series feed network, there were no specific design goals for the array performance. The maximum gain was chosen, which necessitated a uniformly excited array.

The high-level simulation was conducted using Cadence VSS. The simulation used ideal power dividers, transmission lines and time delays. The noteworthy results are the phase relationships between the output ports and the input port, and the power at the output ports. The relative phase and power at the outputs must be equal over their band of interest for a broadside directed beam, which satisfies the case for an array that is firing broadside. These are shown in Figures 5.3 and 5.4.

5.2.1 Cadence VSS design

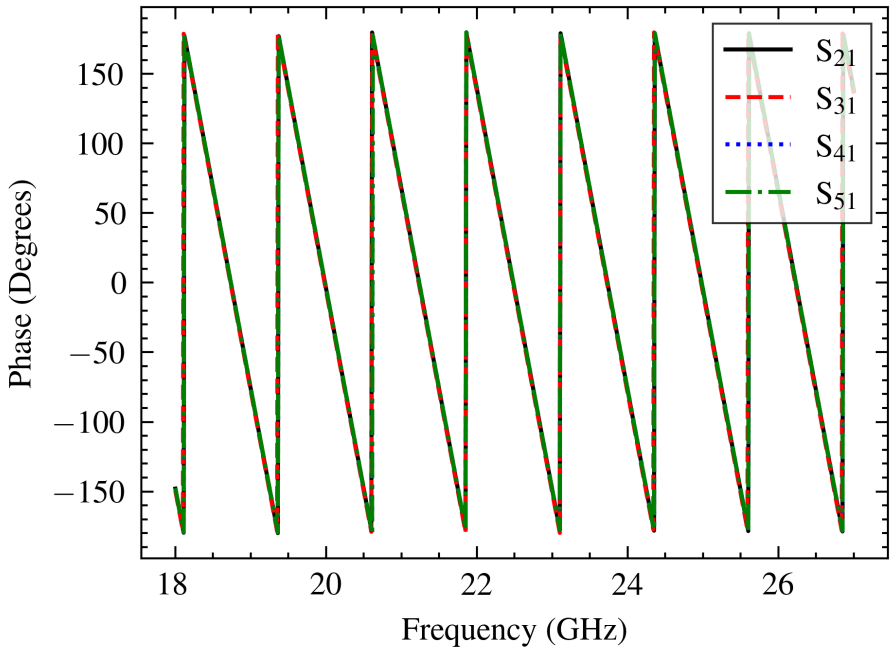

Figure 5.3. Theoretical phases at the array's output for a broadside beam.

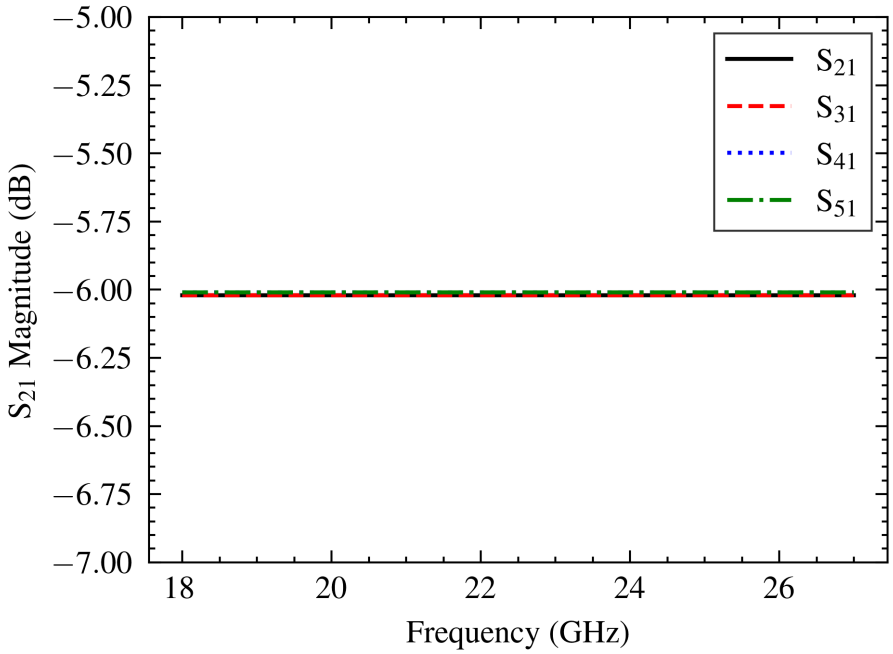

Figure 5.4. Theoretical powers at the array's output for a broadside beam.

The achieved phase result shows that the time delay causes the phases of the output ports to be equal over the entire K-band. The power at the output ports is also equal throughout the K-band. Both results show that the solution is viable and that a detailed design could begin. The array factor that should be obtained with the magnitude and phase results of Figures 5.3 and 5.4 was calculated and is shown in Figure 5.5, which indicates the two grating lobes around the main lobe. The array pattern accounts for both the power and time delays described in the rest of this chapter. The main lobe of the array pattern has an array factor of 5.933 dB, while the left and right grating lobes have a array factor of 5.94 dB each at a 50° offset from the main lobe. With the additional boresight gain of horn antennas, the grating lobes will be reduced.

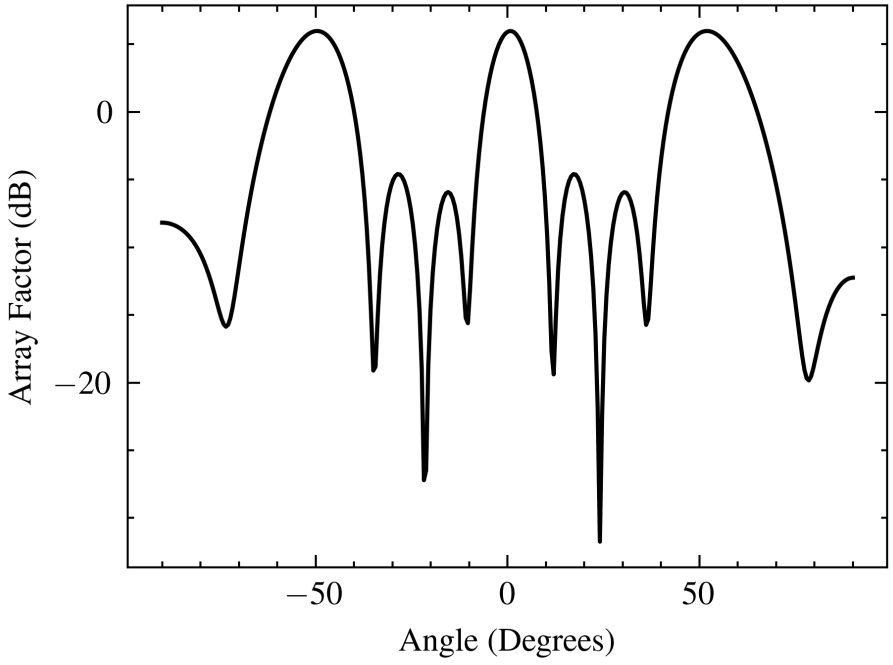

Figure 5.5. Theoretical array factor with equal phases and power.

5.3 FEED LINE

The feed line, shown in Figure 5.6, is responsible for distributing the incident wave with equal power to the branches. The feed line comprises power splitters that route power into the branches. Each divider is designed to divide the power such that each coupled port receives a quarter of the total power. This means that the first divider has a power split of 1:3, leaving three-quarters of the power at the second divider, which has a split of 1:2. The last divider receives two-quarters of the total input

power and divides the power equally. At the end of the feed line, there is a 90° corner to feed the final branch.

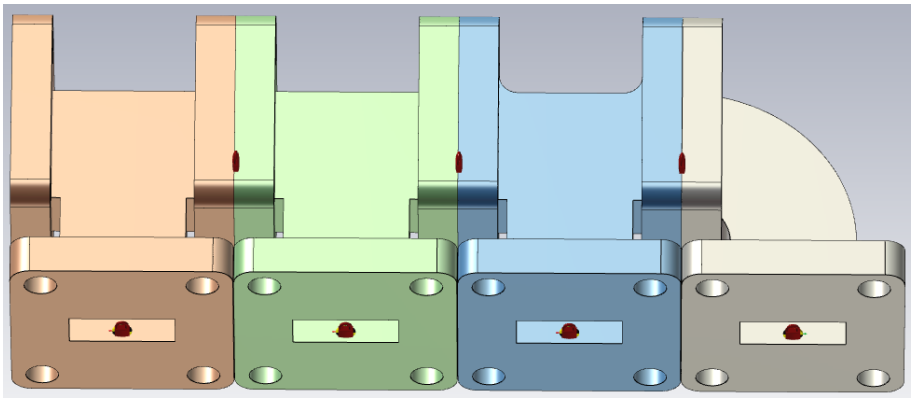

Figure 5.6. Image of the feed line. Each component is shown in a different colour. The input wave travels from the left to the right.

The dimensions of the power dividers for a specific power split can be found using [68]. The power dividers are made from a T-junction rectangular waveguide. The perpendicular output contains an inductive iris while a fin is inserted between ports 1 and 3, which assists with the input match. The design discussed here was chosen because it is the most compact and easily integrates into K-band waveguides. The geometry is also easy to print as a single piece without internal support. A disadvantage of the design is that the power split ratio varies over its band of operation. The power divider dimensions were designed to have a length Wd of 22.5 mm spacing between input and through ports to realise the element spacing mentioned in Section 3.2. Three variables control the power split ratio: the septum offset (l_o), the septum length (l_I) and the iris width (W_i). The septum offset is the distance of how much the septum is shifted to the through port from the centre of the divider. The septum is halfway between the input and through port when l_o is zero. S_{11} is closely related to the septum offset (l_o). The iris width (W_i) and the septum length (l_I) affect the frequency at which the S_{11} is minimum. The iris width (W_i) and the septum length (l_I) also control the power split ratio. An increase in the iris width (W_i) decreases the power at the coupled port while increasing the power at the through port. The converse is true when decreasing the iris width (W_i). The iris width (W_i) and the septum length (l_I) were found to have no effect on the S_{11} magnitude. The relationship between variables was, therefore, relatively simple. The septum length (l_I) and iris width (W_i) were adjusted contrarily to control the power split and adjusted similarly to position the S_{11} minimum, while the septum length (l_I) was adjusted to control the S_{11} magnitude. The clear relationships between variables

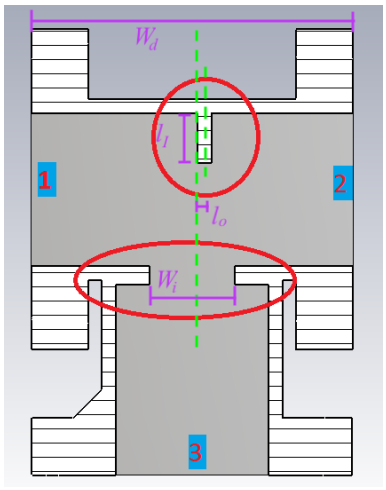

Figure 5.7. Section view of a single power divider. The iris and septum are circled. The input (1), through (2) and coupled (3) ports are labelled.

meant that the power divider could be easily hand-tuned and then fine-tuned using an optimiser. Only three optimiser goals were used: to minimise S_{11} and to have the power at the output ports equal to the desired values for each power divider. The effects of the various parameters are summarised in Table 5.2.

Table 5.2. Power divider parameter variation affects.

		S_{11}	S_{21}	S_{31}
Offset	Increase	Increases or decreases S_{11}	No change	No change
	Decrease	Increases or decreases S_{11}	No change	No change
Iris Thickness	Increase	Shifts S_{11} minimum to higher frequency	Decrease power at port 2	Decrease at port 3
	Decrease	Shifts S_{11} minimum to lower frequency	Increase power at port 2	Power increase at port 2
Septum Length	Increase	Moves S_{11} minimum to a lower frequency. Increases or decrease S_{11} minimum	Increase power to port 2	Decrease power to port 3
	Decrease	Moves $S_{11}1$ minimum to a higher frequency. Increases or decrease S_{11} minimum	Decrease power to port 2	Increase power to port 3

The S-parameters found from simulation are shown below in Figures 5.8, 5.9 and 5.10. The achieved power at the coupled port of the first divider is -6.05 dB, while -1.36 dB passes through to the next power divider. This provides a ratio of 0.248:0.731, close to the ideal ratio of 0.25:0.75. The second power divider (Figure 5.9) had -5.10 dB of the input power passed to the coupled port while -1.77 dB passed through to the through port. This provides a ratio of 0.31:0.67 versus the desired split of 0.33:0.67. The final power divider (Figure 5.10) splits the power equally at each port. Each port receives -3.15 dB of the input power. This means that the power split ratio is 0.48:0.48 while 0.5: 0.5 is desired. The antecedent and consequent of the power ratio do not add up to 1 due to losses, which is the case for all dividers.

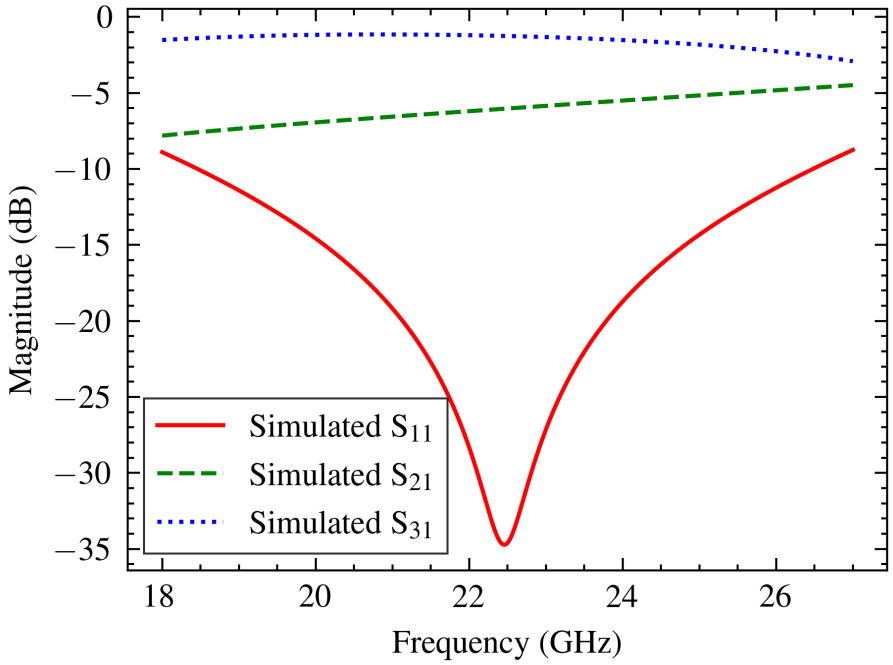

Figure 5.8. First power divider with a power split of 1:3.

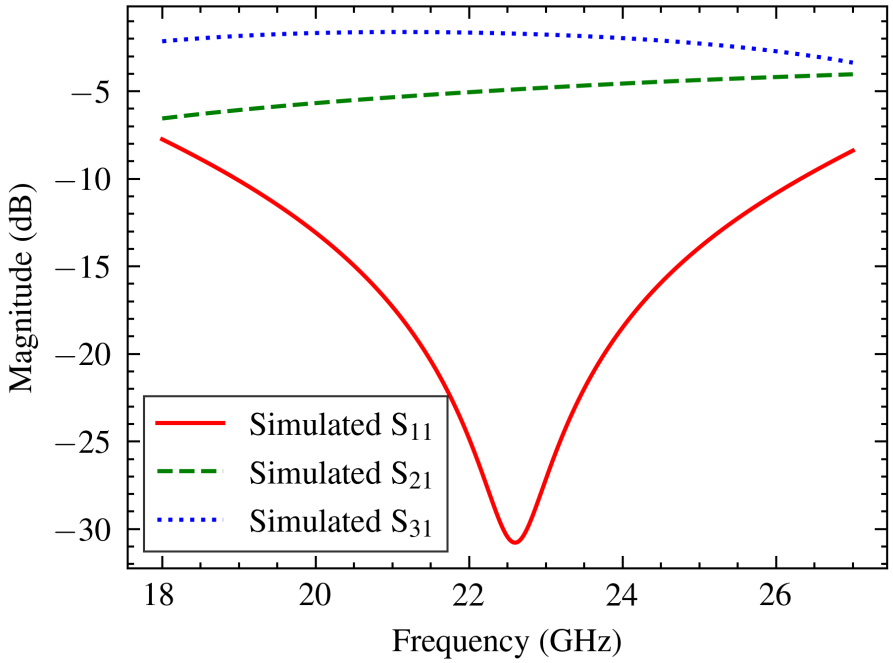

Figure 5.9. Second power divider with a power split of 1:2.

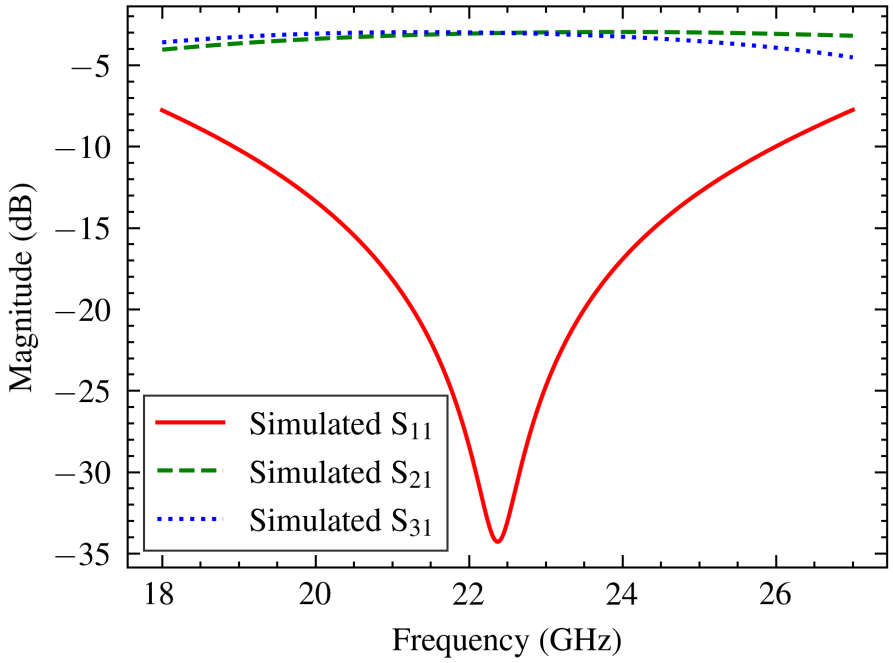

Figure 5.10. Third power divider with a power split of 1:1.

An SLM and an SLA printed power divider are shown in Figure 5.11. Distortion of the SLM flange

face can be seen where the flange is not reflective. These distortions were a result of the SLM printing process.

Figure 5.11. Manufactured SLA and SLM power dividers.

5.3.1 Slow wave lines

The sinusoidal slow wave line mentioned in the previous section was chosen for its simplicity and ability to be printed without internal supports. The waveguide resembles a rectangular waveguide with sinusoidal corrugations perpendicular to the propagation direction. These corrugations are only present on the top and bottom walls, which has a low pass effect on the propagating signal.

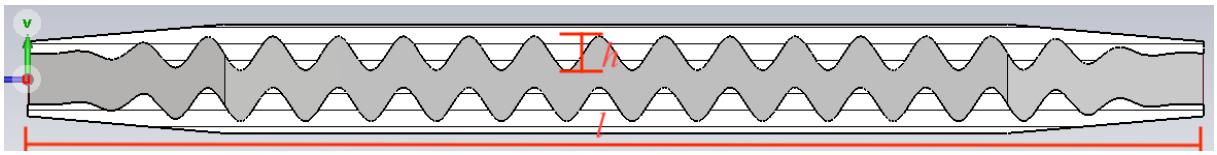

Figure 5.12. Cross section of the sinusoidal guide.

The width (w) of the waveguide, length (l) and the number of periods in the tube are controlled to achieve a desired time delay. Figures 5.12 and 5.13 show the sinusoidal waveguide. The parameters

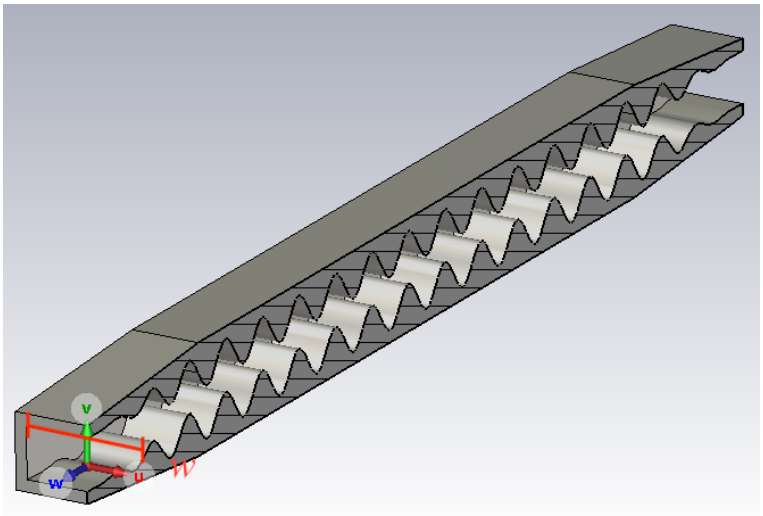

Figure 5.13. Sinusoidal slow waveguide.

Table 5.3. Effect of parameters on delay.

Parameter	Change	Group Delay
Tube Periods (P)	Increase	Increase in time delay
	Decrease	Decrease in time delay
Amplitude (h)	Increase	Increases time delay
	Decrease	Decreases time delay
Width Increase (w)	Increase/Decrease	Moves centre frequency inversely proportional to width change

being controlled are the group delays. They are controlled by varying the amplitude of the corrugations (h), the period of corrugations (P), the width of the guide (w) and the height between the top and bottom walls. The delay is proportional to the guide's length (l) and the corrugations' amplitude. For the array network, the lengths (l) of the sinusoidal waveguides are all the same to maintain the correct linear element arrangement. The amplitude of the corrugations (h) and the width (w) were then adjusted to achieve the desired time delay given a fixed waveguide length. No calculation for the time delay is given in [28]. The time delay is not calculated but instead found through simulation. Improved delay bandwidth can be achieved at the expense of length and increased delay. Twelve periods (P) were found to be a good trade-off between length and delay for this work. The relationship (shown in Table 5.3) between the various parameters and the group delay was determined by hand-tuning the time delays to values near their target. The data were then fitted to a curve to find an analytical relationship between the increase and the sinusoid amplitude that could then be used in CST to find the

dimensions of the guide from the desired group delay. The width increase of branch three was easily found by hand and had little effect other than shifting the frequency where the desired delay occurs. Equation (5.1) is the fitted equation for the amplitude of the sinusoid; the width increase is given by (5.2) and is plotted in Figure 5.14 against the desired delay (d).

$$h = 82.3154 + \frac{-146.8031}{1 + (d/47.8024)^{0.0473635}} \tag{5.1}$$

$$w = -2.3 + \frac{96.391}{2^{d/0.100539}} \tag{5.2}$$

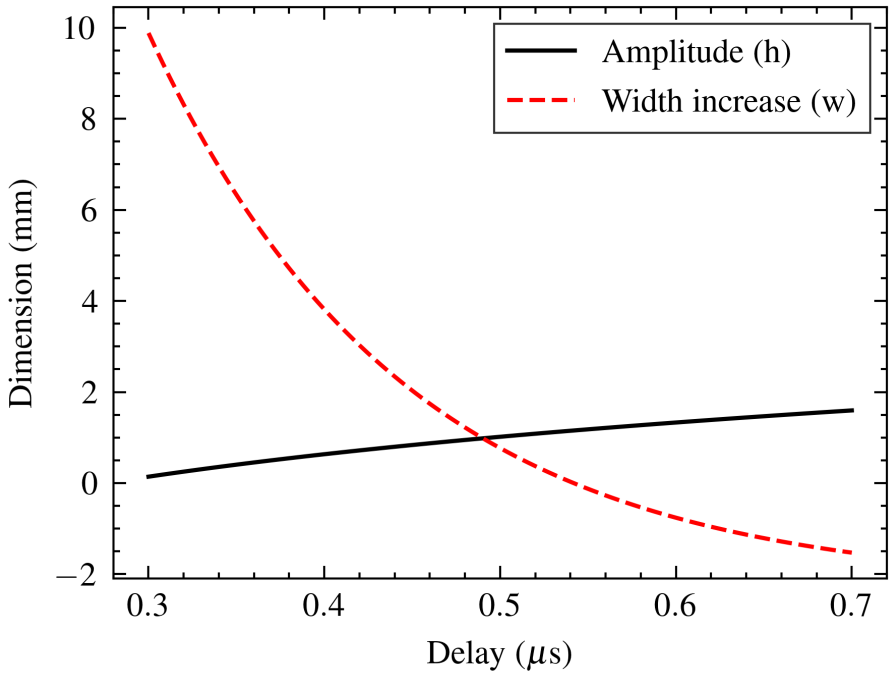

Figure 5.14. Sweep of the width increase and the amplitude of the sinusoid pattern.

Table 5.4. Final parameter found using simulation.

Parameter	Branch 1 (mm)	Branch 2 (mm)	Branch 3 (mm)
Delay (μs)	0.638	0.62	0.410
Periods (P)	12	12	12
Sinusoid Amplitude (h) (mm)	1.435	1.387	0.680
Width (w) (mm)	9.557	9.288	16.668

Figure 5.15 shows the time delay simulation results. In an ideal case, the time delay would be as flat as possible to ensure maximum bandwidth. The time delays here show some errors at the band edges.

The error depends on the time delay being provided, and greater time delays cause the error to increase more quickly at the band edges.

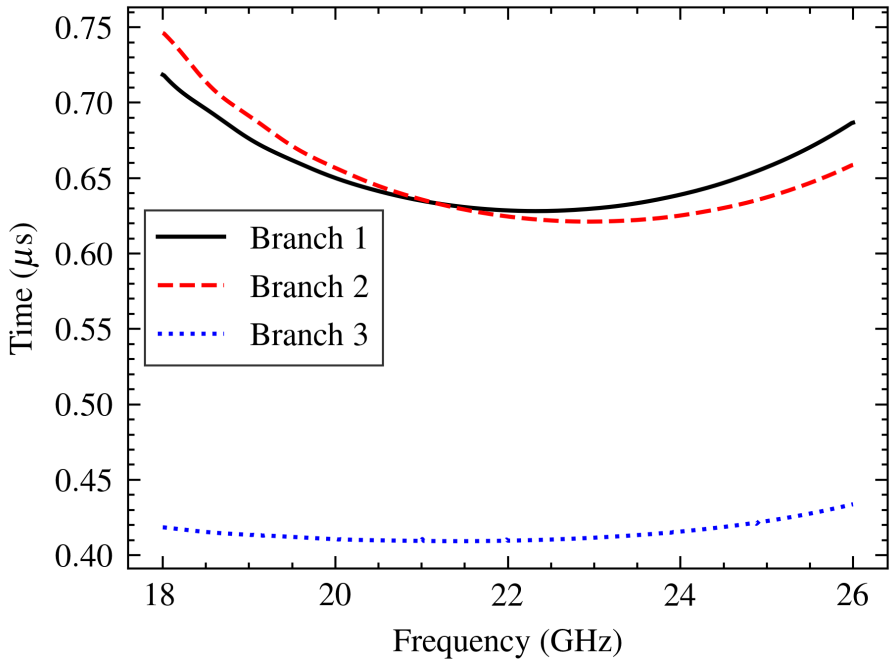

Figure 5.15. Simulated group delay of the chosen time delay.

The manufactured horn and straight waveguide section are shown in Figure 5.16. The corrugation can be seen on the inside of the delay.

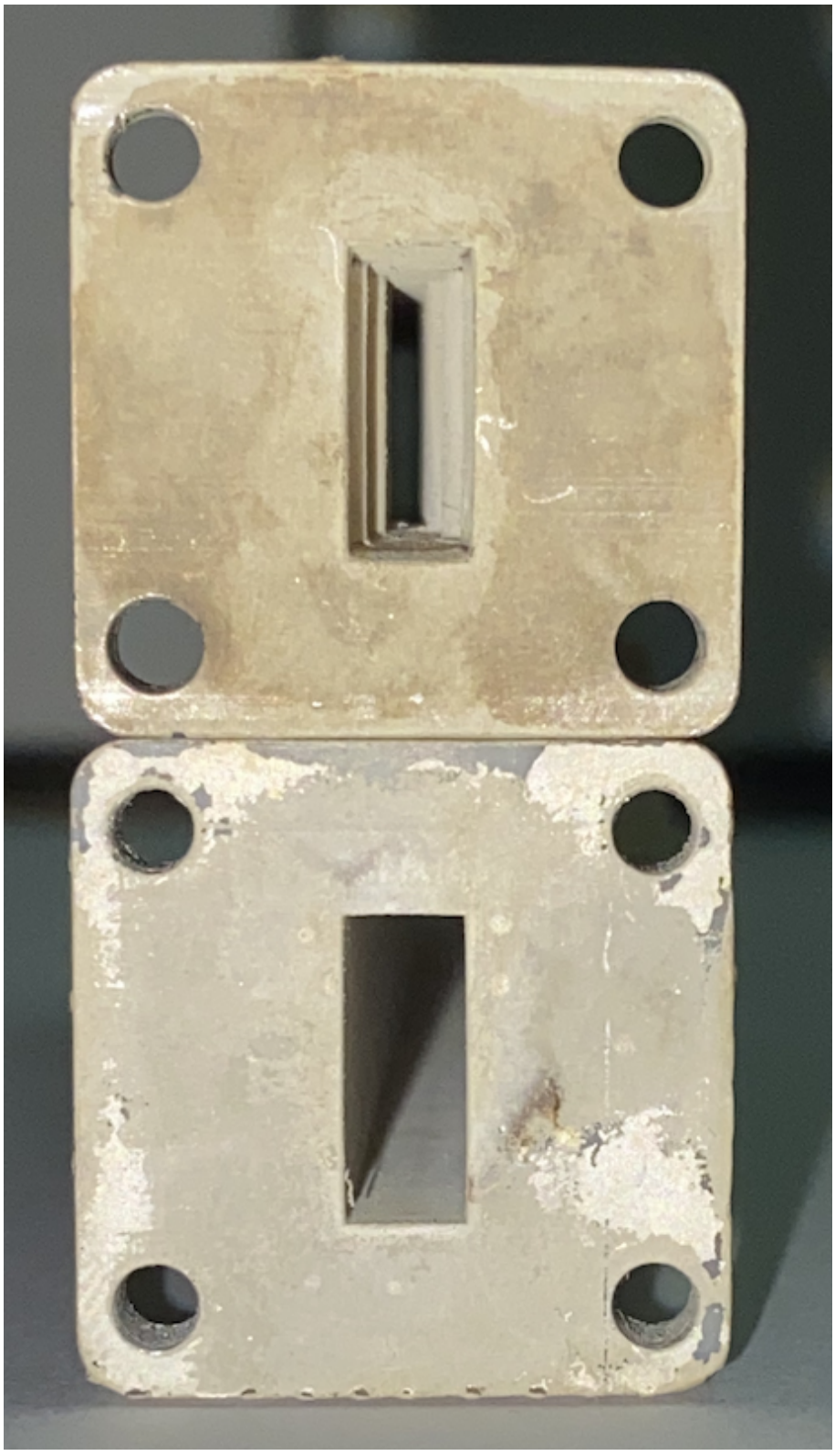

Figure 5.16. SLA time delay on top of a waveguide section. The corrugations inside the waveguide can be seen compared to the straight section.

5.3.2 Horn antennas

The horn antennas, shown in Figure 5.17, were based on the dimensions of a commercially available antenna. The flare length was varied, but the aspect ratio of the aperture was kept constant. The dimensions of the horn antenna were limited since the horns of the array needed to fit next to each other. The dimension of the aperture was adjusted so the horns could fit next to one another without the flares touching. The length of the horn was adjusted to achieve high gain while also limiting the length so that the horn is not unreasonably large. The gain of the horn was analysed using the relations given in [14].

The gain of a horn antenna can be calculated using

$$G = \frac{4\pi}{\lambda^2}\varepsilon_t AB\varepsilon_{ph}^H\varepsilon_{ph}^E \tag{5.3}$$

where A and B are the height and width of the aperture, ε_{ph}^E and ε_{ph}^H are the phase efficiencies of the E and H planes, and ε_t is the taper efficiency of a rectangular aperture. ε_{ph}^E is calculated using

$$\varepsilon_{\text{ph}}^E = \frac{C^2(q)+S^2(q)}{q^2}. \tag{5.4}$$

The value of q is found using

$$q = 2\sqrt{\frac{B^2}{8\lambda R_2}}, \tag{5.5}$$

with B being the height of the horn aperture and R_2 the length of the flare in the E-plane. Functions C and S are the cosine and sine Fresnel integrals, respectively. ε_{ph}^H is found using

$$\varepsilon_{\text{ph}}^H = \frac{\pi^2}{64t}\left\{[C(p_1)-C(p_2)]^2+[S(p_1)-S(p_2)]^2\right\}, \tag{5.6}$$

where C and S are again the cosine and sine Fresnel integrals. The value of p_1 is found using

$$p_1 = 2\sqrt{t}\left[1+\frac{1}{8t}\right], \tag{5.7}$$

and p_2 is

$$p_2 = 2\sqrt{t}\left[-1+\frac{1}{8t}\right]. \tag{5.8}$$

The value of t is found using

$$t = \frac{A^2}{8\lambda R_1}, \tag{5.9}$$

where A is the width of the aperture and R_1 is the length of the flare in the H-plane, ε_t is the efficiency of a rectangular aperture which is equal to 0.81. With the flare R_1 equal to 37.26 mm, R_2 equal to 50.4 mm, B as 15.24 mm and A equal to 19.47 mm, the values of q and t are 0.058 and 0.095. ε_{ph}^E is then found as 0.988 and ε_{ph}^H is found as 0.985. The gain is then found using (5.3), which gives a gain of 12.2 dBi at 22.5 GHz.

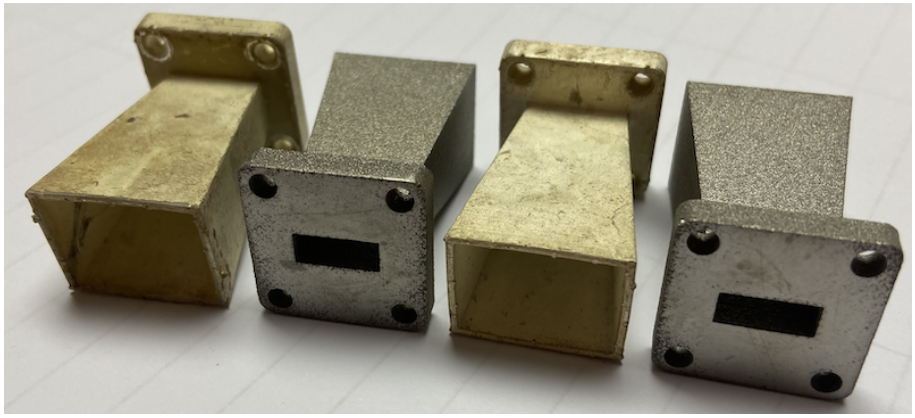

Figure 5.17. Image of the manufactured SLA and SLM horns.

In Figures 5.18 and 5.19 the simulated farfield pattern of the horn antenna is shown. The beam's peak has a gain of 12.1 dBi at the centre of the band, equal to the theoretical gain. The beam has a half-power beamwidth of 29.9 degrees in the H-plane plane and 20° in the E-plane.

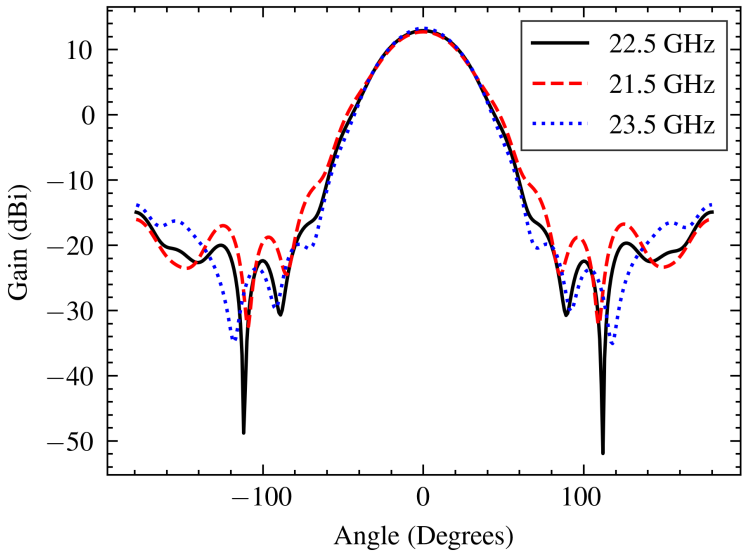

Figure 5.18. Simulated co-polar azimuth pattern of the horn antenna.

At 18 GHz, the gain of the horn is reduced to 9.5 dBi. At 27 GHz, there is a slightly greater gain at 14.1 dBi. The shape of the radiation pattern remains similar despite the variation in gain.

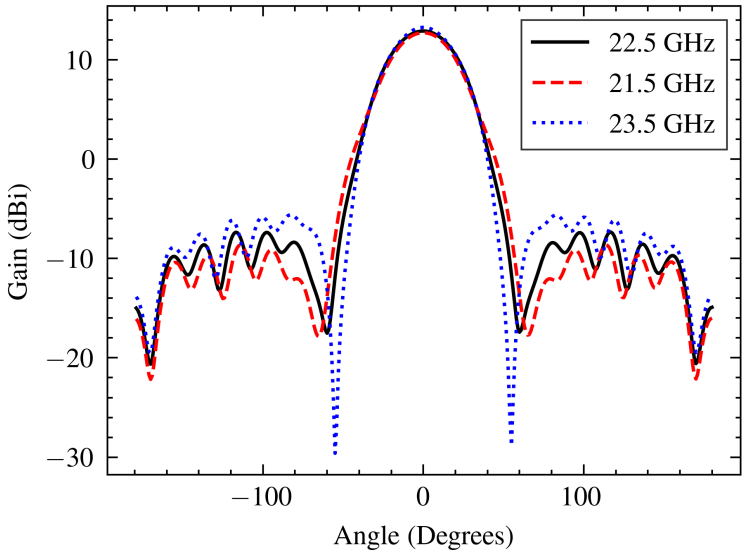

Figure 5.19. Simulated co-polar elevation pattern of the horn antenna.

The cross-polar patterns are shown in Figures 5.20 and 5.21. In all cases, the cross-polar pattern is at least 50 dB below the co-polar pattern. This result is expected for the vertically polarised horn antenna.

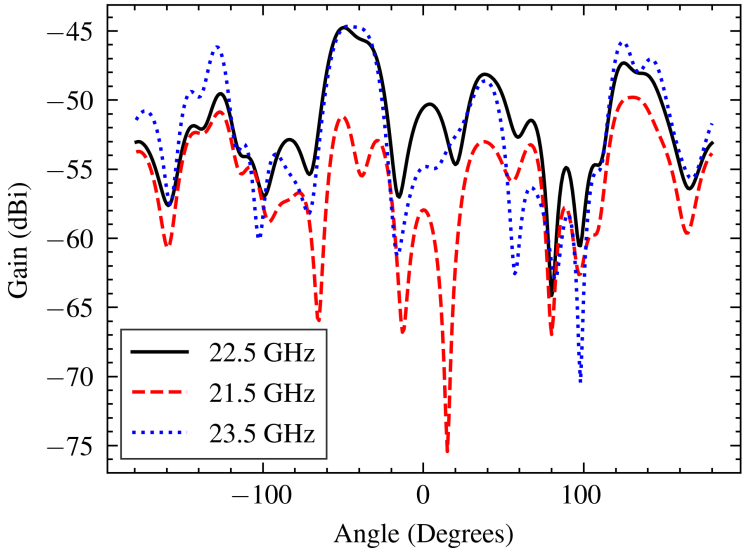

Figure 5.20. Simulated cross-polar elevation pattern of the horn antenna.

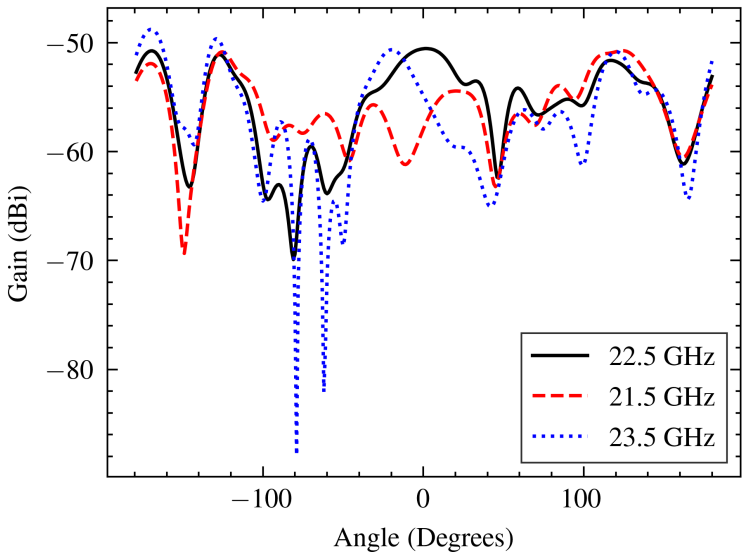

Figure 5.21. Simulated cross-polar elevation pattern of the horn antenna.

The assembled antenna array is shown in Figure 5.22. The four output horns can be seen on the left side of the image. The input is on the top right of the array.

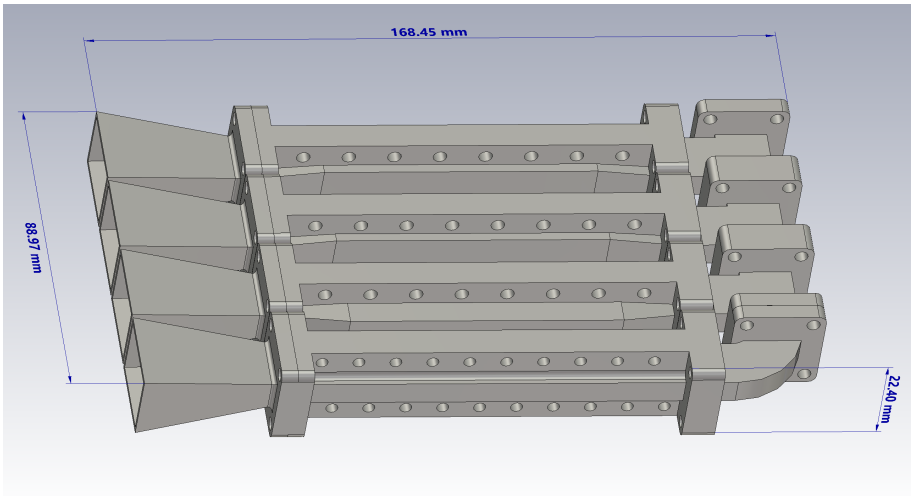

Figure 5.22. CAD model of the horn array.

The simulated co-polar far-field patterns of the array are shown in Figure 5.23. The grating lobes are 30° from boresight and have a gain of 10.31 dBi. This reduction is due to the directivity of the horns. The main lobe has a gain of 18.89 dBi. Above 23.5 GHz, the side lobes increase to 12 dBi. At 26.5

GHz, the time delays can no longer ensure the correct phases at the outputs of the array, and the pattern no longer has a main lobe at the front of the antenna.

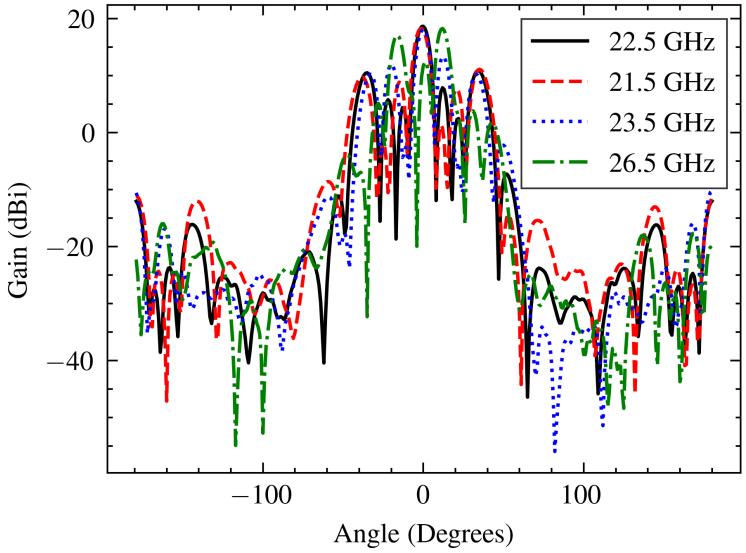

Figure 5.23. Farfield results of the 3D EM simulation of the co-polar azimuth pattern.

The effect on the limited bandwidth of the time delay elements is visible by the pattern when operating at 18 GHz or 27 GHz. Figure 5.24 shows the array pattern but with the time delays replaced with straight sections. By comparing Figures 5.23 and 5.24 the effect of the time delays on squint can be seen.

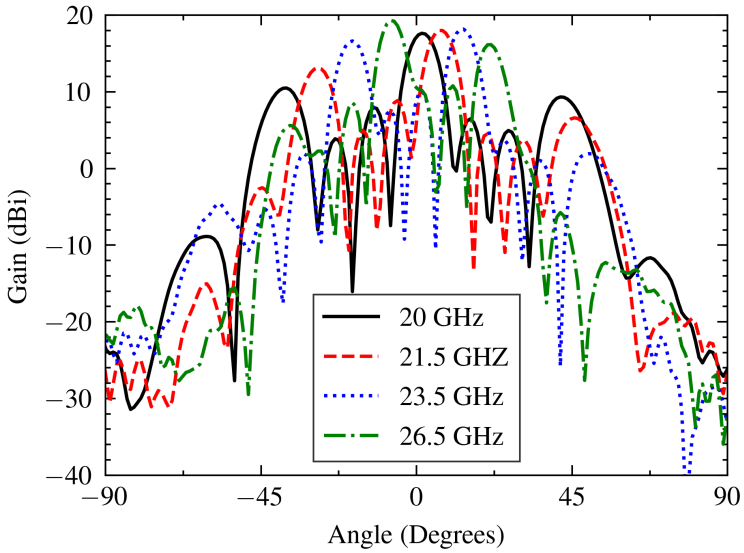

Figure 5.24. Array pattern with the time delays replaced with straight section. The pattern shifts to the right as frequency increases.

The angle of the simulated main lobe with and without time delays is shown in Figure 5.25. Without time delays the array pattern shifts to the right as frequency increases until a grating lobe moves to boresight. This result shows how the beam pattern is improved by adding the time delay sections.

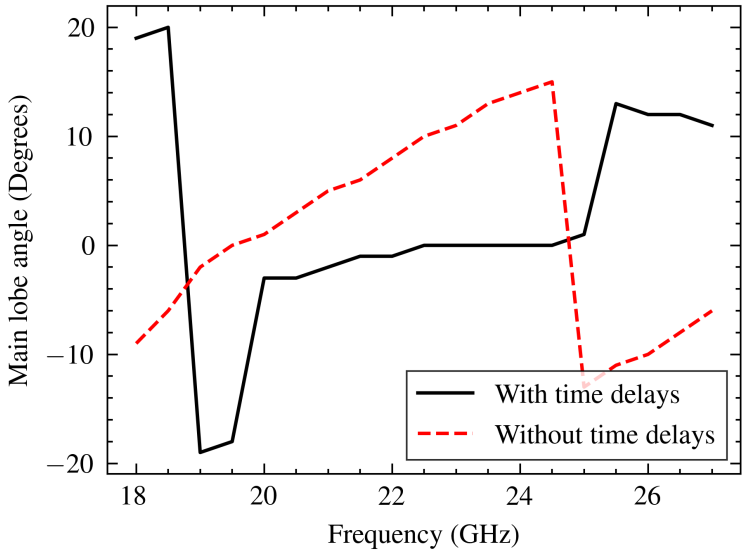

Figure 5.25. Simulated main lobe angle with and without time delays. The sudden change in angle of the array without time delays is caused by the grating lobe having a larger beam gain than the original main lobe as it moves to boresight.

The elevation pattern for the array with time delays in Figure 5.23 has a peak fixed in frequency and a gain greater than the individual horn antenna, as expected. The reduced gain at 26.5 GHz corresponds to the reduced azimuth pattern in Figure 5.26, where the boresight gain is notably depressed. The

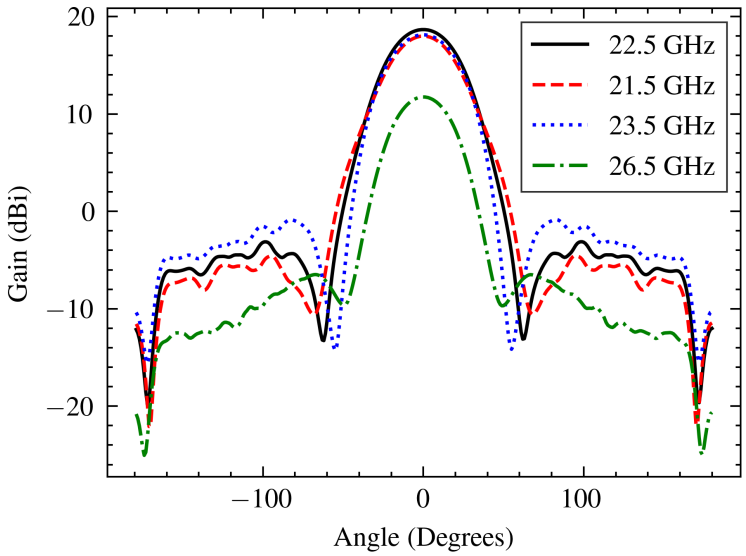

Figure 5.26. Co-polar elevation pattern of the 3D EM simulation.

cross-polar azimuth and elevation are shown in Figures 5.27 and 5.28. The cross-polarisation levels are at least 40 dB below the co-polarised levels, as there are no significant features that can couple between co-polar and cross-polar polarisations in the simulation.

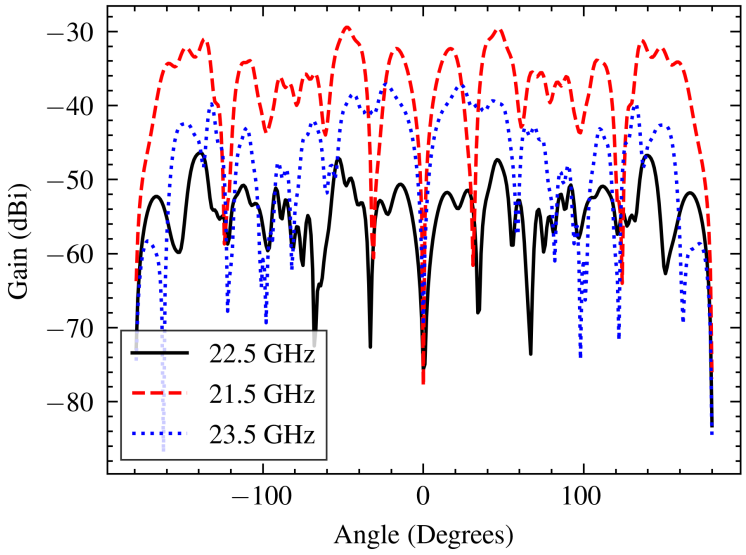

Figure 5.28. Cross-polar elevation pattern of the 3D EM simulation.

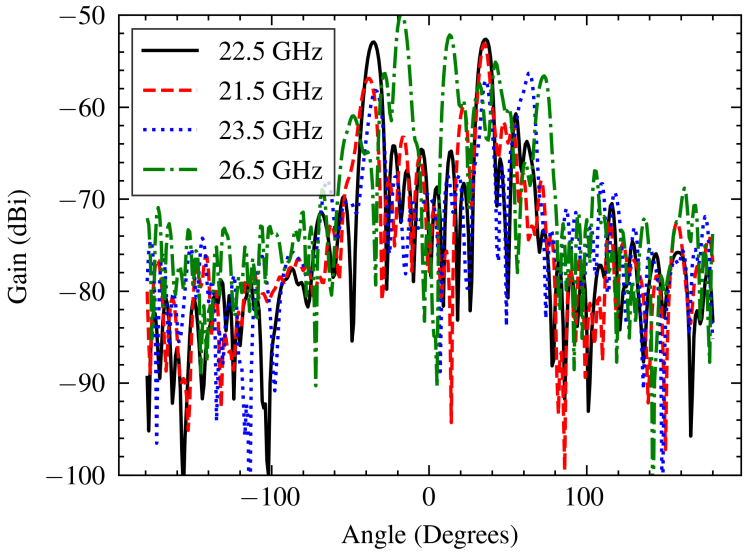

Figure 5.27. Cross-polar azimuth pattern of the 3D EM simulation.

The simulated far-field patterns show the array works as intended. The time delays do manage to equalise the phases at the outputs of the array.

5.4 MEASURED PERFORMANCE RESULTS

5.4.1 Time delays

The three time delay sections were manufactured and measured on a VNA to verify their loss and group delay. A time delay is being measured in Figure 5.29. Figure 5.30 shows the transmission magnitude of the time delays, as well as a straight section made with white resin and silver plating. Branch 3 has the smallest delay while branch one has the greatest delay. The higher the delay, the longer the effective internal path length of the geometry is, which increases the loss of the waveguide. To improve the losses, branch 1 underwent a further four rounds of silver plating for a total of eight rounds, reducing the loss to less than branch 2. Internal clearances inside the delay limit the flow of the plating solution resulting in a limited amount of silver forming inside the time delay. This result illustrates the need for extra plating rounds when the plating solution cannot flow through the waveguide. The S_{11} results of the time delay sections in Figure 5.31, show a similar result, with branches 1 and 3 performing better than branch 2. An interesting observation was that branches 1 and 3 achieved similar or better reflection coefficient than simulation at the lower end of the band. As the frequency increases, the simulated results are better. Branch 1's worst reflection coefficient was -18 dB. For branch 3 the worst reflection coefficient was -22 dB. Branch 2 achieved the worst reflection coefficient of -12 dB. The poorer performance of branch 2, compared to the final branch 1 result, can be attributed to having only

four rounds of silver plating while having narrower geometries inside the waveguide.

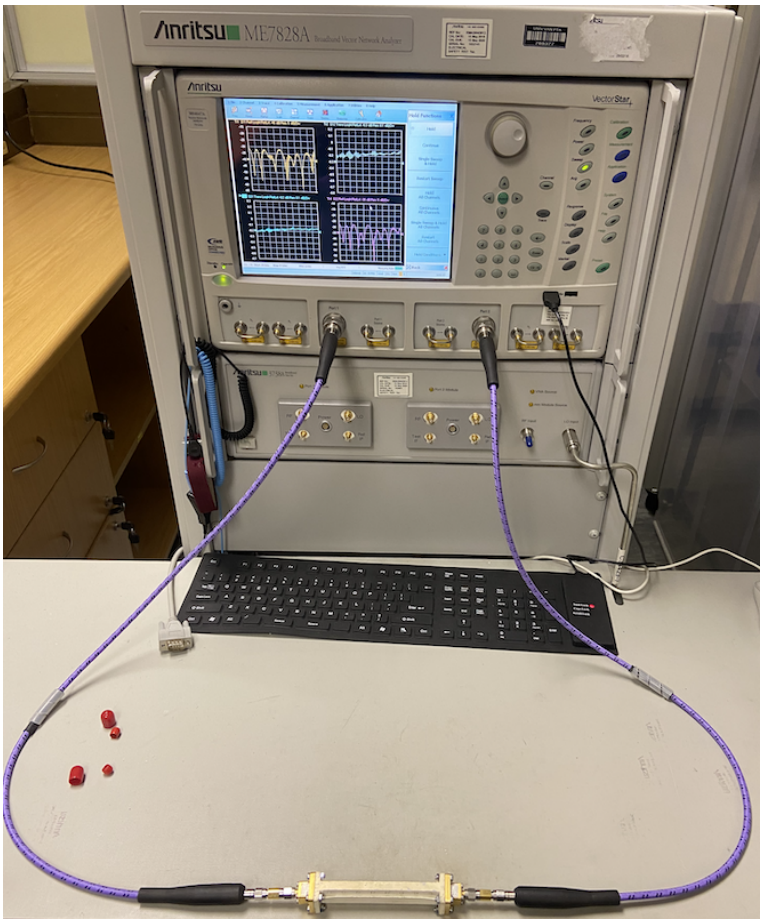

Figure 5.29. Time delay waveguide being measured on the Anritsu MS4647A VNA.

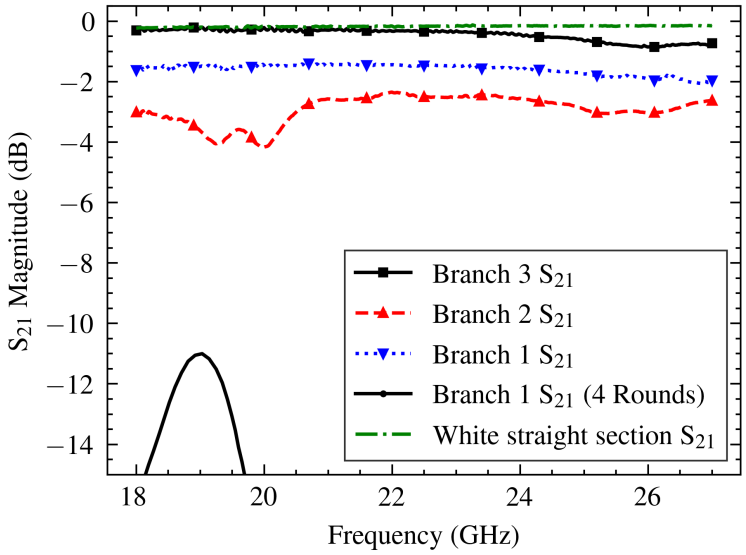

Figure 5.30. S_{21} of the SLA time delays.

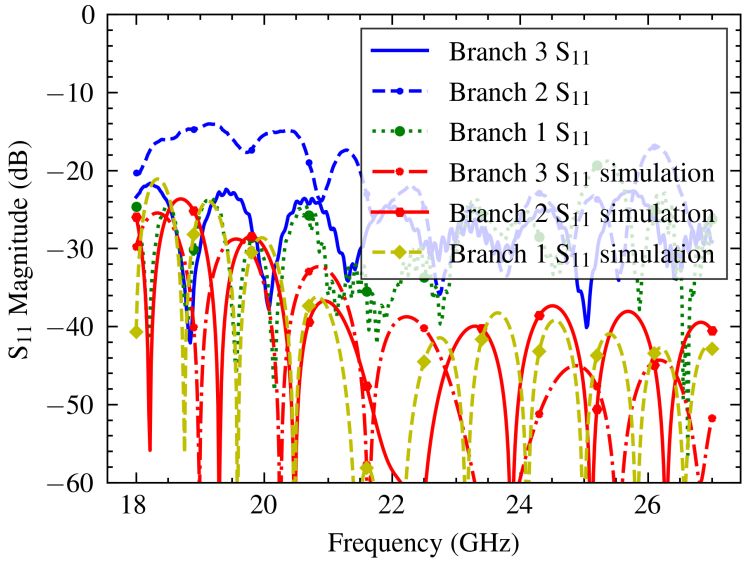

Figure 5.31. S_{21} of the SLA time delays.

The group delay of the three branches is shown in Figure 5.32 and compared to the simulation. The delay sections matched the simulated response with some measurement noise due to the differential operation on the measured data. The differing number of plating rounds did not affect the group delay of time delays.

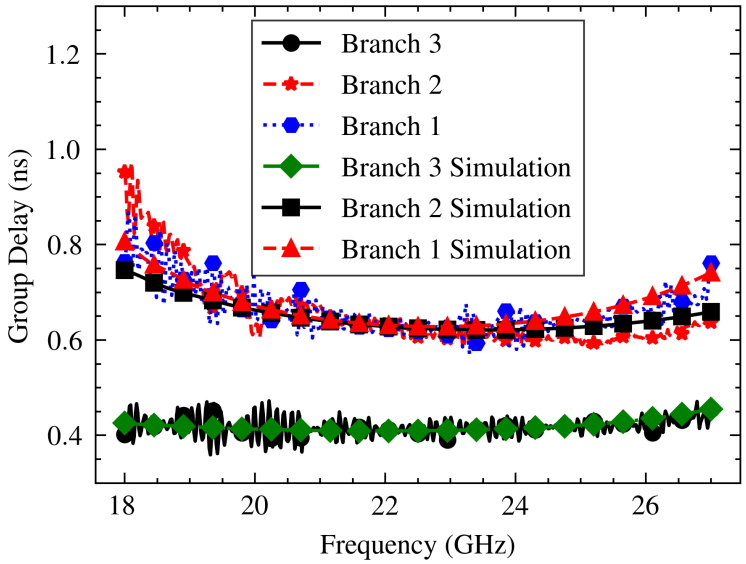

Figure 5.32. Group delay of the SLA time delays.

The SLM time delays exhibited more loss than the SLA waveguides. Branch 3 had the lowest transmission loss, averaging less than 1 dB of insertion loss within the band 21.5 GHz to 23.5 GHz which increases to 1.5 dB above 26 GHz. Branch 2 follows branch 3 with an S_{21} of 2.6 dB, and branch 1 achieved 2.9 dB of transmission loss. The transmission loss of branches 2 and 1 exhibited narrowband peaks of up to 5 dB at 25.5 GHz. This appears to be an unmodelled resonance in the branches, especially accounting for the reflection coefficient in Figure 5.34, where there are peaks in reflection that coincide. The transmission responses for branches 3, 2 and 1 roughly translate to a loss of 15, 26 and 29 dB/m at midband. The high midband losses are attributed to the surface roughness. Since the surface area inside the time delays is greater, the loss of the time delays is expected to be greater than a straight section.

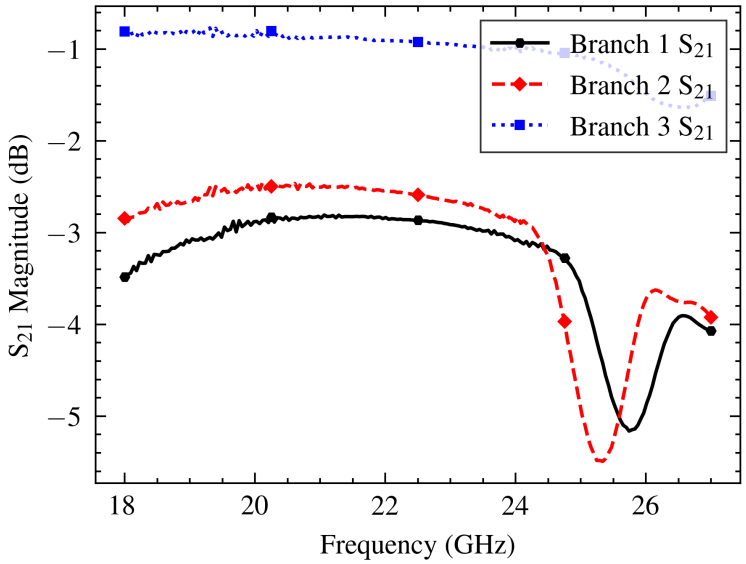

Figure 5.33. S_{21} of the SLM time delays.

The reflection coefficient, as seen in Figure 5.34, is better on average than the SLA parts except at 25.5 GHz, where the resonance causes a peak in reflection coefficient to above -6 dB. The lower reflection coefficients are a result of the flanges being skimmed. The reflection coefficient was worst at 25.5 GHz, where the reflection coefficient of branches one and two was greater than -10 dB. This could be attributed to the previously mentioned unmodelled resonance in the structure.

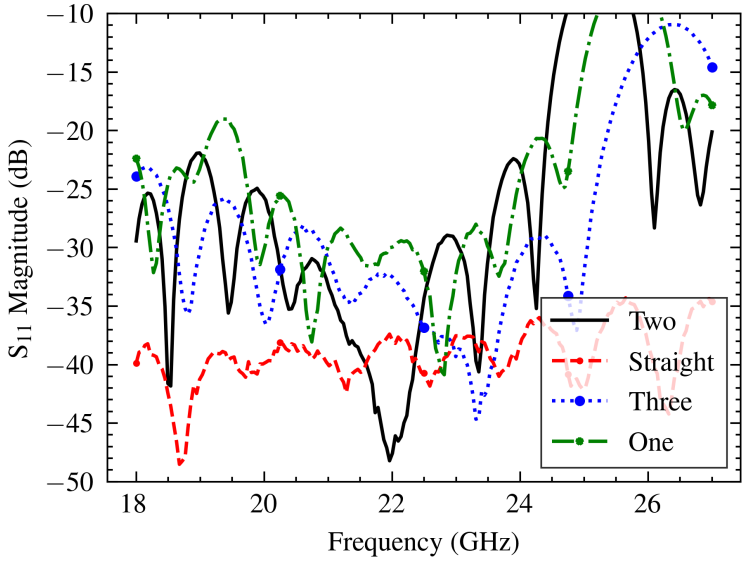

Figure 5.34. S_{11} of the SLM time delays.

Despite the SLM waveguides' higher insertion and reflection coefficients, the group delay remains unaffected. All branches produced similar results to the simulation, though branches 2 and 3 do deviate at 25.5 GHz. This effect is a further indication of an unmodeled resonance.

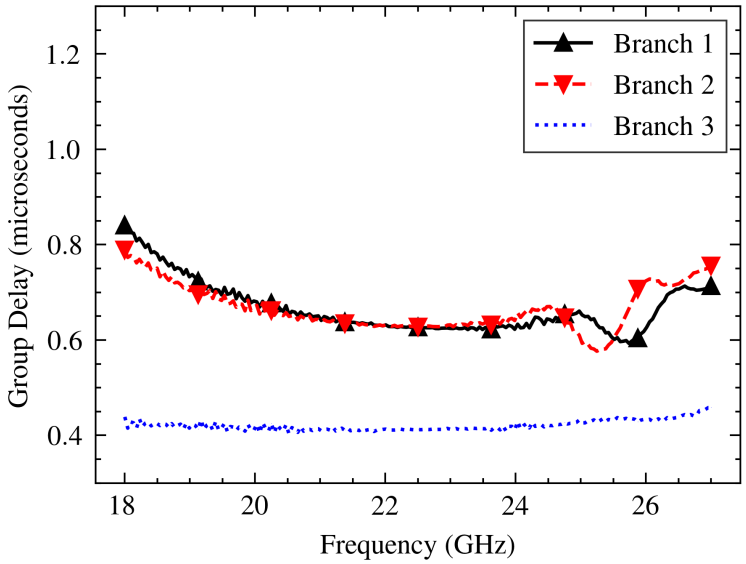

Figure 5.35. S_{11} of the SLM time delays.

5.4.2 Power dividers

In Figures 5.36, 5.37 and 5.38 S_{21} and S_{31} are shown for the three power dividers. In Figure 5.36, the first branch with a ratio of 3:1 is shown. In all cases, the SLM parts are expected to provide the best S_{11}. However, there was some distortion on the flange of branch one, which slightly changed the dimensions of the waveguide leading to a greater S_{11} for the SLM parts than the SLA parts. The SLA and SLM parts closely matched the S_{21} and S_{31} responses in simulation. For divider two, the SLM waveguide had a lower reflection coefficient than the SLA waveguide, which was attributed to the skimming of the SLM flanges. Again the SLA and SLM divider closely matched the S_{21} and S_{31} responses in simulation, with the SLM waveguide deviating more than the SLA waveguide from the simulated S_{31}. The opposite was true for the S_{21}. The insertion loss for the final divider was again similar to the simulation, with the SLM and SLA divider almost achieving the same reflection coefficient achieved in the simulation. Again the SLM divider deviated slightly more than the SLA waveguide from the simulated S_{21} and S_{31} responses.

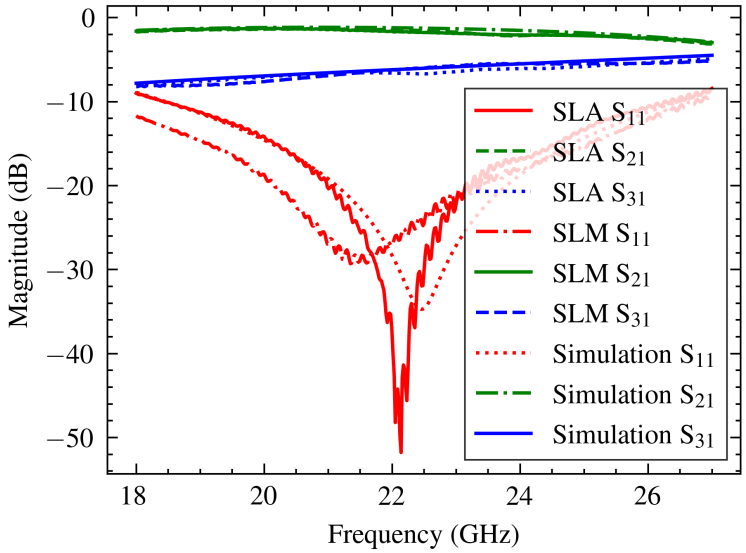

Figure 5.36. First power divider with a power split of 3:1.

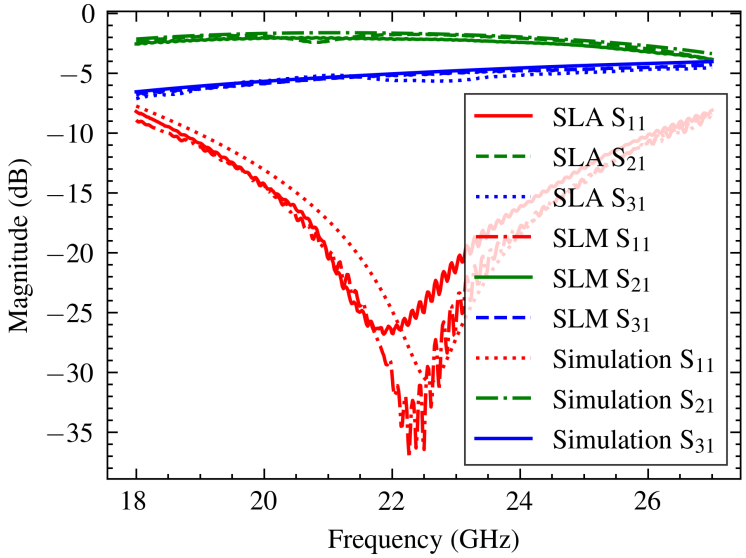

Figure 5.37. Second power divider with a power split of 2:1.

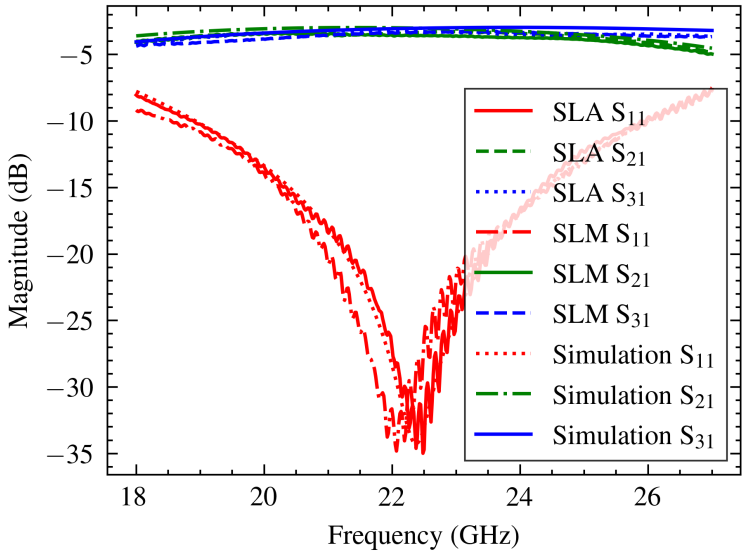

Figure 5.38. Third power divider with a power split of 1:1.

5.4.3 Feed network

5.4.3.1 SLA feed network

The S-parameters of the assembled feed network with time delay sections are shown in 5.39. These were measured with the horns removed to show the power and delay of signals arriving at the horns. The magnitude response of the horn antennas is uniform within 2 dB inside the band of 21.5 GHz to 23.5 GHz. The reflection coefficient was less than -22.5 dB which translates to a maximum VSWR of 1.16.

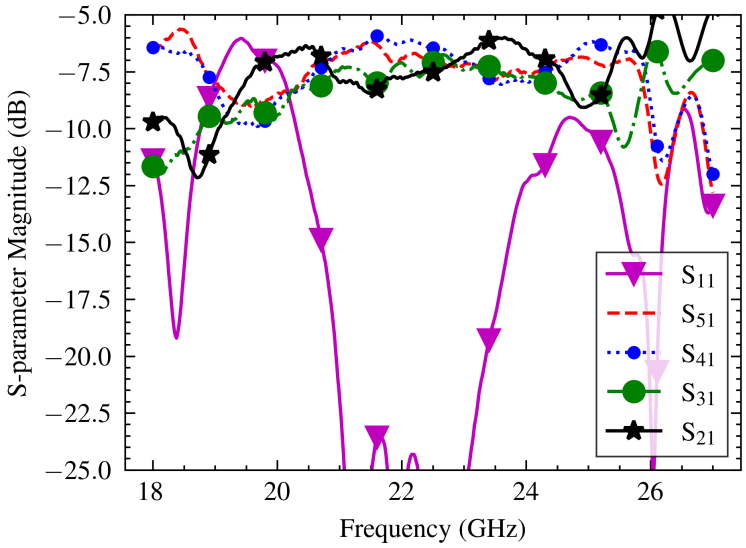

Figure 5.39. S-parameters of the feed network.

The second metric being verified is the group delay to each horn, shown in Figure 5.40, measured from the input port to each output. The delay to the outputs is similar in the band, leading to a similar phase at the output of the horns, which is needed to achieve the correct beam pattern. When compared to the individual group delays in Figure 5.32, it is apparent that there is a larger deviation in group delay. This is because the power dividers add some variability since their group delay cannot be controlled as strictly.

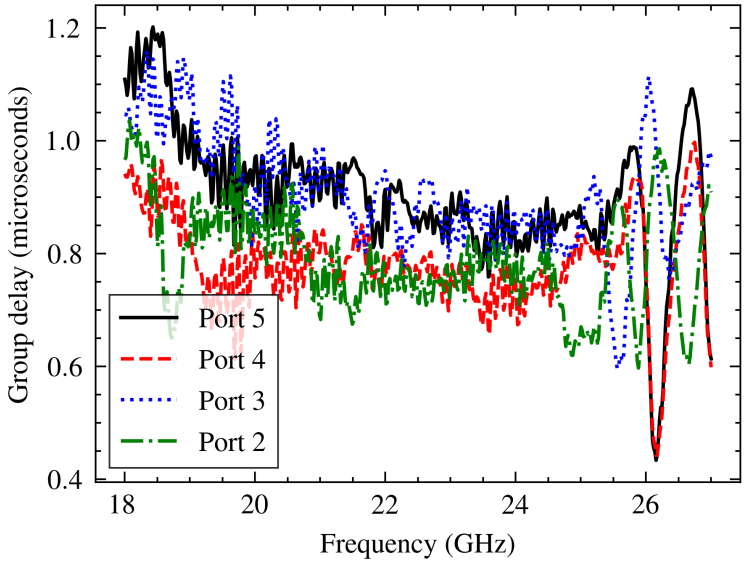

Figure 5.40. Group delay of the SLA feed network.

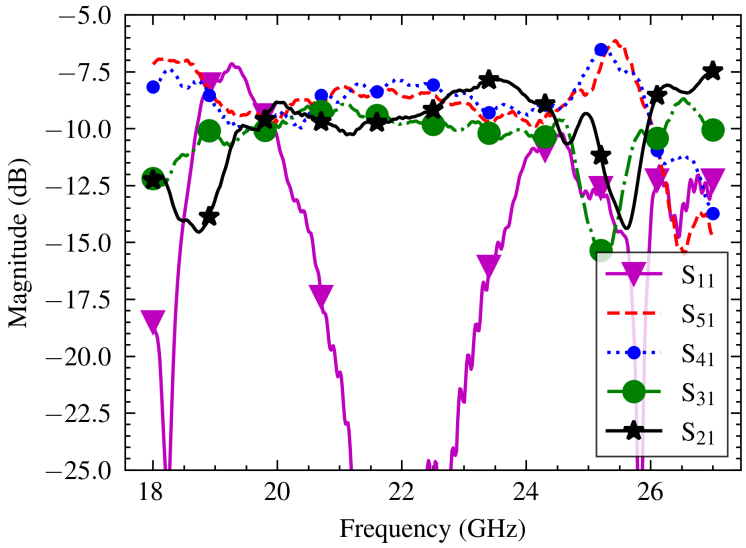

Figure 5.41. S-parameters of the SLM feed network.

5.4.3.2 SLM feed network

The S-parameter results of the SLM feed network are shown below in Figure 5.41. The SLM network had more losses, which was expected when considering individual losses of the branches. On average, losses were 2.5 dB more than the SLA network. There was also a larger difference in output powers between ports, which meant that one side of the array was transmitting more power than the other. The reflection coefficient peaked at -24 dB, with most of the reflection being less than -27 dB. The group delay is shown in Figure 5.42. The group delay of the SLM feed network follows a similar trend to that of the SLA network. The delay to ports two and four are similar, while ports three and five are similar. Similarly to the SLA network, the time delays are closest to each other at 23.5 GHz. The group delays remain largely unchanged by surface roughness and distortion, which is expected since the individual delays were similar to the simulation.

5.4.4 Horn antenna

The co-polarised azimuth pattern for the SLA and SLM horns is shown in Figure 5.43. The main lobe of SLM and SLA horns matched the simulated horn quite closely and the horns achieved a peak gain of 12.6 dBi at 22.5 GHz. This is similar to the theoretical and simulated result of 12.1 dBi. The back lobe does differ when comparing the simulated results to measured results, but this is still negligible.

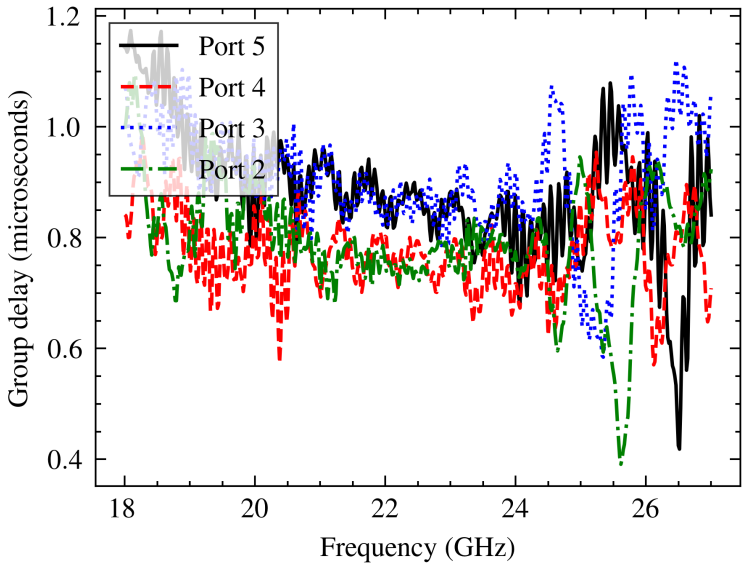

Figure 5.42. Group delay of the SLM feed network.

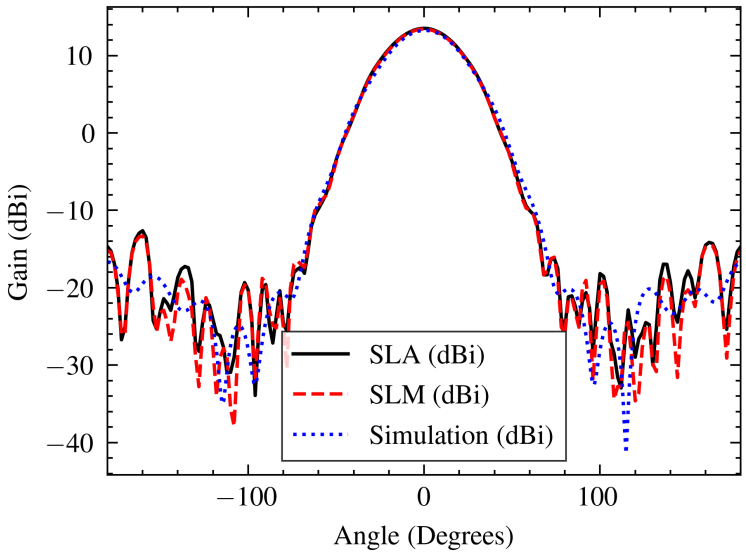

Figure 5.43. Horn antenna co-polar azimuth measurement 22.5 GHz.

The cross-polar result is shown in Figure 5.44, where the measured and simulated results differ significantly. The poor cross-polarisation is attributed to the surface roughness of the horns, as well as distortion of the horn geometry. Rough surfaces can introduce random scattering, which can increase cross-polarisation [69]. Similar results are seen at 21.5 and 23.5 GHz in Figures 5.45, 5.46, 5.47 and 5.48.

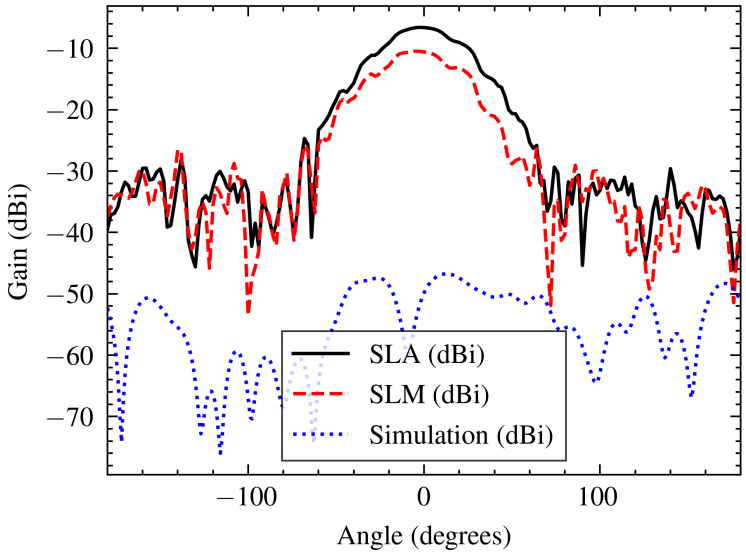

Figure 5.44. Horn antenna cross-polar azimuth measurement 22.5 GHz.

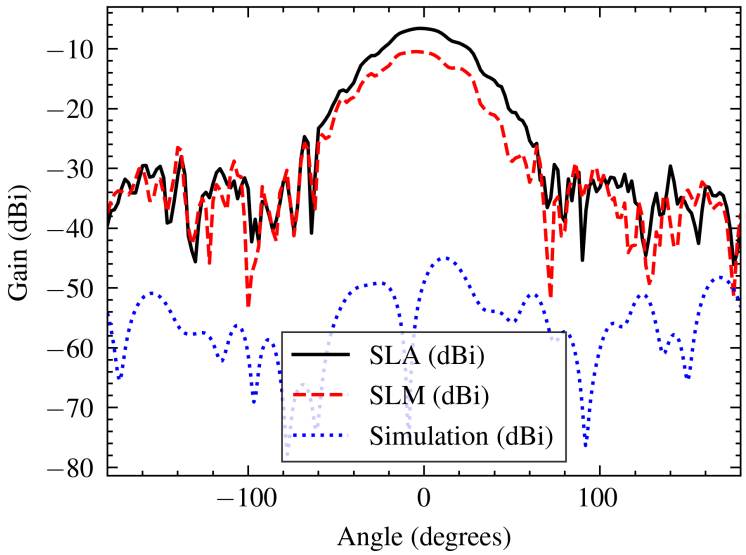

Figure 5.45. Horn antenna cross-polar azimuth measurement 21.5 GHz.

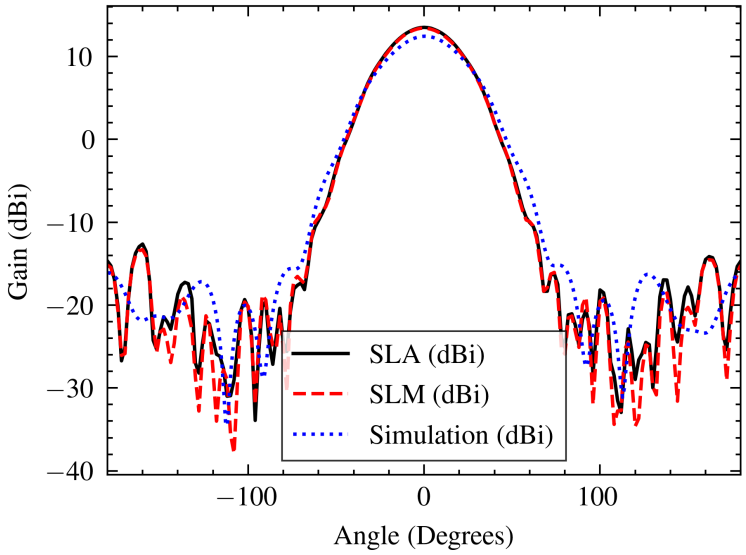

Figure 5.46. Horn antenna co-polar azimuth measurement 21.5 GHz.

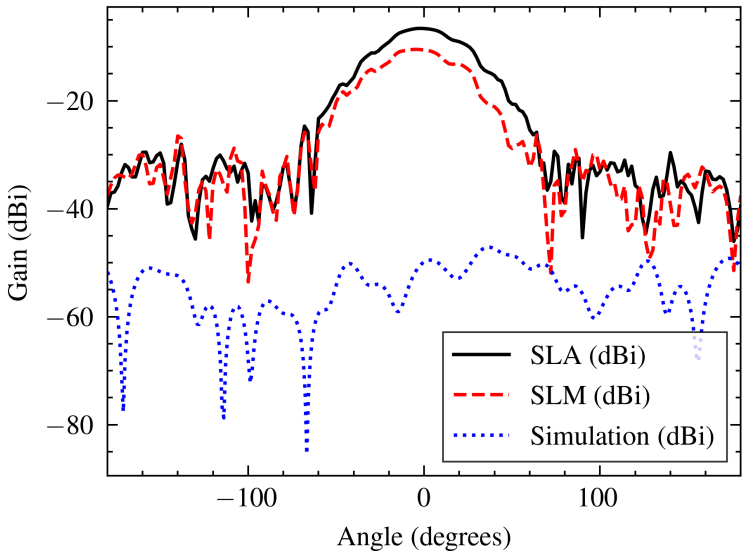

Figure 5.47. Horn antenna cross-polar azimuth measurement 23.5 GHz.

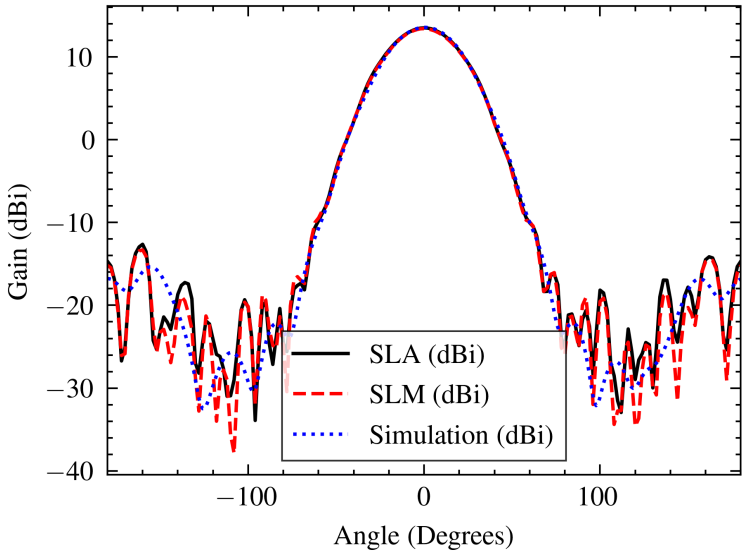

Figure 5.48. Horn antenna co-polar azimuth measurement 23.5 GHz.

5.4.5 Array patterns

5.4.5.1 Reference array

A reference array, printed with SLA resin, without time delays is presented to understand the pattern results of the array better. This array was identical to the synthesized array, except that the time delays were replaced with straight waveguide sections. A vital characteristic seen in Figure 5.49 is the shifting of the main lobe left or right, indicating that the main lobe squints with changing frequency. The reference design achieved a side lobe level (SSL) of 6.88 dB, while in simulation it achieved 7.24 dB. Changing the frequency to below 20 GHz causes the grating lobes to move to the front of the antenna until it has a lower gain than the main lobe, after which the grating lobe becomes the main lobe.

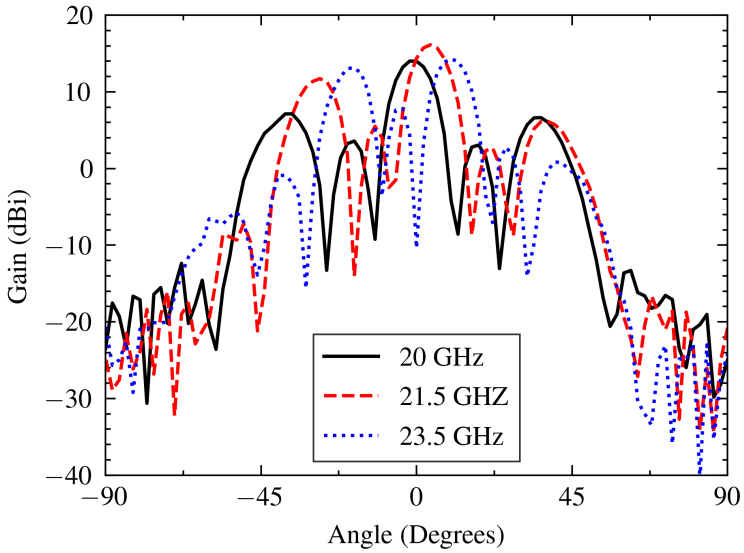

Figure 5.49. Azimuth pattern for the reference array.

As a result of the squint in Figure 5.49, the elevation measurement at 23.5 GHz in Figure 5.50 shows little gain. This is because, at 23.5 GHz, a null has been steered to boresight. Besides the main beam movement affecting the elevation, the elevation pattern is expected to look similar to a standard horn antenna since radiating elements are only placed along the azimuth axis.

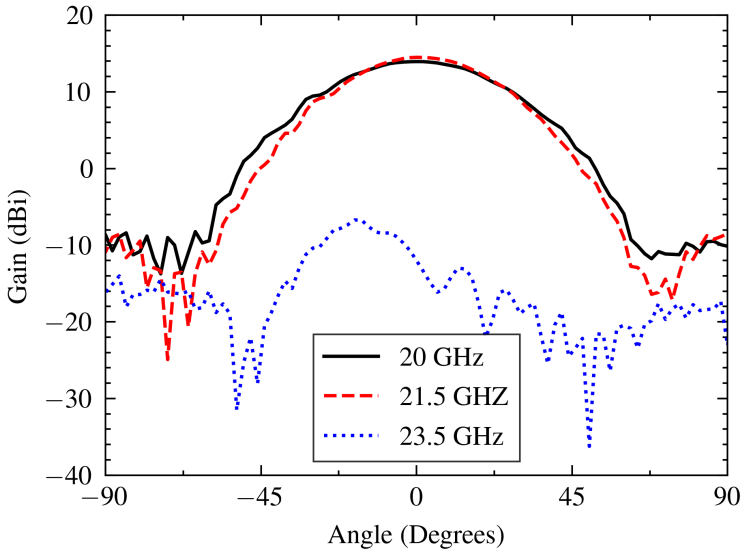

Figure 5.50. Elevation pattern for the reference array.

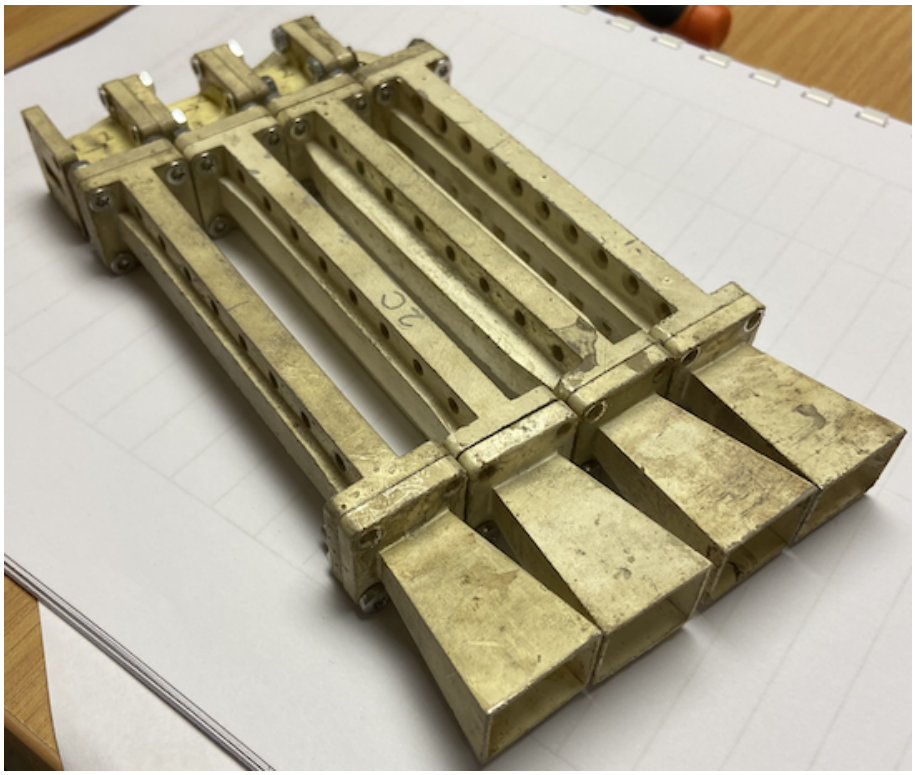

Figure 5.51. The assembled SLA horn array.

5.4.5.2 SLA array

The assembled SLA horn array is shown in Figure 5.51. The input port can be seen toward the top left of the image. Figure 5.52 shows the radiation pattern for the SLA delay compensated antenna array. The main beam remains fixed at boresight at different frequencies. The array achieved a peak gain of 16 dBi at 23 GHz. The centre frequency of the array was at 23 GHz, which is not unexpected since this is where the group delays and output power were the most similar, as seen in Figures 5.40 and 5.39. The side lobe level (SSL) achieved by the SLA array was 7.69 dB compared to 8.27 dB in the simulation at 23.5 GHz. The poorer side lobe level is mainly a result of the power dividers directing more power to the first and last radiators on the feed branch. The array is designed for uniform excitation of the radiating elements. Improvements to SSL can be made by applying current tapering to the excitations used to drive the horns.

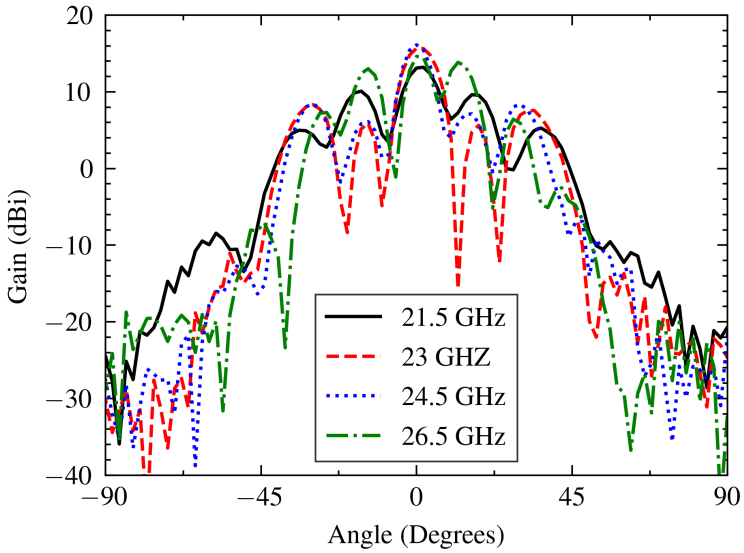

Figure 5.52. Azimuth pattern for the SLA compensated array.

The elevation pattern for the array is shown in Figure 5.53. The shape of the patterns looks similar to the pattern of the horn antenna but with more gain. At 21 GHz, the beam is squinted downwards slightly.

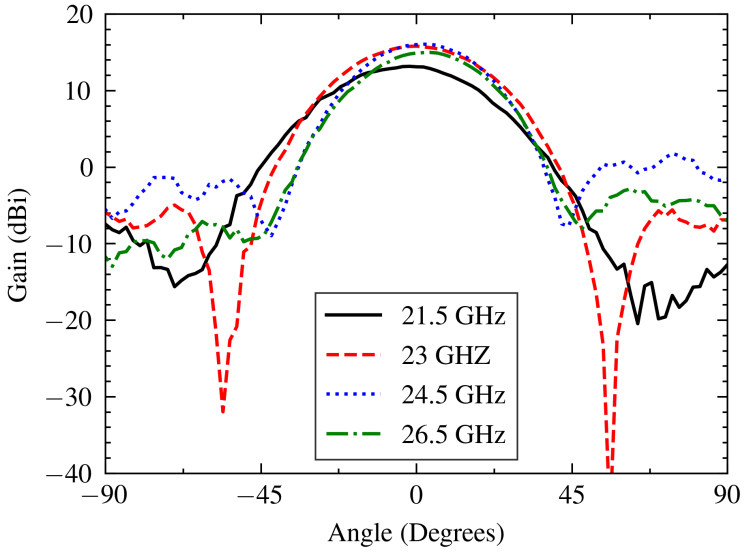

Figure 5.53. Elevation pattern for the SLA compensated array.

The cross-polarised azimuth pattern is shown in Figure 5.54 and looks similar to the co-polarised

pattern but with a lower gain. The cross-polarisation is caused by the cross-polarisation of the horn antennas shown earlier. Depending on the frequency, the difference between co-polarised and cross-polarised gain is roughly 19 dB, while for the horn, it was 20 dB. This confirms that the horns are the cause of cross-polarisation.

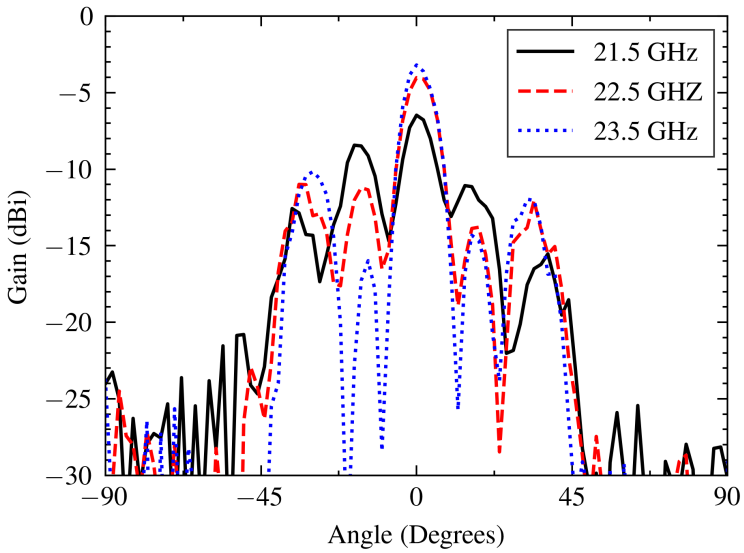

Figure 5.54. Cross-polarised azimuth pattern for the SLA compensated array.

The cross-polar elevation measurement shows that the cross-polar levels are 30 dB below the co-polar level, which is a favourable result.

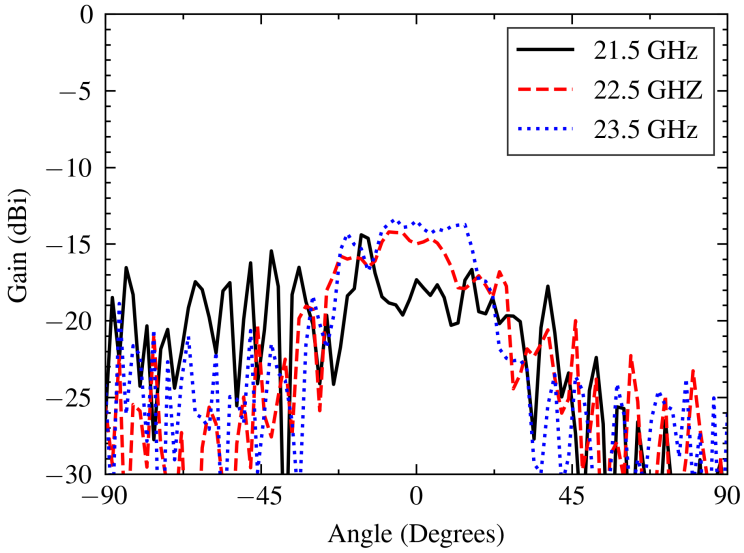

Figure 5.55. Cross-polarised elevation pattern for the SLA compensated array.

Figure 5.56. SLA horn on the measurement platform.

The SLA horn on the measurement platform is shown in Figure 5.56.

5.4.5.3 SLM array

The assembled SLM horn array is shown in Figure 5.57. The array is identical to the SLA array but is manufactured using SLM printing. The effect of distortion of the alignment of the horns is clearly evident. As a result the SLM array pattern shown in 5.58 was very dissimilar to the simulation in Figure 5.23. At 22.5 GHz, there was no discernible main lobe. The maximum gain achieved at 22.5 GHz was 12.9 dBi, skewed to the right of boresight. The pattern at 27 GHz bore the closest resemblance to the simulation. There was a 15 dBi main lobe at 3.16° left of boresight and two grating lobes 25° away from the main lobe. The high losses of the SLM time delays meant that the incorrect signal powers arrived at the radiators, which combined with the distortion on the printed prototype prevented the correct array pattern.

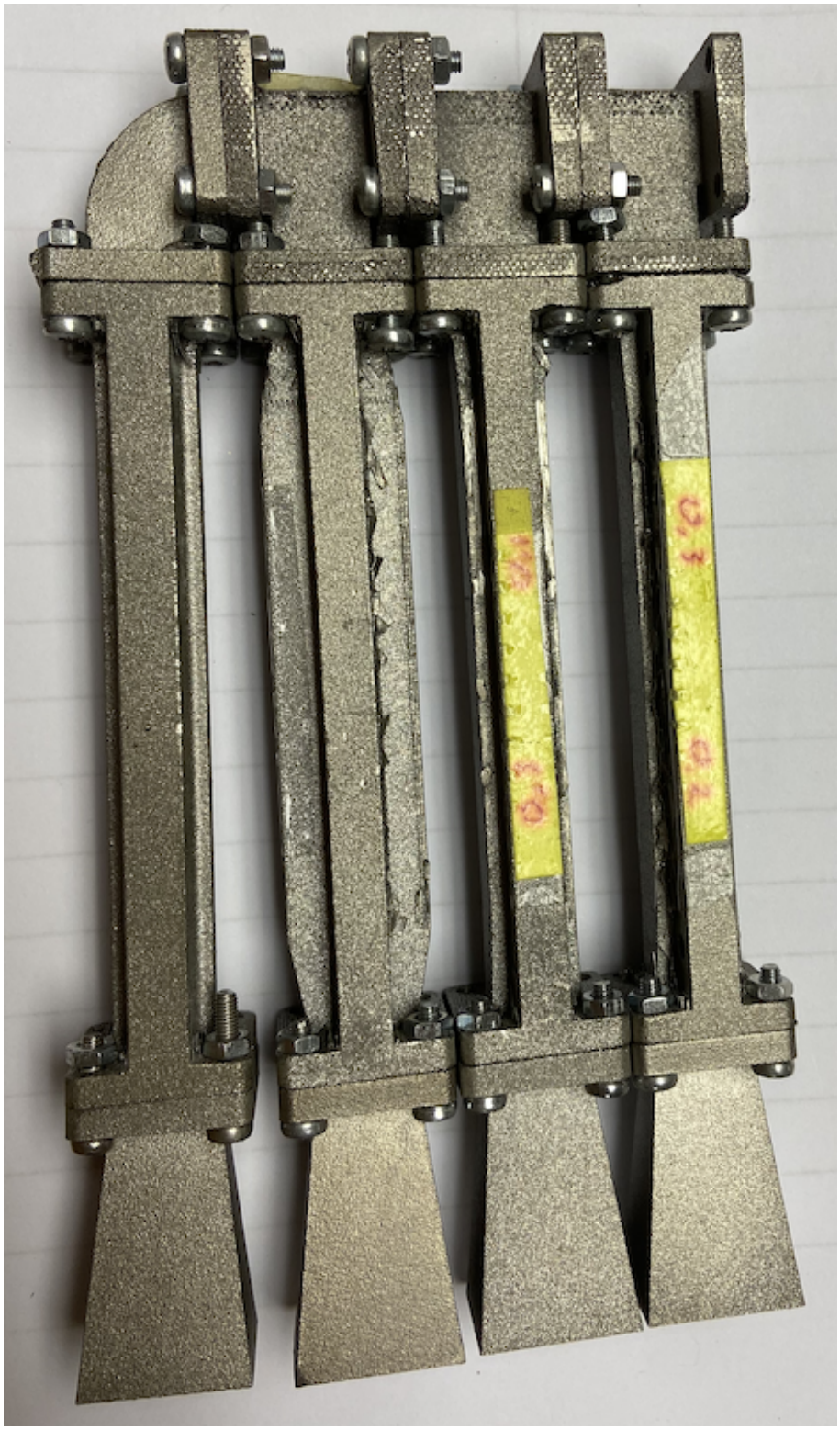

Figure 5.57. Assembled SLM horn array.

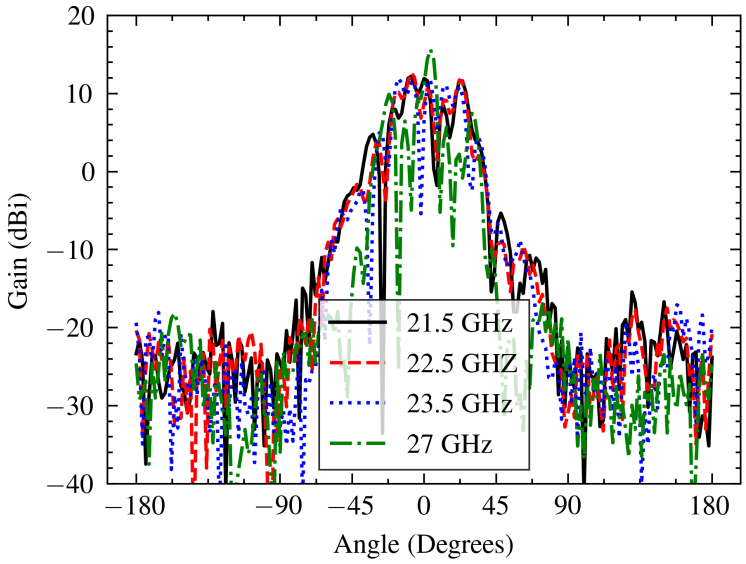

Figure 5.58. Co-polarised azimuth pattern for the SLM compensated array.

The elevation patterns resembled that of the horn antennas. The peak gain was 12 dBi at 20.5 GHz. Because the radiation pattern is not perfectly aimed at boresight, different peak gains are seen when looking at the azimuth and elevation results at different frequencies. The pattern maintained its shape from 18.5 Hz to 23 GHz but with gain decreasing away from 23 GHz. At higher frequencies, the beam began to skew downwards. This result highlights the degree to which the losses and distortion in SLM affect the array. The gain should be larger than achieved with a single horn, but in this case, it is less. This is due to the losses and the distorted geometry.

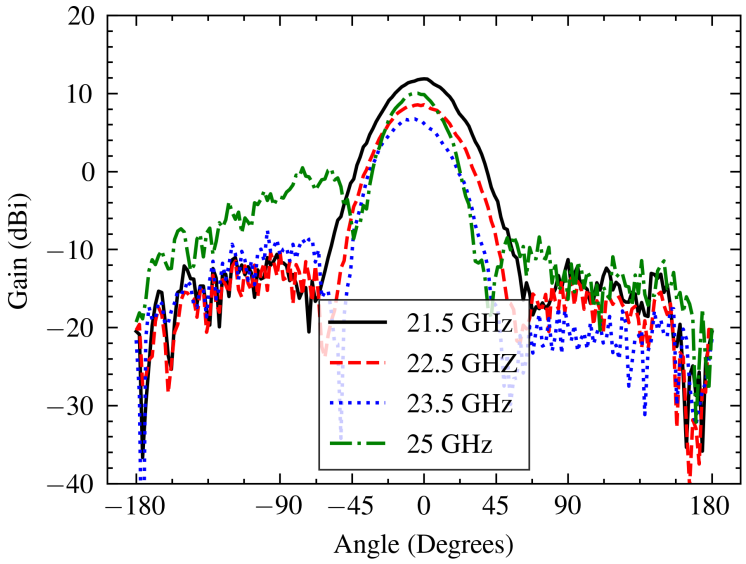

Figure 5.59. co-polar elevation pattern for the SLM compensated array.

The cross-polar azimuth pattern looks similar to the co-polar pattern. Again, most of the cross-polarisation can be attributed to the horn antennas.

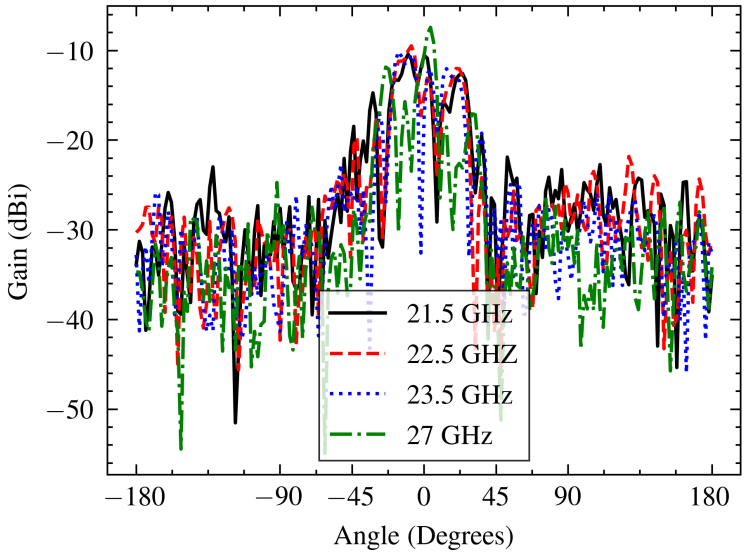

Figure 5.60. Cross-polarisation azimuth pattern for the SLM compensated array.

The cross-polar elevation plot bears little resemblance to the co-polar plot. At 27 GHz, some concentration of the radiated signal can be seen.

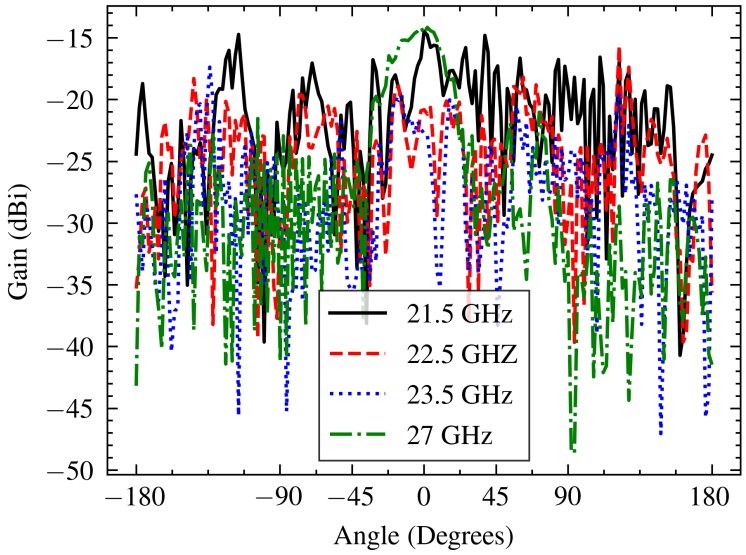

Figure 5.61. Cross-polarisation elevation pattern for the SLM compensated array.

5.4.6 Performance review

Only the SLA array exhibited a response that compared well to the simulation. The SLM array did not achieve the intended pattern due to print distortion shown in Figure 4.33, which meant that the radiating elements were not parallel nor uniformly spaced. Furthermore, the SLM prints exhibited more loss, which interfered with the beamforming as well. A performance summary for the array is given in Table 5.5.

Table 5.5. Summary of array performance over 21.5-26.75 GHz.

	SLA	SLM	Simulation	Reference Array (SLA)
Gain (dBi)	16.4	12.9	18.85	16.1
SLL (dB)	7.69	NA	8.27	6.88
Squint (°)	1.58	NA	0.0	10.52
Reflection coefficient (dB)	-22.5	-24	-22.3	-18

Over the band of 21.5 – 26.75 GHz, the compensated array exhibits less than 7.5° beam steering variation, while the uncompensated beam varies by 12.61° over the same bandwidth. In the band of 21.5 GHz to 23.5 GHz (8 % bandwidth), the uncompensated array achieved a squint of 6.35° while the compensated array had only 0.5°. Over 20% of the bandwidth (21.5 GHz to 25.5 GHz), the beam

varies by 1.58°. The operating band of the SLA array was slightly offset to a higher frequency than the simulation. This is because the delay variation (seen in Figure 5.32) is flatter at higher frequencies than at lower frequencies. The SLA printed array provided the closest gain to that of the simulation. The reference array and the SLA array achieved similar gain which was expected since the only difference was that the delays were replaced with straight sections that were also made using silver plating. However, since the main lobe varies with frequency, the gain is only achieved at 21.5 GHz and decreases for all other frequencies because the directivity of the horn reduces the main lobe gain.

The difference in SLL between the SLA and simulated array is minor and is most likely a result of minor printing distortion in the SLA antenna. Since the SLM array did not achieve a pattern that resembled the simulated array, a good estimate for SLL cannot be given. The poorer SLL in the reference array results from the skewed main beam, which increases the grating lobes gain, and decreases the main lobe gain.

The SLA array achieved reduced squint, which is easily noticeable compared to the reference array. Figure 5.62 shows measured squint versus frequency. The figure shows the main beam direction relative to the direction where the maximum directivity is achieved. When considering the reference array, there is a sharp jump at 24 GHz because the grating lobe moves to the front of the array and has a greater gain than the main lobe.

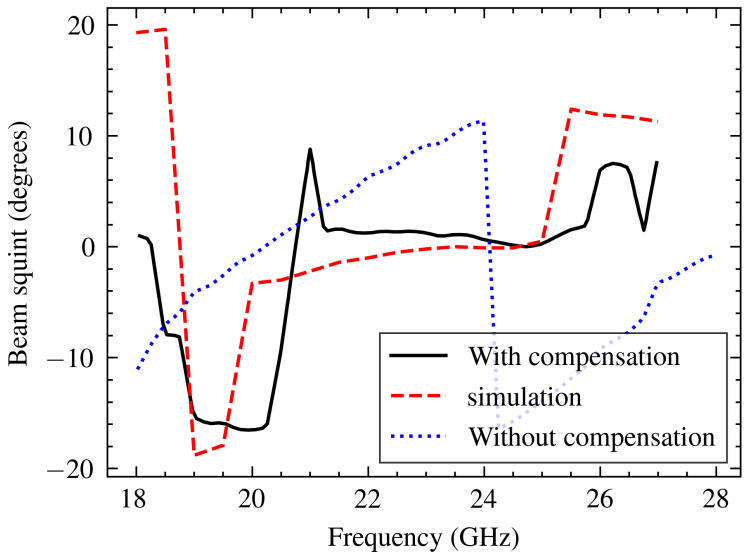

Figure 5.62. Beam angle vs frequency.

The simulated array achieved the highest gain of 18.89 dBi, 2.9 dB more than the SLA array and 6 dB more than the SLM array. The reduced gain can be attributed to the largest losses for the SLM components. The simulated array performed slightly worse where the beam varied by 1.3°. The reflection coefficient was the only measurement where the SLM array performed best. The SLA and simulated array performed similarly to the simulation, while the reference array performed the worst, with its in-band reflection coefficient peaking up to -18 dB. By skimming the flanges of the SLM waveguide, very low reflection coefficients were achieved. The reflection coefficient before skimming the flange was not measured as the flanges were rough, similar to low-grit sandpaper, which risked damaging the waveguide adapters.

5.5 ARRAY REALISATION CONCLUSION

The array used in this work was uniformly excited and equally spaced. The time delays that were manufactured provided similar delays to those in the simulation. The physical time delays did have more loss than the simulation due to surface roughness caused by the manufacturing process. The SLM time delays were lossier than the SLA versions due to the increased roughness of SLM printing. Both the SLA and SLM power divider performed similarly to the simulation. The short paths of the power divider meant there was little signal loss due to surface roughness. The same was seen with the horn antennas.

Multiple versions of the array were made. Two versions with time delay equalisation were made, of which one was manufactured using white SLA resin and the other using SLM printing. A reference array where there was no time delay equalisation was also manufactured. When comparing the SLA arrays with and without time delay equalisation to one another there was a clear difference in beam patterns. With time delays the main beam of the compensated array varied by only 0.5° while without compensation the beam varied by 6.35°. The SLM array had too many losses and print distortions for correct beam forming to take place. There was no clear main beam. Furthermore, the losses of the SLM printing meant that the SLM array had reduced gain.

CHAPTER 6 CONCLUSION

6.1 PERFORMANCE REVIEW AND APPLICATION RECOMMENDATIONS

This work designed and constructed a horn array with additively manufactured waveguide components. Both SLA printing with silver plating and SLM printing were investigated. The SLA parts were electroless plated using only the Tollens reaction. The SLA plating produced components with good electrical properties. A particularly good result was the straight sections and power dividers. The low losses of the straight sections compared well to other work in the literature. The silver-only waveguide featured lower loss and was easier to manufacture as a monoblock part. A summary of other works in literature, compared to this work, is presented in Table 6.1. Only more complex manufacturing techniques, such as electroplating, produced lower loss. An important result of this work was the effect of the number of rounds of electroless Tollens plating on electrical performance, as well as the effect of cooling the solution. Four rounds of silver produced a comparable loss to what was achieved

Table 6.1. Performance comparison table.

Source	Loss dB/m @ Frequency	Plating Type
[43]	4.3 dB/m @ Ka-band	Binder Jetting with metal infiltration
[62]	14 dB/m @ 75-110 GHz	SLA with Tollens silver plating (original)
[70]	11 dB/m @ K-band	Silver ink dispensing on FDM
[71]	1.29 dB/m @ Ku-band	FDM with liquid metal filling
[29]	0.58 dB/m @ X-band	FDM ABS with copper electroplating
[72]	3.75 dB/m @ X-band	SLS printing
This work	2 dB/m @ K-band	SLA printing with silver plating (4 rounds)
This work	1.25 dB/m @ K-band	SLA printing with silver plating (6 rounds)
This work	2.1 dB/m @ K-band	Copper electroplating on silver plating

with copper plating in this work. Extra rounds of silver plating surpassed the copper plating done here and are only outdone by other work which used copper plating. Considering the performance achieved with silver plating, there was little reason to use copper plating. Copper plating the parts was much more difficult than using silver plating on its own. Furthermore, using copper plating would have required parts to be made as split blocks. The silver plating also worked well for the power divider, which performed marginally better than the SLM part except with respect to input match.

Electroless silver is particularly good for low-cost prototypes or when a part is needed quickly. Excluding the printing time, parts can be manufactured in as little as 2 hours. The printing time adds a day or two, depending on the geometry. A limitation of the silver plating is that with enough friction, the silver plating can be rubbed off, limiting its use in applications where there is abrasion or a high amount of shock. Its resilience to other environmental stresses has not yet been evaluated.

The antenna array with delay equalization exhibited lower beam squint than the reference array and compared well to other works. In [22], an LWA is designed with a metasurface lens compensating for beam squint. This LWA achieved a bandwidth of 20% with 1.2 ° of squint at the expense of size. The array length was roughly 480 mm and had a depth of 300 mm. In [23], a 60 GHz array is manufactured, which achieves a 20% bandwidth with 0.5° of beam angle variation. The array is about 100 mm wide and has a depth of 70 mm. The works in [21] achieved a bandwidth of 10% with 12° of squint. The array in [21] was made from a coplanar waveguide and the lens was placed on top of the antenna. The lens was made from Rogers 3003 substrates that were 6.5 mm thick, making the antenna very compact. The array that was made in this work compares favourably to others. This array is more compact and achieves similar bandwidth and squint variation. The array designed here had a width of 90 mm and a depth of 150 mm with 17% bandwidth with a squint variation of 1.5°. The design of the compensation lenses requires complex mathematics making the design challenging. In contrast, the approach here uses path length, which is simple and can be performed quickly as long as a design for a time delay waveguide exists. The arrays designed in [22] and [23] required dispersive lenses that are large and complex to manufacture, composed of some periodic structures. These designs require complex machining to manufacture. The work in [21] was manufactured using PCB. Using a mature process such as PCB is more straightforward than the additive manufacturing used here and is also low-cost. Still, the PCB array did not achieve the small beam squint achieved in this study. The array manufactured in this study was smaller than compensation lenses with similar performance while achieving a similar or better level of beam squint reduction. Since the waveguide

could have been manufactured using additive manufacturing of printed resins, the array is lightweight compared to metal arrays. The waveguide design is also simpler, focusing only on the time taken for power to reach the output.

6.2 NOVELTY OF THIS WORK

This work contributes to the understanding of SLA printing with electroless plating. It provides an in-depth analysis of the silver plating process parameters, which has yet to be found in the literature. Electroless silver plating has been used before but has only been directly applied to high frequencies above V-band without added electroplating. However, this plating is thin, resulting in an unsuitable metal finish for lower frequencies. In this work, the plating process is applied to K-band waveguides. For this to be successful, the plating process had to be adjusted from the original to achieve a thicker skin depth. Furthermore, there is no mention in the literature of the effect of different resins on the plating process, which is also investigated here. In this work, two resin types were chosen and tested: white resin and clear resin.

While parts with only silver plating provided good performance, the silver plating was also used as a seed layer onto which copper is electroplated. Usually, other metals like silver and nickel are used as a colloid, which is used for electroplating another metal onto the part. In this work, silver is deposited onto the part with Tollens reaction, which is simpler than when a silver colloid is used and can produce thicker layers.

Beam squint in series-fed arrays has been solved in literature through multiple means, such as non-Foster circuits and compensation lenses, which equalise the phase at the array's output or counteract squint by squinting the beam in the opposite direction. Non-Foster circuits and compensation lenses are complex to design and manufacture, while time-delay circuits are difficult to integrate into waveguides. The advantage of the solution presented here is the simplicity of design. Also, since classical rectangular waveguide is used without the need for dielectric lenses, manufacturing is much easier than the before mentioned approaches.

6.3 EVALUATION OF RESEARCH QUESTIONS

The research questions in Chapter 1 are answered below.

How can series-fed arrays be designed to reduce squint over large bandwidths?

As discussed in Chapter 1, the beam squint issue is caused by unequal path lengths. Equalising the path by delaying the signal or increasing path length where necessary can equalise paths. This work

used waveguide integrated time delay sections because keeping the array's element spacing equal is easier than using meandered lines.

How can additive manufacturing be used to realise low-cost, rapidly prototyped antenna arrays with low beam squint?

Using additive SLA resin printing with silver plating allowed quick manufacturing of the waveguide parts. The waveguide parts were printed overnight and plated with silver the next day. Modifications were made to parts when necessary and re-printed. The non-toxicity of the manufacturing process makes it simple and aids in keeping costs and minimising manufacturing time since special tools and materials are not needed. The antenna beam angle can also be quickly re-configured by creating time delays with different characteristics, which can be done in a matter of hours when using additive manufacturing.

What limitations are imposed by additive manufacturing on waveguide components?

Because additive manufacturing creates parts layer by layer, some geometries cannot be manufactured easily. An example from this work is rectangular waveguides. Lying flat, a large hanging edge would require internal supports to print, which was avoided in this work. Re-orientating parts so that there were no hanging edges was an easy fix. However, this is only sometimes a viable solution, meaning that specific part geometries must be chosen for suitability for additive manufacturing. This was the case for the time delays, where alternatives originally under consideration would need internal support regardless of the geometry.

Can waveguide components be manufactured with low-cost techniques?

The cost to manufacture the straight section was R288, and the cost to purchase the same machined part was R2411, which took a month to deliver. The chemicals needed for silver plating are not very hazardous, in contrast to the strong acids used in conventional processes, which must be disposed of as chemical waste and adds to costs. While the purchased waveguide performs slightly better, the printed waveguide would work well for prototypes where multiple iterations are needed.

6.4 FUTURE WORK

The silver plating used to manufacture the waveguide could be applied differently. Using a pump to move the plating solution through the waveguide could assist by pushing air bubbles out of the parts. Small or complex parts that impede the flow of the plating solution could also benefit, especially

smaller waveguides. This could be applied to the time delays in this work to reduce the number of plating rounds needed.

The rate of the silver plating reaction could be slowed down chemically, preventing the need to cool reagents. In [67], electroless silver is used to make optical components. The rate of reaction was slowed down by adding Arabic Gum. The slow rate helped improve the surface roughness, with an average roughness of 10 nm to 15 nm. A parametric study of cooled reaction solution temperatures could also be conducted.

The factor limiting the bandwidth of the array was the bandwidth of the time delays. A flatter time delay would have extended the squint-free bandwidth since the signal's phase arriving at the horn antennas would remain equal. This should be pursued in future work.

REFERENCES

[1] H. Mirzaei and G. V. Eleftheriades, "Arbitrary-Angle Squint-Free Beamforming in Series-Fed Antenna Arrays Using Non-Foster Elements Synthesized by Negative-Group-Delay Networks," *IEEE Transactions on Antennas and Propagation*, vol. 63, no. 5, pp. 1997–2010, May 2015.

[2] W. L. Stutzman and G. A. Thiele, *Antenna theory and design*, 3rd ed. Hoboken, NJ, USA: Wiley, 2013.

[3] M. Longbrake, "True time-delay beamsteering for radar," in *2012 IEEE National Aerospace and Electronics Conference (NAECON)*, Dayton, OH, USA, Jul. 2012, pp. 246–249.

[4] H. Mirzaei and G. V. Eleftheriades, "An active artificial transmission line for squint-free series-fed antenna array applications," in *2011 41st European Microwave Conference*, Manchester, UK, Dec. 2011, pp. 503–506.

[5] S. Keser and M. Mojahedi, "Removal of beam squint in series fed array antennas using abnormal group delay phase shifters," in *2010 IEEE Antennas and Propagation Society International Symposium*, no. 1, Toronto, ON, Canada, Jul. 2010, pp. 1–4.

[6] L. Wang, J. L. Gómez-Tornero, and O. Quevedo-Teruel, "Dispersion reduced SIW leaky-wave antenna by loading metasurface prism," in *2018 International Workshop on Antenna Technology (iWAT)*, Nanjing, China, Jun. 2018, pp. 1–3.

[7] C. A. Balanis, *Antenna theory:analysis and design*, 3rd ed. New York, NY, USA: Wiley Interscience, 2005.

[8] F. B. Gross, *Leaky-Wave Antennas*. New York, NY, USA: McGraw-Hill Education, 2011.

[9] D. F. Sievenpiper, "Superluminal waveguides based on non-foster circuits for broadband leaky-wave antennas," *IEEE Antennas and Wireless Propagation Letters*, vol. 10, pp. 231–234, Mar. 2011.

[10] J. N. Smith and T. Stander, "A Capacitive SIW Discontinuity for Impedance Matching," *IEEE Transactions on Components, Packaging and Manufacturing Technology*, vol. 9, no. 11, pp. 2257–2266, Nov. 2019.

[11] M. Kitano, T. Nakanishi, and K. Sugiyama, "Negative group delay and superluminal propagation: an electronic circuit approach," *IEEE Journal of Selected Topics in Quantum Electronics*, vol. 9, no. 1, pp. 43–51, Jan. 2003.

[12] J. Long and D. F. Sievenpiper, "The Observation of Dispersionless Superluminal Propagation in a Non-Foster Loaded Waveguide and Its Fundamental Limitations," *IEEE Transactions on Microwave Theory and Techniques*, vol. 66, no. 2, pp. 762–773, Feb. 2018.

[13] D. Sievenpiper and J. Long, "Stable multiple non-Foster circuits loaded waveguide for broadband non-dispersive fast-wave propagation," *Electronics Letters*, vol. 50, no. 23, pp. 1708–1710, Nov. 2014.

[14] D. Pozar, *Microwave Engineering*, 4th ed. Hoboken, NJ, USA: John Wiley & Sons, 2011.

[15] J. Long, M. Jacob, and D. F. Sievenpiper, "Electronically steerable antenna using superluminal waveguide and tunable negative capacitors," in *Proceedings of the 2012 IEEE International Symposium on Antennas and Propagation*, Chicago, IL, USA, Jul. 2012, pp. 1–2.

[16] S. R. Rengarajan and C. R. White, "Stability Analysis of Superluminal Waveguides Periodically Loaded With Non-Foster Circuits," *IEEE Antennas and Wireless Propagation Letters*, vol. 12, pp. 1303–1306, Oct. 2013.

[17] H. Mirzaei and G. V. Eleftheriades, "Squint-free beamforming in series-fed antenna arrays using synthesized non-foster elements," in *2013 IEEE Antennas and Propagation Society International Symposium (APSURSI)*, Orlando, FL, USA, Jul. 2013, pp. 2209–2210.

[18] C. Madsen, G. Lenz, A. Bruce, M. Cappuzzo, L. Gomez, T. Nielsen, L. Adams, and I. Brenner, "An all-pass filter dispersion compensator using planar waveguide ring resonators," in *OFC/IOOC . Technical Digest. Optical Fiber Communication Conference, 1999, and the International Conference on Integrated Optics and Optical Fiber Communication*, vol. 4, San Diego, CA, USA, Aug. 1999, pp. 99–101 vol.4.

[19] S. Gupta, D. Sounas, Q. Zhang, and C. Caloz, "All-pass dispersion synthesis using microwave C-sections," *International Journal of Circuit Theory and Applications*, vol. 42, no. 12, pp. 1228–1245, Dec. 2014.

[20] M. Gustafsson, "Bandwidth constraints for passive superluminal propagation through metamaterials," *Applied Physics A*, vol. 109, no. 4, pp. 1015–1021, Dec. 2012.

[21] A. Mehdipour, J. W. Wong, and G. V. Eleftheriades, "Beam-Squinting Reduction of Leaky-Wave Antennas Using Huygens Metasurfaces," *IEEE Transactions on Antennas and Propagation*, vol. 63, no. 3, pp. 978–992, Mar. 2015.

[22] J. Chen, W. Yuan, C. Zhang, W. X. Tang, L. Wang, Q. Cheng, and T. J. Cui, "Wideband Leaky-Wave Antennas Loaded With Gradient Metasurface for Fixed-Beam Radiations With Customized Tilting Angles," *IEEE Transactions on Antennas and Propagation*, vol. 68, no. 1, pp. 161–170, Jan. 2020.

[23] O. Zetterstrom, E. Pucci, P. Padilla, L. Wang, and O. Quevedo-Teruel, "Low-dispersive leaky-wave antennas for mmWave point-to-point high-throughput communications," *IEEE Transactions on Antennas and Propagation*, vol. 68, no. 3, pp. 1322–1331, Mar. 2020.

[24] O. Quevedo-Teruel, R. C. Mitchell-Thomas, T. M. McManus, S. A. R. Horsley, and Y. Hao, "Conformal surface lenses from a bed of nails," in *The 8th European Conference on Antennas and Propagation (EuCAP 2014)*, The Hague, Netherlands, Sep. 2014, pp. 269–270.

[25] H. Mirzaei and G. V. Eleftheriades, "Eliminating Beam-Squinting in Wideband Linear Series-Fed Antenna Arrays Using Feed Networks Constructed by Slow-Wave Transmission Lines," *IEEE Antennas and Wireless Propagation Letters*, vol. 15, pp. 798–801, Sep. 2016.

[26] S. Papantonis, S. Lucyszyn, and E. Shamonina, "Dispersion effects in Fakir's bed of nails metamaterial waveguides," *Journal of Applied Physics*, vol. 115, no. 5, p. 054903, Feb. 2014.

[27] Z. Lu, R. Wen, Z. Su, W. Ge, Z. Wang, H. Gong, and Y. Gong, "Novel Helical Groove Rectangular Waveguide Slow Wave Structure for 0.2 THz Traveling Wave Tube," *IEEE Electron Device Letters*, vol. 40, no. 9, pp. 1526–1529, Sep. 2019.

[28] X. Xu, Y. Wei, F. Shen, Z. Duan, Y. Gong, H. Yin, and W. Wang, "Sine Waveguide for 0.22-THz Traveling-Wave Tube," *IEEE Electron Device Letters*, vol. 32, no. 8, pp. 1152–1154, Aug. 2011.

[29] M. D'Auria, W. J. Otter, J. Hazell, B. T. Gillatt, C. Long-Collins, N. M. Ridler, and S. Lucyszyn, "3-D Printed Metal-Pipe Rectangular Waveguides," *IEEE Transactions on Components, Packaging and Manufacturing Technology*, vol. 5, no. 9, pp. 1339–1349, Sep. 2015.

[30] S. Olivera, H. B. Muralidhara, K. Venkatesh, K. Gopalakrishna, and C. S. Vivek, "Plating on acrylonitrile–butadiene–styrene (ABS) plastic: a review," *Journal of Materials Science*, vol. 51, no. 8, pp. 3657–3674, Apr. 2016.

[31] D. Miek, S. Simmich, and M. Hoft, "Additive manufacturing of symmetrical X-band waveguide filters for wide-band applications based on extracted pole filter design," in *2019 IEEE MTT-S International Microwave Workshop Series on Advanced Materials and Processes for RF and THz Applications (IMWS-AMP)*, Bochum, Germany, Jul. 2019, pp. 13–15.

[32] D. Bruhn, D. Miek, K. Braasch, F. Kamrath, C. Bartlett, P. Boe, and M. Höft, "Effects of Cutting Planes on Filter Performance of FDM 3D-Printed X-Band Waveguide Filters," in *2021 IEEE MTT-S International Microwave Filter Workshop (IMFW)*, Perugia, Italy, Nov. 2021, pp. 236–238.

[33] F. Teberio, A. Gomez-Torrent, I. Arregui, J. M. Percaz, I. Arnedo, M. Chudzik, T. Lopetegi, and

M. A. G. Laso, "Sensitivity analysis of a 3-D printed low-cost compact waveguide low-pass filter," in *2016 46th European Microwave Conference (EuMC)*, London, UK, Oct. 2016, pp. 249–252.

[34] A. Bal and G. H. Huff, "Modelling and Impact of 3D Print Inaccuracies on the Performance of Circular Waveguide Hybrid Coupler," in *2020 International Applied Computational Electromagnetics Society Symposium (ACES)*, Monterey, CA, USA, Jul. 2020, pp. 1–2.

[35] K. V. Hoel, N. Jastram, S. Kristoffersen, and D. Filipovic, "3D Printed Double Ridged Waveguide Rotman Lens System," in *2020 50th European Microwave Conference (EuMC)*, Utrecht, Netherlands, Jan. 2021.

[36] E. A. Rojas-Nastrucci, J. Nussbaum, T. M. Weller, and N. B. Crane, "Meshed rectangular waveguide for high power, low loss and reduced weight applications," in *2016 IEEE MTT-S International Microwave Symposium (IMS)*, San Francisco, CA, USA, May 2016, pp. 1–4.

[37] L. Polo-López, P. Sanchez-Olivares, E. García-Marín, J. Ruiz-Cruz, J. Córcoles, J. Masa-Campos, J. Montejo-Garai, and J. Rebollar, "Waveguide Manufacturing Technologies for Next-Generation Millimeter-Wave Antennas," *Micromachines*, vol. 12, no. 12, p. 1565, Dec. 2021.

[38] B. Zhang and H. Zirath, "Metallic 3-D Printed Rectangular Waveguides for Millimeter-Wave Applications," *IEEE Transactions on Components, Packaging and Manufacturing Technology*, vol. 6, no. 5, pp. 796–804, May 2016.

[39] P. Vaitukaitis, K. Nai, J. Rao, and J. Hong, "3D Metal Printed Deformed Elliptical Cavity Bandpass Filter with an Additional Plate," in *2021 IEEE CPMT Symposium Japan (ICSJ)*, Kyoto, Japan, Nov. 2021, pp. 118–119.

[40] C. Beck, J. Gabsteiger, C. Scheitler, M. Dietz, A. Hagelauer, and R. Weigel, "An additive manufactured K-Band Waveguide Coupler and K-Band Antennas in SLM-Technology," in *2020 23rd International Microwave and Radar Conference (MIKON)*, Warsaw, Poland, Oct. 2020, pp. 274–277.

[41] A. Vaske, A. Akar, and B. Neubauer, "Coplanar Waveguide Fed U-Band Horn Antenna Manufac-

tured Using 3D Printing and Electroplating," in *2022 16th European Conference on Antennas and Propagation (EuCAP)*, Madrid, Spain, Mar. 2022, pp. 1–4.

[42] S. Verploegh and Z. Popovic, "V- and W-band Two-Way Waveguide Splitters Fabricated by Metal Additive Manufacturing," in *2018 IEEE MTT-S Latin America Microwave Conference (LAMC 2018)*, Arequipa, Peru, Dec. 2018, pp. 1–4.

[43] E. A. Rojas-Nastrucci, J. T. Nussbaum, N. B. Crane, and T. M. Weller, "Ka-Band Characterization of Binder Jetting for 3-D Printing of Metallic Rectangular Waveguide Circuits and Antennas," *IEEE Transactions on Microwave Theory and Techniques*, vol. 65, no. 9, pp. 3099–3108, Sep. 2017.

[44] R. Zhu and D. Marks, "Rapid prototyping lightweight millimeter wave antenna and waveguide with copper plating," in *2015 40th International Conference on Infrared, Millimeter, and Terahertz waves (IRMMW-THz)*, Hong Kong, China, Aug. 2015, pp. 1–2.

[45] M. Paunovic and M. Schlesinger, *Modern electroplating*, 5th ed. Hoboken, NJ, USA: John Wiley & Sons, 2010.

[46] G. P. Le Sage, "3D Printed Waveguide Slot Array Antennas," *IEEE Access*, vol. 4, pp. 1258–1265, Mar. 2016.

[47] R. Zhu, G. Lipworth, T. Zvolensky, D. R. Smith, and D. L. Marks, "Versatile Manufacturing of Split-Block Microwave Devices Using Rapid Prototyping and Electroplating," *IEEE Antennas and Wireless Propagation Letters*, vol. 16, pp. 157–160, May 2017.

[48] K. Zhao, J. A. Ramsey, and N. Ghalichechian, "Fully 3-D-Printed Frequency-Scanning Slotted Waveguide Array With Wideband Power-Divider," *IEEE Antennas Wireless Propagat Lett*, vol. 18, no. 12, pp. 2756–2760, Dec. 2019.

[49] K. Lomakin, G. Gold, S. Herold, L. Ringel, J. Ringel, D. Simon, M. Sippel, A. Sion, M. Vossiek, and K. Helmreich, "SLA-Printed 3-D Waveguide Paths for E-Band Using Electroless Silver

Plating," *IEEE Transactions on Components, Packaging and Manufacturing Technology*, vol. 9, no. 12, pp. 2476–2481, Dec. 2019.

[50] E. G. Geterud, P. Bergmark, and J. Yang, "Lightweight waveguide and antenna components using plating on plastics," in *2013 7th European Conference on Antennas and Propagation (EuCAP)*, Gothenburg, Sweden, Apr. 2013, pp. 1812–1815.

[51] Y. Lee, S.-M. Sim, R.-L. Kang, I. Llamas-Garro, Y. Wang, Y.-H. Jang, and J.-M. Kim, "Two-way Waveguide Power Divider using 3D Printing and Electroless Plating," in *2018 48th European Microwave Conference (EuMC)*, Madrid, Spain, Sep. 2018, pp. 219–222.

[52] X. Han, G. Wang, J. He, J. Guan, and Y. He, "Influence of temperature on the surface property of ABS resin in KMnO 4 etching solution," *Surface and Interface Analysis*, vol. 51, no. 2, pp. 177–183, Feb. 2019.

[53] J. Haumant, R. Allanic, C. Quendo, D. Diedhiou, A. Manchec, C. Person, and R.-M. Sauvage, "Ultra Wideband Transition From Coaxial Line to Two Parallel Lines Manufactured Using Additive Manufacturing Technology," in *2019 IEEE MTT-S International Microwave Symposium (IMS)*, Boston, MA, USA, Jul. 2019, pp. 1217–1220.

[54] Jet Metal. "Solutions" JetMetal-Tech.com. https://www.jetmetal-tech.com/?lang=en (accessed Mar. 26, 2023).

[55] E. Márquez-Segura, S. Shin, A. Dawood, N. M. Ridler, and S. Lucyszyn, "Microwave Characterization of Conductive PLA and Its Application to a 12 to 18 GHz 3-D Printed Rotary Vane Attenuator," *IEEE Access*, vol. 9, pp. 84 327–84 343, Jun. 2021.

[56] P. Sanchez-Olivares, J. L. Masa-Campos, E. Garcia-Marin, and D. Escalona-Moreno, "High-Gain Conical-Beam Traveling-Wave Array Antenna Based on a Slotted Circular Waveguide at Ku -Band," *IEEE Transactions on Antennas and Propagation*, vol. 68, no. 8, pp. 6435–6440, Aug. 2020.

[57] D. M. Mattox, *The foundations of vacuum coating technology*, second edition. ed. Berlin, DE.: Springer-Verlag, 2018.

[58] Z. L. Ma, C. H. Chan, and B.-J. Chen, "A 3-D Printed Waveguide-Based Linearly Polarized Magnetoelectric Dipole Antenna," *IEEE Antennas and Wireless Propagation Letters*, vol. 20, no. 1, pp. 68–72, Jan. 2021.

[59] V. Gjokaj, P. Chahal, J. Papapolymerou, and J. D. Albrecht, "A novel 3D printed Vivaldi antenna utilizing a substrate integrated waveguide transition," in *2017 IEEE International Symposium on Antennas and Propagation*, San Diego, CA, USA, Jul. 2017, pp. 1253–1254.

[60] A. M. Cook, C. D. Joye, and J. P. Calame, "W-band and D-band Traveling-Wave Tube Circuits Fabricated by 3D Printing," *IEEE Access*, vol. 7, pp. 72 561–72 566, Jun. 2019.

[61] A. Tamayo-Dominguez, P. Sanchez-Olivares, A. Camacho-Hernandez, and J.-M. Fernandez-Gonzalez, "Guidelines for Accurate In-House Electroplating and 3-D-Printing Processes Applied to mm-Wave Devices," *IEEE Microwave and Wireless Components Letters*, vol. 32, no. 11, pp. 1267–1270, Jun. 2022.

[62] J. Shen, M. Aiken, C. Ladd, M. D. Dickey, and D. S. Ricketts, "A simple electroless plating solution for 3D printed microwave components," in *2016 Asia-Pacific Microwave Conference (APMC)*, New Delhi, India, Dec. 2016, pp. 1–4.

[63] L. Engel, K. Lomakin, G. Gold, T. Pfahler, J. Schür, and M. Vossiek, "3D Printed Waveguide Transition for 77 GHz Radar Applications," in *2022 14th German Microwave Conference (GeMiC)*, Ulm, Germany, May 2022, pp. 13–16.

[64] K. Lomakin, S. Alhasson, and G. Gold, "Additively manufactured amplitude tapered slotted waveguide array antenna with horn aperture for 77 GHz," *IEEE Access*, vol. 10, pp. 44 271–44 277, Mar. 2022.

[65] O. A. Peverini, G. Addamo, M. Lumia, G. Virone, F. Calignano, M. Lorusso, and D. Manfredi, "Additive manufacturing of Ku/K-band waveguide filters: a comparative analysis among selective-

laser melting and stereo-lithography," *IET Microwaves, Antennas & Propagation*, vol. 11, no. 14, pp. 1936–1942, Nov. 2017.

[66] S. Afazov, E. Semerdzhieva, D. Scrimieri, A. Serjouei, B. Kairoshev, and F. Derguti, "An improved distortion compensation approach for additive manufacturing using optically scanned data," *Virtual and Physical Prototyping*, vol. 16, no. 1, pp. 1–13, Jan. 2021.

[67] A. Antonello, B. Jia, Z. He, D. Buso, G. Perotto, L. Brigo, G. Brusatin, M. Guglielmi, M. Gu, and A. Martucci, "Optimized electroless silver coating for optical and plasmonic applications," *Plasmonics*, vol. 7, no. 4, pp. 633–639, Mar. 2012.

[68] S. H. Lee, J. S. Kim, Y. J. Yoon, and W. S. Lee, "Six-way power divider for series feed using H-plane T-junctions," *Microwave and Optical Technology Letters*, vol. 58, no. 7, pp. 1622–1626, Jul. 2016.

[69] B. Zhang, P. Linner, C. Karnfelt, P. L. Tarn, U. Sodervall, and H. Zirath, "Attempt of the metallic 3D printing technology for millimeter-wave antenna implementations," in *2015 Asia-Pacific Microwave Conference (APMC)*, Nanjing, China, Dec. 2015, pp. 1–3.

[70] S. Khan, N. Vahabisani, and M. Daneshmand, "A Fully 3-D Printed Waveguide and Its Application as Microfluidically Controlled Waveguide Switch," *IEEE Transactions on Components, Packaging and Manufacturing Technology*, vol. 7, no. 1, pp. 70–80, Jan. 2017.

[71] K. Y. Chan, R. Ramer, and R. Sorrentino, "Low-Cost Ku-Band Waveguide Devices Using 3-D Printing and Liquid Metal Filling," *IEEE Transactions on Microwave Theory and Techniques*, vol. 66, no. 9, pp. 3993–4001, Sep. 2018.

[72] G.-L. Huang and T. Yuan, "Application of 3-D metal printing to microwave components and antennas," in *2017 Sixth Asia-Pacific Conference on Antennas and Propagation (APCAP)*, Xi'an, China, Oct. 2017, pp. 1–3.